This is to certify that the

dissertation entitled

RING PACK BEHAVIOR AND OIL CONSUMPTION
MODELING IN IC ENGINES

presented by

Mikhail Aleksandrovich Ejakov

has been accepted towards fulfillment
of the requirements for

Ph.D. degree in Mechanical Engineering

Harold J. Schock
Major professor

Date August 27, 1998

RING PACK BEHAVIOR AND OIL CONSUMPTION MODELING IN IC ENGINES

By

Mikhail Aleksandrovich Ejakov

A DISSERTATION

Submitted to
Michigan State University
in partial fulfillment of the requirements
for the degree of

DOCTOR OF PHILOSOPHY

Department of Mechanical Engineering

1998

ABSTRACT

RING PACK BEHAVIOR AND OIL CONSUMPTION
MODELING IN IC ENGINES

By

Mikhail Aleksandrovich Ejakov

In this dissertation, two major research areas are considered: further development of the piston ring analysis model, and application of this model to engine design and analysis in order to better understand physical processes in an internal combustion engine. The model development includes: creating the first operational three-dimension ring twist model; establishing an interface between the in-cylinder combustion model and piston ring; and adding the ring pack optimization routine.

It was found that ring twist significantly influences ring pack performance and dynamics and that the nature of ring twist requires a three-dimensional analysis of the ring motion. Simulations were performed for an engine at the same operating conditions for several combinations of twist and no twist analysis. The results show the importance of modeling ring twist to achieve accurate predictions of the ring position, inter-ring gas pressures and inter-ring pressure gradients. Special attention has to be paid to the motion of the twisted second ring at the middle of the intake and the end of the compression stroke and to the top ring at the beginning of the compression stroke and the end of the exhaust stroke.

Another part of the model development includes the ring pack optimization routine. An optimization technique was developed and applied to ring-pack design synthesis. When applied to existing engine ring-pack designs, optimized results indicated the poten-

tial for significant reduction in blow-by through the ring-pack by optimizing ring geometry.

In analysis of the blow-by of combustion chamber gasses through the ring pack, the coupled effects of ring dynamics, piston dynamics, ring-pack gas dynamics, and in-cylinder pressure are all important for achieving accurate predictions of blow-by. It was recognized that ring pack cannot be de-coupled from the engine bore-stroke ratio through its influence on piston / ring motion, therefore it has to be considered in the early stages of engine design in order to optimize ring pack performance.

In the Variable Displacement Engine (VDE) analysis, interesting physical phenomena associated with the ring pack transient processes after the engine valves are shut off were analyzed. The model predictions indicated the optimal valve timing in order to minimize losses of the in-cylinder pressure due to blow-by through the ring pack.

to my parents, to my grandma,

to my fiancée Sally,

and to Jules, who made this possible...

ACKNOWLEDGMENT

I would first like to thank my research advisor Dr. Harold J. Schock. He has provided invaluable guidance and motivation. Even at most difficult times of my graduate studies, he had a faith in me, and his encouragement and support have helped me to overcome the difficulties.

I would also like to thank the members of my guidance committee: Giles Brereton, Mei Zhwang, Alexanro Diaz, Ridge Golding, and Jules LoRusso. I would like to express my special thanks to Dr. Brereton for his encouragement and willingness to listen to me and answer all my questions; Dr. Diaz for his encouragement and support of ring pack optimization; and Dr. Steve Shaw for long hours discussing ring dynamics.

I would like to express a very special thanks and appreciation to Jules. His support has helped me to complete my degree, and his encouragements, enthusiasm, energy, and optimism have been more than invaluable.

A special recognition needs to be expressed to Dr. Lawrence Brombolich. His knowledge, enthusiasm, and experience have helped me to overcome the challenge.

The people from Ford: Rick Williams, George Davis, Chuck Newman, Yi Lu, Fred Trinker, Jim Novak, and Erik Kiledal have deserved a special thanks for helping me at my study and providing expertise, support, and technical assistance.

It would have been impossible to do my research without friends and colleagues from The Engine Research Laboratory: Hans Hascher, Mark Novak, Dr. Lee, Jon Darrow, Larry Dalimonte, Kass Jafri, Matt Foster, Mahmood Rahi, and our secretary Bobbie Slider. I would like to express my special thank to Hans Hascher for his support, recommendations, and encouragement; and Mark Novak for his help, technical assistance, and patience reading all my paper drafts and manuscripts.

My family has deserved a special thanks for being always supportive and encouraging during my graduate study, and my sister Anna for writing me weekly letters for four years.

I would like to thank my fiancee Sally. Her love, encouragement, optimism, and support made my life much better during these stressful times.

Table of Contents

LIST OF TABLES

LIST OF FIGURES

Chapter 1 INTRODUCTION

MOTIVATION

In recent years, a significant amount of work has been done in the area of internal combustion engine modeling and simulations. The "driving force" of these efforts has been an industry trend for fuel efficiency improvement, emissions reduction, and cost saving. Computer models have proven to be valuable tools for designing engines which satisfy all of these demands. An important part of overall engine modeling and design is understanding the processes occurring in the piston ring pack. The main purpose of the piston is to transfer the kinetic energy of the combustion gases into the mechanical energy output of the engine through a reciprocating mechanism. The piston rings can be considered as an auxiliary element of the piston. The main purpose of the piston rings is to eliminate combustion chamber energy losses through proper sealing of the combustion chamber from the environment at the level of the piston. In addition, the piston rings have to satisfy design constraints for durability, emissions, noise, vibration, manufacturing, and cost requirements. Most of these requirements are mutually exclusive. A good piston ring pack design represents a compromise among all of these factors. Even though piston ring design may appear simple, finding a suitable compromise requires extensive efforts in research and development. A bad piston ring design can significantly affect engine performance due to engine blow-by (insufficient ring pack sealing), engine emissions due to back flow and high oil consumption, engine durability due to excessive ring wear and ensuing ring failure, and compliance of the engine with Noise, Vibration, and Harshness (NVH) requirements due to ring fluttering.

The difficulties associated with finding a good ring pack design can be characterized by two primary factors. First, even having been studied for more than one century, the physics of an internal combustion engine still is not very well understood. The internal combustion engine represents a complicated cyclic technical device with multiple physical processes taking place simultaneously or concurrently. The cyclic nature of the problem provides sufficient conditions for non-steady transient cyclic processes. These physical processes can be described by fluid mechanics [1, 2, 82], thermodynamics [81], the theory of combustion [48], heat transfer [36], non-linear dynamics [38, 83, 70, 3], structural mechanics [84], and the theory of chaos [83, 70].

Second, in order to achieve a good ring pack design satisfying multiple constraints, the influence of a significant number of design parameters and factors affecting ring pack performance has to be considered. It is worth mentioning that the relative influence of ring pack design parameters also depends on a particular engine design and may vary significantly from one engine to another. Overall, designing the ring pack in particular and the engine in general requires a significant amount of experimental work and testing. That is why computer modeling and simulations have proven to be valuable theoretical tools for better understanding physical processes and providing practical design recommendations.

RING PACK DESIGN

A typical ring pack design of a modern gasoline engine includes three rings: two compression rings, and one oil control ring. The top compression ring usually has a symmetric cross section and a barrel face profile. The second compression ring is typically a twisted ring with a bevel cut or a step in its cross section with a taper face profile. However, both the compression rings can be twisted or non-twisted. The oil control ring typically consists of three pieces: two rails and an expander. The ring pack configuration shown in Figure 1 includes two twisted compression rings and a three-piece oil control ring. References on types and designs of piston rings may be found in [9, 50, 77].

PREVIOUS EFFORTS IN RING PACK MODELING

Ring pack modeling can be logically divided into the following submodels: inter-ring gas pressure, blow-by, and ring motion; ring lubrication; ring friction; ring wear; and oil consumption. Over the past fifty years, many aspects of inter-ring gas flow have been considered [5, 29, 34, 35]. Ting and Mayer [78, 79] presented a concept of a quasi-steady orifice-volume gas flow model for ring pack gas flow analysis. This approach has been employed in many research models [24, 66, 24, 46, 75, 10]. The original orifice-volume gas flow models include only the flow through the ring end gap clearances without considering the effect of ring side clearance on the inter-ring gas flow through the ring pack. Further developments involved incorporating ring axial motion and flow behind the ring groove with the orifice-volume approach [10, 46]. Namazian et al. [54] suggested an empirical orifice flow formula for the better description of the flow along the ring side

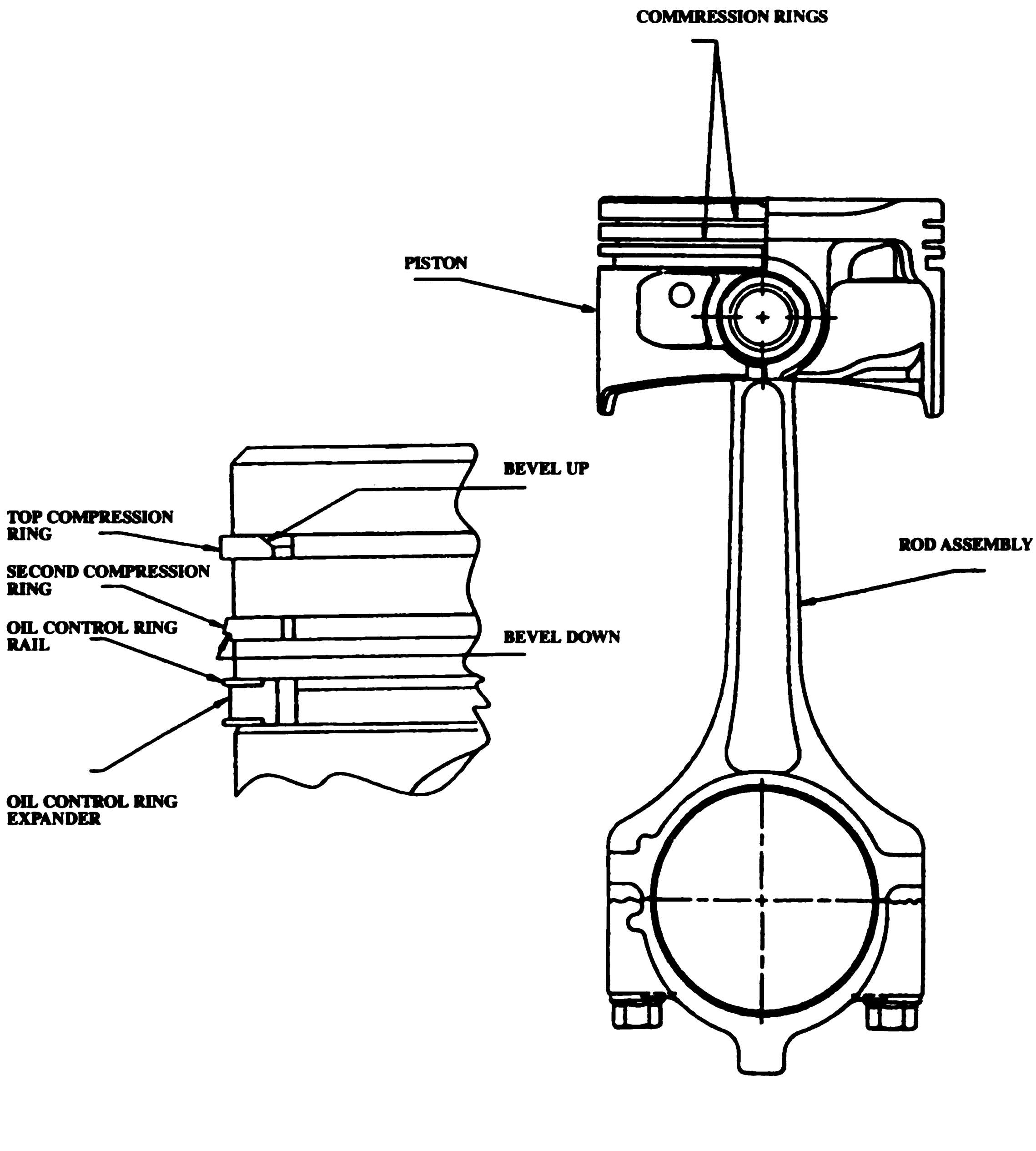

Figure 1 Piston / piston rings / connecting rod assembly

clearance. A very good description on the physical processes in the ring pack and the inter-ring gas flow modeling was given by Ting [77]. Other recent works include work done by Tian et al. [75], Keribar et al. [46], and Knowland et al. [47].

In early works on piston ring dynamics, only ring axial motion was considered [77, 34, 35]. In addition to axial translation motion, Tian et al. [75] and Keribar et al. [46] considered the effect of ring twist on ring dynamics and gas flow. However, these studies included only two-dimensional axisymmetric analysis. Corbat [21] tried to formulate a mathematical theory of three dimensional dynamics of non-symmetric piston rings. Due to the complexity of three-dimensional ring motion, only limited results are available.

Many theoretical studies on piston ring lubrication have been conducted. In 1886, Osborne Reynolds derived a mathematical equation to describe a general lubrication problem. The Reynolds equation and its modifications are still widely used for hydrodynamic lubrication problems. The Reynolds equation of hydrodynamic lubrication can be found in any lubrication textbook [14, 44].

Castleman [18] was one of the first who tried to study theoretically the lubrication of piston rings. He introduced the concept of hydrodynamic lubrication in the analysis of piston rings and made calculations of the oil film thickness. He considered a curved ring face profile and calculated the pressure distribution between a ring and a circular bore. Eilon and Saunders [28] assumed a symmetrical parabolic profile. Their calculations included the predictions of oil film thickness and friction forces acting on the ring. Furuhama [32] considered a ring profile consisting of a central flat region and two circular arcs at the top and bottom of the ring face profile. In addition, he considered the variations of the pressure with axial ring speed during the engine cycle.

With advances in computer technology, piston ring models have become faster and more complicated. In his work, Lloyd [51] assumed an off-centric parabolic ring profile and considered cyclic variations of velocity, oil viscosity, pressure, and load during an engine cycle. Ting and Mayer [78, 79] calculated the oil film thickness and used the results to predict the cylinder wear. Further research was conducted by Baker et al. [6], Hamilton and Moore [41], Allen et al. [4], and Butler and Henshall [13]. Brown and Hamilton [11] added oil starvation into a ring pack lubrication model.

Further research included the study of the influence of the piston ring profile on ring pack lubrication. Rhodes [61] demonstrated the importance of the ring face profile on the piston ring lubrication and friction. Furuhama and Hiruma [33] continued this work and determined the necessary conditions of the barrel-face ring profile lubrication. Allen at al. [4] included into their calculations the effects of varying ring face / cylinder bore inclination and viscosity variations due to changes of liner temperature along the cylinder bore. Das [22] considered the ring and the liner as two eccentric circles, and he solved the Reynolds equation using a Finite Difference Method.

The work of Dowson et al. [24] included calculations of oil film thickness, the friction force and the oil transport for a single ring as well as for a ring pack. In this study, they assumed mixed lubrication with a constant friction coefficient when the oil film thickness was smaller than a certain value. Ruddy et al. [67] examined the effect of thermal distortion and wear of piston ring grooves on ring pack lubrication.

During the 1970s, several studies were made to incorporate into the models the effect of surface roughness on ring pack lubrication [19, 20, 57, 58]. As the oil film is reduced, the sliding surfaces start to make contact with their asperities. The metal-to-metal contact between asperities takes part of the load from the lubricating fluid and causes plastic deformation of the asperities. In order to determine the area of a metal-to-metal contact, the surface asperities of a simple geometrical shape were represented mathematically. The mathematical model confirmed some of the phenomena associated with boundary lubrication.

Rohde et al. [62] studied the influence of piston ring and engine design parameters on piston ring lubrication and friction. In his later work, Rohde [63] included the effect of surface roughness into his lubrication model. His calculations showed that at the end of the stroke, most of the load is supported through the contact between asperities causing higher friction forces. Patir and Cheng [57, 58] introduced the concept of average flow to the model of partial hydrodynamic lubrication. In their approach, the asperities were treated as a statistical average with standard deviation. Recently, this approach has been incorporated into several ring pack lubrication models [76, 74, 85]. The latest trend in ring pack lubrication modeling includes the attempt to model the effect of shear stresses on viscosity or shear thinning [69, 73, 76]. In these models the lubricant viscosity is calculated based on variations of oil temperature along the cylinder liner and the rate of shear due to a contact with the sliding surface of the ring face.

The two primary goal of this dissertation can be described as further model development and model application. The model development includes the three dimensional ring twist model; the ring pack optimization routine; and the establishment of an interface between the ring pack model and the in-cylinder combustion model. This interface allows modeling of ring pack phenomena for a wide range of operating conditions as well as for a particular engine setup or configuration and is the first step toward a "virtual" engine. The three-dimensional ring twist model has the capability to predict a complicated ring motion in three-dimensional space with constraints or ring displacements. A correct modeling of ring motion allows one to predict inter-ring gas pressure and blow-by more precisely. The ring pack optimization routine helps to determine the optimal ring pack configuration with a given objective function. In addition to design analysis, it introduces a design syntheses into ring pack modeling.

In a model application, the ring pack model is applied to engine design and analysis for better understanding of physical processes associated with the ring pack. First, the model is used for prediction of processes in a specific engine setup, the Variable Displacement Engine (VDE). Second, the ring pack model is used to analyze ring pack behavior of three production engines to understand blow-by characteristics and ring dynamics for a wide range of operating conditions.

Chapter 2 THEORETICAL BACKGROUND OF INTER-RING GAS PRESSURE, RING MOTION CALCULATIONS AND PISTON RING LUBRICATION

MOTIVATION

During an engine cycle, several physical processes take place simultaneously. The piston / piston ring / combustion chamber assembly represent a complicated cyclic system consisting of multiple components. During an engine cycle, the piston moves from the Top Dead Center (TDC) to the Bottom Dead Center (BDC) and back. The pressure inside the combustion chamber changes from relatively low at the end of the exhaust stroke and during the intake stroke to high during combustion and the power stroke. Due to pressure changes inside the cylinder and pressure differences above and below the piston rings, gas flows from the cylinder into piston ring crevice volumes. Due to constant piston acceleration and decceleration as well as pressure changes above and below the rings, the piston rings change their positions relative to the piston grooves. The whole system represent a complicated system with multiple feed back loops. Figure 2 shows inter-dependencies affecting inter-ring gas pressure, blow-by, and ring motion.

Combustion rate and combustion chamber pressure, inter-ring gas pressures, and blow-by form an inter-dependent triangle. The combustion chamber pressure has a significant influence on inter-ring gas pressure and is a “driving force” for blow-by. However, for a good ring pack design, the influence of blow-by and inter-ring gas pressures on combus-

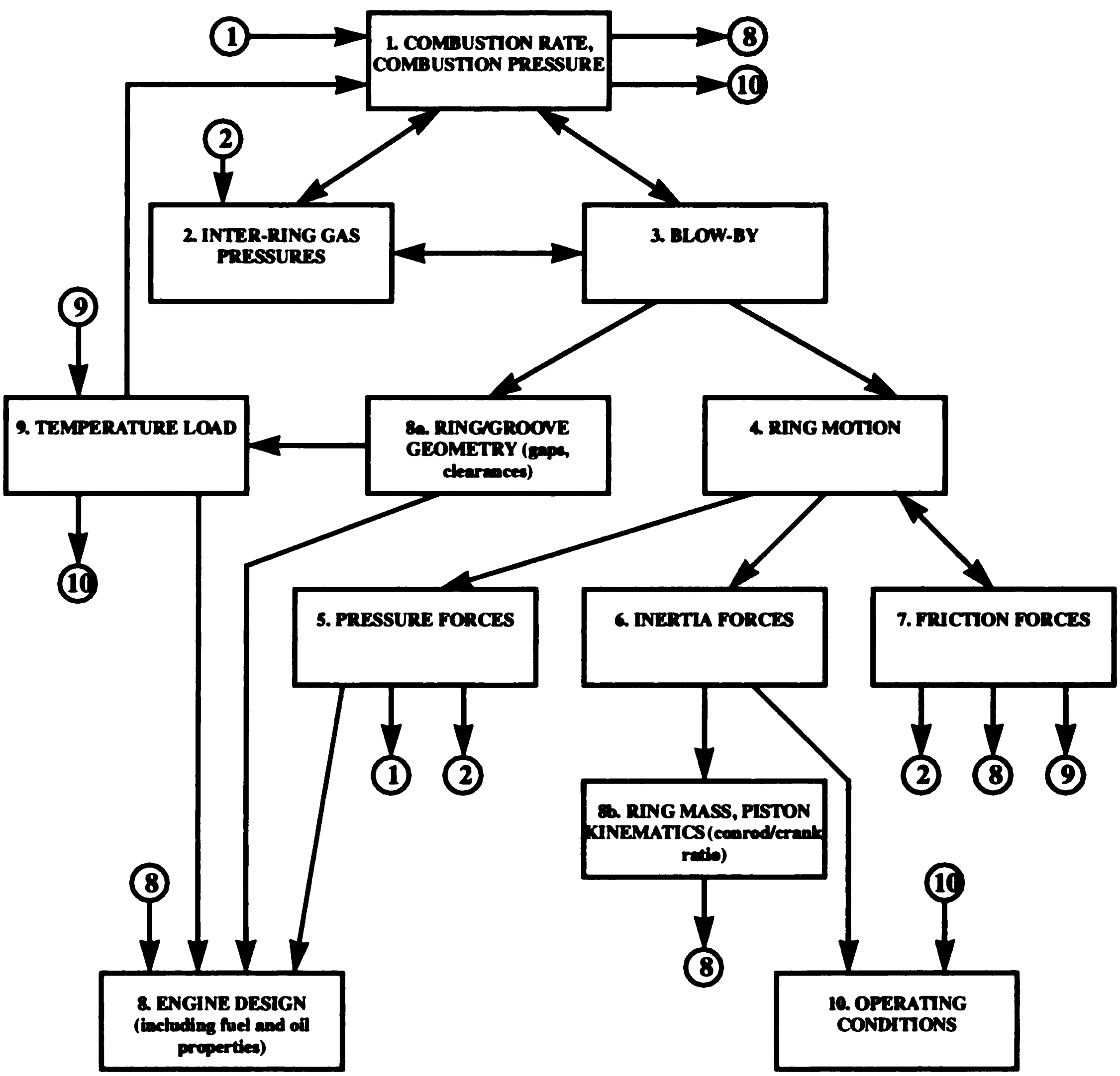

Figure 2 Inter-dependencies affecting inter-ring gas pressure, blow-by, and ring motion

tion and the combustion rate is not very significant. In the case when piston rings fail to properly seal the combustion chamber from the environment, this influence may become significant. Blow-by and inter-ring gas pressure may cause incomplete combustion and worsen engine emissions. The primary factors affecting combustion are engine design, properties of the fuel, and operating conditions. Operating conditions include engine speed and engine load.

Blow-by and inter-ring gas pressures are strongly inter-dependent. Blow-by is caused by pressure differences between piston ring crevice volumes and depends on piston / piston ring / ring groove design and ring motion. Ring motion is controlled by three primary factors: pressure load, inertia load, and friction load. The pressure load depends on in-cylinder and inter-ring pressure and ring pack design. The inertia load depends on ring mass, piston kinematics, and engine operating conditions (engine speed). The friction load damps the ring motion and depends on the ring design (ring tension, ring geometry), lubricant properties, the pressure behind the rings, and the temperature load. Temperature load affects lubricant viscosity. It is worth mentioning again that ring pack assembly represent a complicated system of relatively simple components with multiple feed back loops. In order to correctly predict inter-ring gas pressure, blow-by ring motion, and lubrication, the model has to be able to analyze these inter-dependencies interactively.

PISTON KINEMATICS

A piston / crank / connecting rod / cylinder assembly represents a reciprocating slider mechanism (Figure 3 and Figure 4). The piston kinematics depends on the length of the connecting rod L, crank radius r, and engine angular velocity ω. Considering geometri-

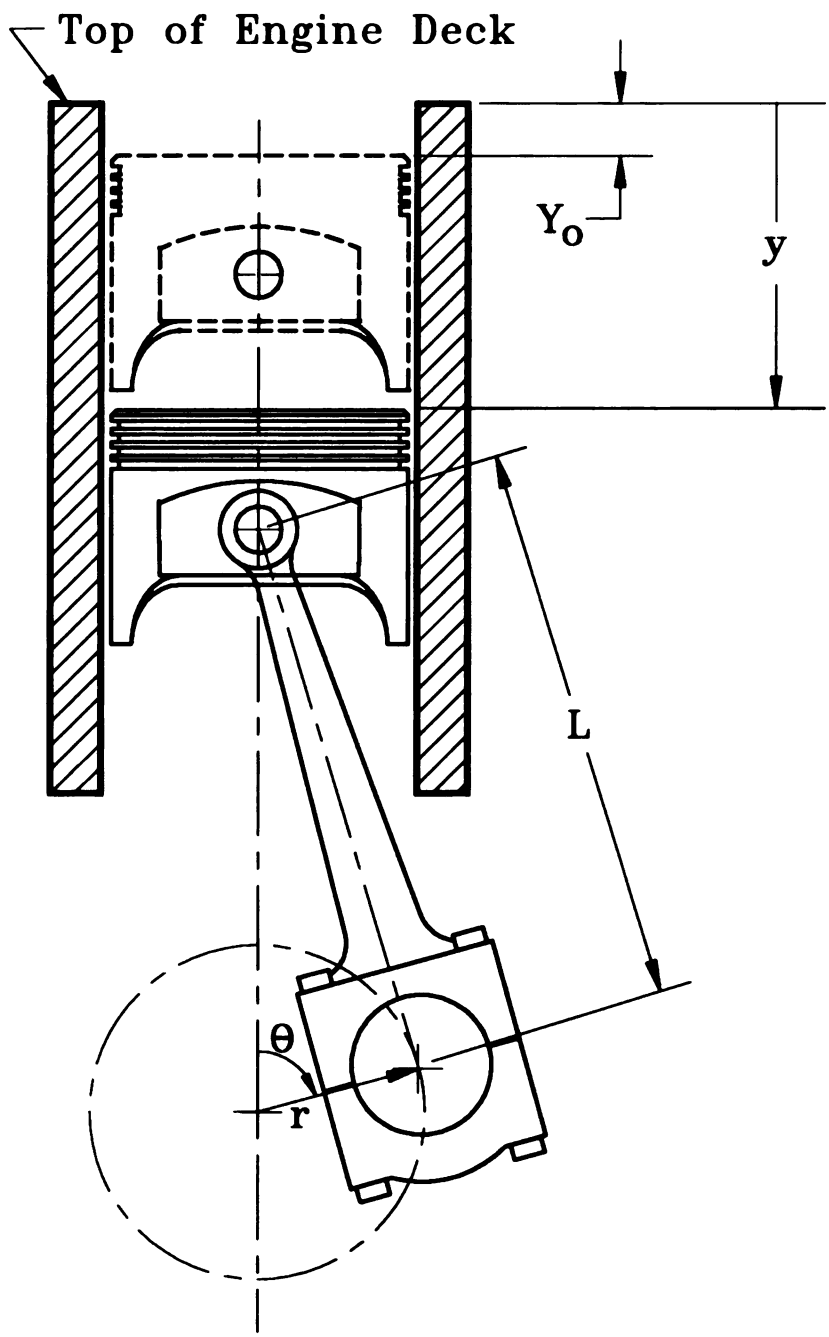

Figure 3 Piston reciprocating slider mechanism

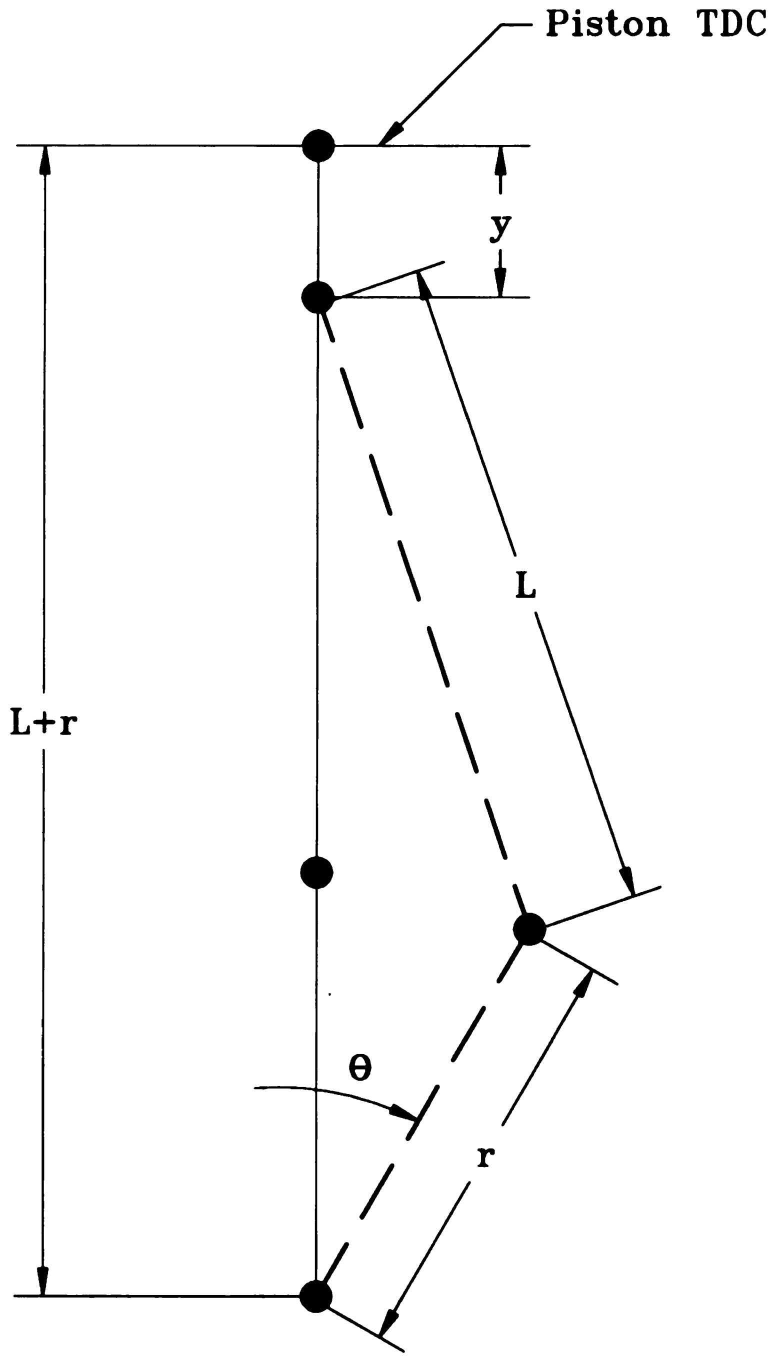

Figure 4 Schematic of crank / connecting rod assembly

cal constraints, the position of the piston at any given instant of time can be expressed as follows:

$$y = r\left[1 + \frac{L}{r} - \cos(\omega t) - \sqrt{\frac{L}{r} - \sin^2(\omega t)}\right] \tag{1}$$

where:

L	connecting rod length
r	crank radius
$\theta = \omega t$	crack angle at time t
ω	crank angular velocity
t	time

Differentiation of Eq. (1) with respect to time yields an expression for piston velocity

$$\dot{y} = r\omega\left(\sin(\omega t) + \frac{\cos(\omega t)\sin(\omega t)}{\sqrt{\frac{L}{r} - \sin^2(\omega t)}}\right) \tag{2}$$

Differentiation of Eq. (2) with respect to time yields an expression for piston acceleration

$$\ddot{y} = r\omega^2\left(\cos(\omega t) + \frac{\cos^2(\omega t)}{\sqrt{\frac{L}{r} - \sin^2(\omega t)}} + \frac{\cos^2(\omega t) \cdot \sin^2(\omega t)}{\left(\frac{L}{r} - \sin^2(\omega t)\right)^{3/2}} - \frac{\sin^2(\omega t)}{\sqrt{\frac{L}{r} - \sin^2(\omega t)}}\right) \tag{3}$$

It is worth mentioning that due to geometry constraints of a reciprocating slider mechanism, piston kinetics do not a follow pure sinusoidal motion.

INTER-RING GAS PRESSURES

Inter-ring gas pressures are calculated based on the quasi-steady orifice volume flow model. The key assumptions can be summarized as follows. Gas is assumed to follow the ideal gas law.

$$P \cdot V = m \cdot R \cdot T \tag{4}$$

where:

P pressure

V gas volume

m gas mass

R gas constant

T gas temperature

Another assumption is that the flow is laminar because of a low Reynolds number. There are three main paths for gas flow across the ring: through the ring end gap, between the ring face and cylinder liner, and behind the ring. A schematic of the crevice volumes and gas flow paths is shown in Figure 5. The mass flow rates between the volumes are calculated based on the law of conservation of mass using a quasi-steady flow model

$$\Sigma\dot{m}_{in} - \Sigma\dot{m}_{out} = \frac{dm}{dt} \tag{5}$$

where:

$\dot{m}_{in}$ mass flow rate in

$\dot{m}_{out}$ mass flow rate out

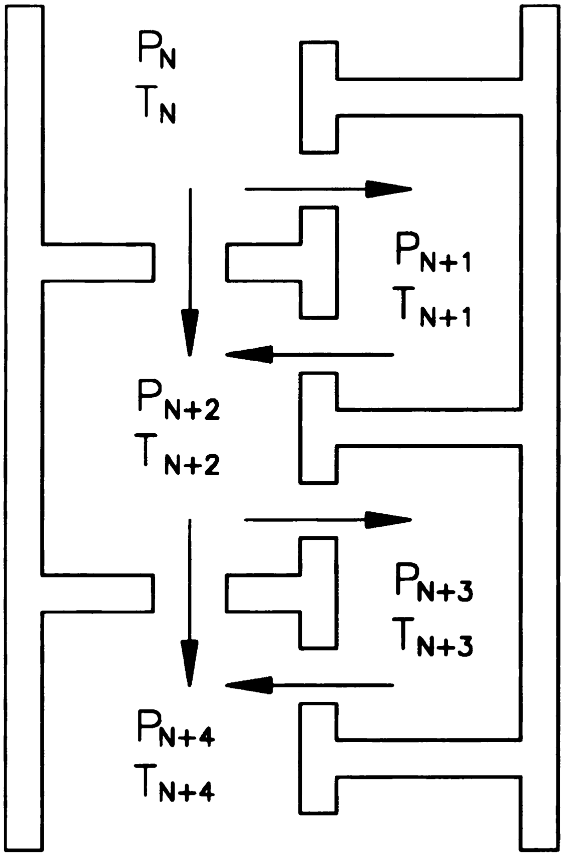

Figure 5 Piston ring crevice volumes and gas flow paths

$\frac{dm}{dt}$ rate of mass change

The mass flow rate through an orifice between volumes 1 and 2 is calculated as follows:

$$\dot{m} = K_c A \sqrt{\frac{2\gamma}{R(\gamma-1)}}\left(\frac{P_1}{\sqrt{T_1}}\right)\left(\frac{P_2}{P_1}\right)^{\frac{1}{\gamma}}\sqrt{1-\left(\frac{P_2}{P_1}\right)^{\frac{\gamma-1}{\gamma}}} \qquad (6)$$

where:

$\dot{m}$	mass flow rate
A	flow area
P	pressure
T	temperature
$\gamma = 1.3$	ratio of specific heats of the gas
K_c	orifice discharge coefficient

The pressure P_c, at which the ratio of $\left(\frac{P_c}{P_1}\right)$ yields the maximum mass flow rate corresponds to a critical pressure. The critical pressure can be found as follows:

$$\frac{P_c}{P_1} = \left(\frac{2}{\gamma + 1}\right)^{\frac{\gamma}{\gamma - 1}} \tag{7}$$

For air at normal conditions $\gamma = 1.4$ and correspondingly $\left(\frac{P_c}{P_1}\right) = 0.528$. For combustion gases passing through the ring pack $\gamma = 1.3$ and correspondingly $\left(\frac{P_c}{P_1}\right) = 0.546$.

The actual mass flow rate through the orifice is less then the theoretical flow rate due to friction losses because of the viscosity of the gas and convergence of the gas streamlines as they pass through the orifice. The orifice discharge coefficient K_c is defined as a ratio of the actual mass flow rate to the theoretical mass flow rate. An orifice discharge coefficient K_c of 0.65 is used for the inter-ring gas pressure calculations (reference [16]).

Assuming a constant crevice volume, constant gas properties, and constant gas temperature in each piston crevice volume and using Eq. (4) and Eq. (5), the pressure changes in each crevice volume can be calculated as follows

$$\frac{dP}{dt} \cdot \frac{V}{R \cdot T} = \Sigma \dot{m}_{in} - \Sigma \dot{m}_{out} \tag{8}$$

An extensive correlation between measured inter-ring gas pressures and the inter-ring gas pressures predicted by the gas-dynamic model with a good agreement can be found in reference [26].

RING MOTION

During an engine cycle, the ring is subject to different types of loads due to friction, a pressure difference above and below the ring, piston acceleration and decceleration, and others. These forces cause the ring to move inside its groove. Piston ring motion includes two primary components: axial motion and radial motion. The third component, rotation of the ring, has a time scale of a high order of magnitude and is not considered.

Ring Axial Motion

Axial ring motion is calculated by solving an equation of Newton's second law

$$m_r \ddot{x} = \Sigma F_i \tag{9}$$

where:

m_r mass of the ring

$\ddot{x}$ axial acceleration of the ring

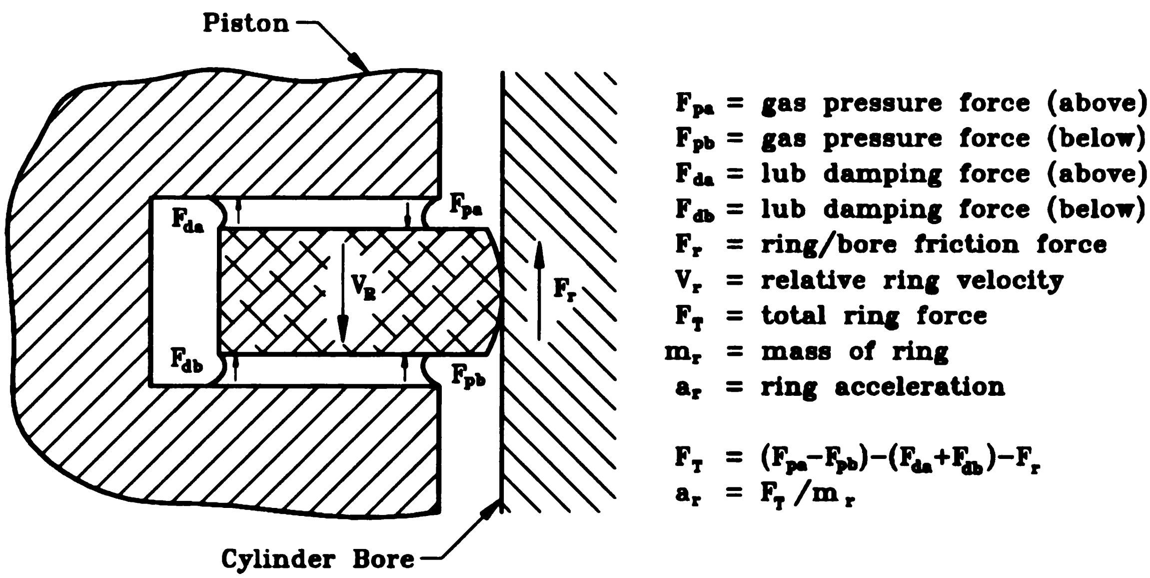

Figure 6 Forces acting on the ring

F_i applied force acting in the axial direction

There are four primary forces acting on the ring: pressure force, inertia force, friction force, and lubricant damping forces. The schematic of the forces acting on the ring is shown in Figure 6.

The pressure force can be expressed as follows:

$$F_P = A_T \cdot p_T - A_B \cdot p_B \tag{10}$$

F_P pressure force

A_T area on which the pressure above the ring acts

p_T pressure above the ring

A_B area on which the pressure below the ring acts

p_B pressure below the ring

Depending on the position of the ring inside the groove, there can be different pressure distributions acting above and below the ring. The ring can be at the top of the groove, at the bottom of the groove, or be floating in the groove. Depending on the ring position in the groove, the ring opens or closes areas for gas flow above or below the ring. These areas affect mass flow rates across the ring pack. Figure 7 shows the three possible positions in the groove and the pressure forces the ring experiences in these three cases.

The inertia force acting on the ring depends on the ring mass and ring acceleration. When the ring is in contact with the top or bottom of the groove, the ring acceleration is equal to the piston acceleration (Eq. (3)). When the ring is floating in the groove, the ring acceleration depends on the forces acting on the ring. The inertia force can be expressed as follows:

$$F_I = -m_r \cdot a_r \tag{11}$$

where:

m_r mass of the ring

a_r acceleration of the ring

The friction force between the ring face profile and the cylinder liner, as shown in Figure 8, is approximated by:

$$F_F = p(\pi D t) f \tag{12}$$

where:

p pressure acting on the ring

D bore diameter

t axial ring thickness

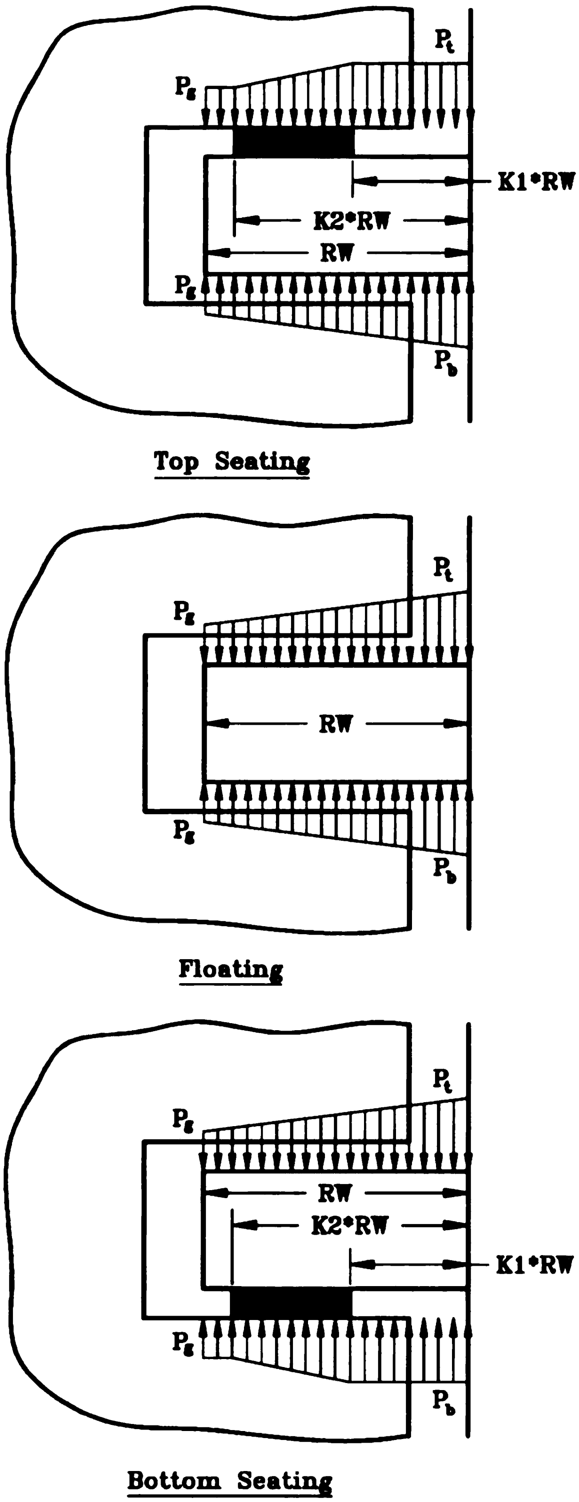

Figure 7 Ring position in the groove

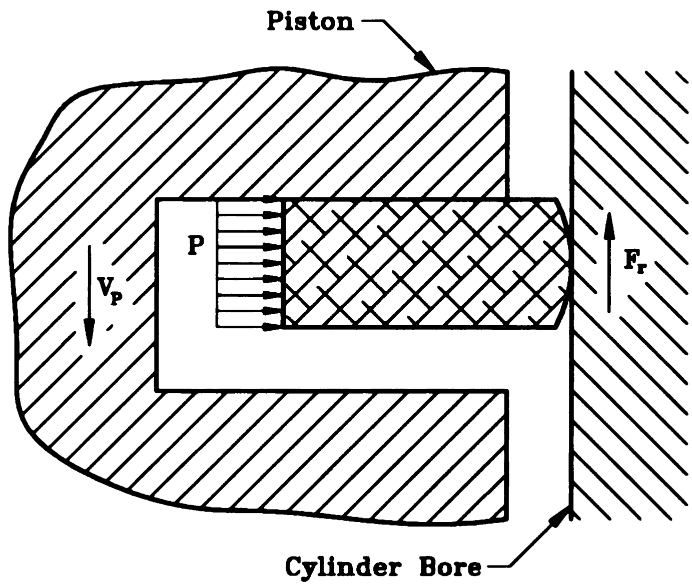

Figure 8 Ring / cylinder liner friction force

f friction coefficient

According to reference [16], the friction coefficient is calculated based on an empirical fit as follows:

$$f = 4.8\sqrt{\frac{\mu V_p}{p}} \tag{13}$$

where:

μ lubricant viscosity in (*reyn*)

V_p ring velocity in $\left(\frac{in}{s}\right)$

p pressure acting on the ring in (*psi*)

Typically, the friction forces are much smaller than inertia or pressure forces.

The lubricant damping forces acting on the ring include the ring squeeze damping force S and the ring adhesive damping force Q. The ring squeeze damping force is given by:

$$S = f_s \mu \dot{h} A \cdot \frac{(R_p - R_r)^2}{h^3} \tag{14}$$

where:

f_s reduction parameter for squeeze film force ($0 \le f_s \le 1$)

μ lubricant viscosity

$\dot{h}$ relative velocity of ring with respect to groove

A wetted Area $A = \pi(R_p^2 - R_r^2)$

h side clearance between ring and groove

The ring adhesive damping force is given by

$$Q = f_a P_{atm} A \tag{15}$$

where:

f_a reduction parameter for adhesive force ($0 \le f_a \le 1$)

P_{atm} atmospheric pressure

A wetted area $A = \pi(R_p^2 - R_r^2)$

The groove geometrical constraints on the ring motion are enforced by using a coefficient of restitution [68]. With a coefficient of restitution, the ring velocity right after the impact with the groove wall is calculated as

$$V_a = -r \cdot V_b \tag{16}$$

where:

V_a ring velocity before the impact

V_b ring velocity after the impact

r coefficient of restitution ($0 \le r \le 1$)

The other way to enforce groove geometrical constraints is to apply a contact force at the moment of impact [68]. The main advantage of using a coefficient of restitution is avoidance of numerical difficulties associated with stiff problems. Non-stiff problems allow the use of simpler and more reliable numerical algorithms with better convergence [75, 74, 1, 60].

Ring Radial Motion

During an engine cycle for most operating conditions, the ring stays in contact with the cylinder liner due to ring tension and pressure load from behind the ring on one side and liner contact reaction force and lubricant pressure force on the other. Under certain conditions, the lubricant pressure force may overcome the force due to ring tension and pressure behind the ring, causing ring collapse.

For most operating conditions, at the end of the compression stroke and during most of the power stroke, the top ring stays at the bottom of the groove. This happens because the pressure forces exceed the inertia forces. This is shown in Figure 9. At low engine load and high engine speed, the inertia forces may dominate the pressure forces and the top ring stays at the top of the groove during combustion. If the pressure above the ring is high enough and the pressure behind the ring is low enough, the ring may lose con-

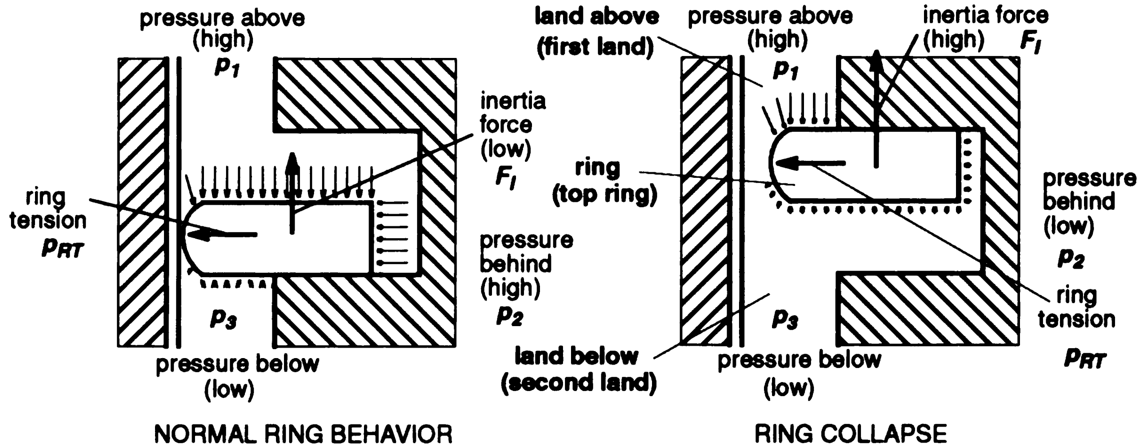

Figure 9 Ring collapse conditions

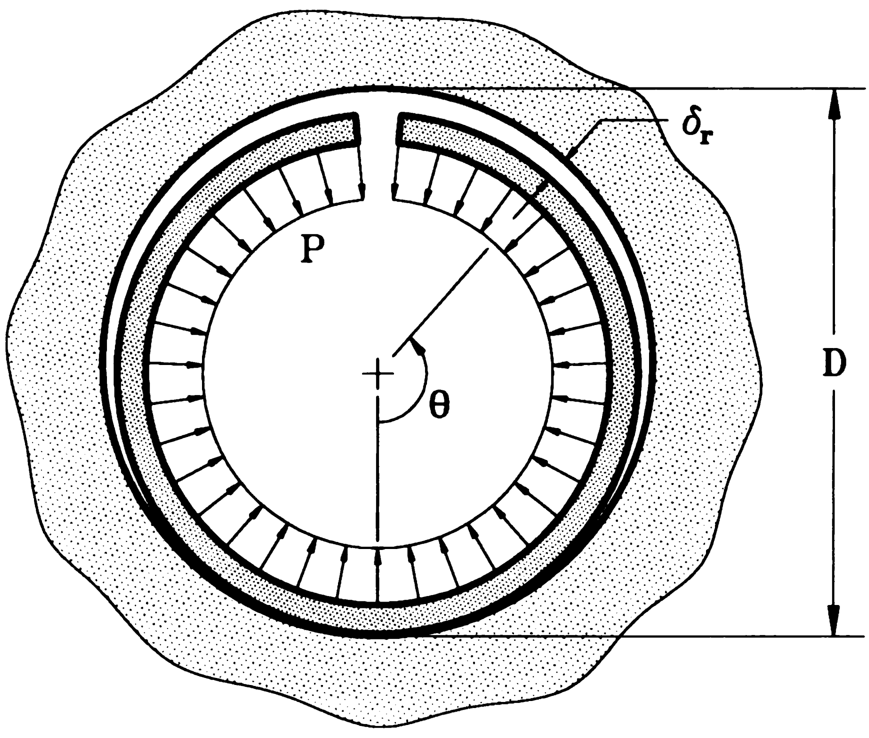

Figure 10 Ring radial displacement and gas flow area due to ring collapse

tact with the cylinder bore and open a large area for gas flow. For ring collapse to occur, the following conditions of inertia forces, pressure above the ring, pressure behind the ring, and ring tension must be fulfilled:

$$\left(\frac{p_1 + p_3}{2}\right) > p_{RT} + p_2 \tag{17}$$

$$A_3 \cdot p_3 + m_r \cdot \ddot{x} > A_1 \cdot p_1 \tag{18}$$

Rearranging Eq. (17) and Eq. (18) yields the following.

$$m_r \cdot \ddot{x} > 2p_{RT} \cdot A_1 + p_3 \cdot (A_1 - A_3) \tag{19}$$

where:

A_1 area above the ring

A_2 area behind the ring

A_3 area below the ring

m_r mass of the ring

p_1 pressure above the ring

p_2 pressure behind the ring

p_3 pressure below the ring

p_{RT} pressure due to ring tension

$\ddot{x}$ axial ring acceleration

It can be seen that ring acceleration $\ddot{x}$ depends on the engine speed ω and slider - crank geometry, crank radius r and connecting rod length L. On the other hand, the area A_1 and A_3 as well as the ring mass m_r depend on the ring design and the bore diameter.

The ring radial displacement (Figure 10) can be calculated as

$$\delta_r = \frac{pR^4}{EI}\left(1 - \cos\theta + \frac{\theta}{2}\sin\theta\right) \tag{20}$$

where:

δr radial displacement

p total pressure

R mean radius of the ring

E ring modulus of elasticity

I moment of inertia of the ring section

θ reference angle

An additional gas flow area between the ring face and the cylinder liner due to ring radial displacement is given by

$$A = \frac{2pR^5}{EI}\left(\frac{3\pi}{2}\right) = 9.4248\frac{pR^5}{EI} \tag{21}$$

with a maximum feasible gas flow area of

$$A_{max} = R \cdot d_{ec} \tag{22}$$

where:

A gas flow area due to ring collapse

A_{max} maximum gas flow area due to ring collapse

p total pressure

R mean radius of the ring

E ring modulus of elasticity

I moment of inertia of the ring section

d_{ec} ring end gap clearance

STATE SPACE REPRESENTATION

For inter-ring gas pressure and ring motion calculations, the governing equations of inter-ring gas pressure and mass flow rates (Eq. (8)) and ring motion (Eq. (9)) have to be solved simultaneously. These equations can be represented in a state space form as

$$\{\dot{x}\} = F(\{x\}, \{z\}, t) \tag{23}$$

where:

$\{\dot{x}\}$ time derivative of state vector

$\{x\}$ state vector

F state space function vector

$\{z\}$ design variable vector

t time

Eq. (23) is solved through crank angle iterations employing the explicit forward difference scheme [1 and 60]. For the forward difference scheme, a derivative is approximated as

$$\left(\frac{\partial f}{\partial x}\right)_j^n \approx \frac{f^n{}_{j+1} - f^n{}_j}{\Delta x} \tag{24}$$

PISTON RING LUBRICATION

During an engine cycle, the piston ring face is always in contact with oil film on the cylinder liner. Depending on oil film thickness, there are three distinct regions of piston ring lubrication: boundary, mixed, and hydrodynamic. When there is enough oil film to avoid surface-to-surface contact, the lubrication is in the hydrodynamic regime. When the oil film is not thick enough to avoid the surface-to-surface contact, the lubrication is in the boundary regime. The intermediate regime between hydrodynamic and boundary lubrication is called mixed lubrication. The oil film development between the ring face and the cylinder liner for hydrodynamic lubrication is modeled with the Reynolds equation. The general form of the three-dimensional Reynolds equation is the following:

$$\frac{\partial}{\partial x}\left(\frac{h^3}{\mu}\frac{\partial p}{\partial x}\right) + \frac{\partial}{\partial z}\left(\frac{h^3}{\mu}\frac{\partial p}{\partial z}\right) = -6U\frac{\partial h}{\partial x} - 6W\frac{\partial h}{\partial z} + 12V \tag{25}$$

where:

p	lubricant pressure
μ	lubricant dynamic viscosity
h	lubricant thickness
U	ring axial velocity
W	ring tangential velocity
$V = \frac{dh}{dt}$	ring radial velocity

An axisymmentric case of piston ring lubrication (Figure 11) can be simplified to a two-dimensional form of the Reynolds equation

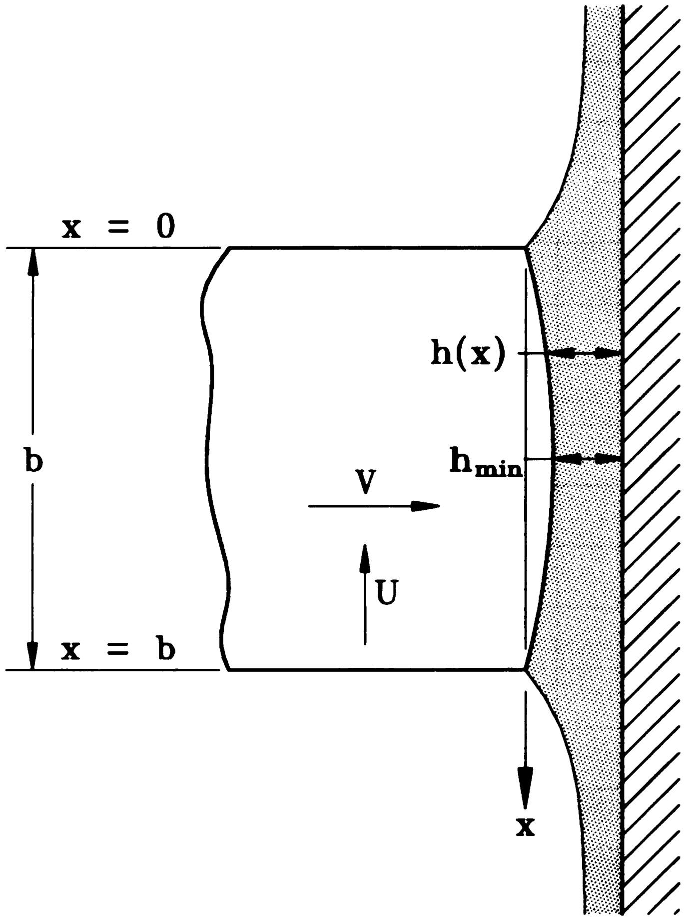

Figure 11 Piston ring lubrication

$$\frac{\partial}{\partial x}\left(\frac{h^3}{\mu}\frac{\partial p}{\partial x}\right) = -6U \cdot \frac{\partial h}{\partial x} + 12V \qquad (26)$$

The Reynolds equation is valid for piston ring lubrication under the following conditions: body forces are negligible; fluid inertia is negligible; the lubricant pressure is constant through out the thickness of the film; the lubricant is Newtonian; flow is laminar; there is no slip at the boundaries (reference [77]). Assuming that the lubricant viscosity is constant through out the oil film thickness with a mean viscosity μ, Eq. (26) can be written as

$$\frac{\partial}{\partial x}\left(h^3\frac{\partial p}{\partial x}\right) = -6\mu U \cdot \frac{\partial h}{\partial x} + 12\mu V \tag{27}$$

Assuming that the surfaces of the ring and the liner are rigid, the integration of Eq. (27) yields

$$p = AI_1 + B\frac{\partial h}{\partial t}I_2 + CI_3 + D \tag{28}$$

where:

$$A = -6\mu U \tag{29}$$

$$B = 12\mu \tag{30}$$

$$I_1 = \int\frac{dx}{h^2} \tag{31}$$

$$I_2 = \int\frac{x}{h^3}dx \tag{32}$$

$$I_3 = \int\frac{dx}{h^3} \tag{33}$$

C integration constant

D integration constant

The integration constants C and D are found from the boundary conditions. Generally, three types of boundary conditions are considered [10, 77]. The three types of boundary conditions are shown in Table 1. Typically, the Half-Sommerfeld or Reynolds boundary conditions give satisfactory results for piston ring lubrication. However, the most appropriate boundary conditions for piston ring lubrication have not been determined yet (reference [77]).

Table 1 Lubrication boundary conditions

Position	Sommerfeld	Half-Sommerfeld	Reynolds
$x = 0$	$p = P1$	$p = P1$	$p = P1$
$x = b/2$	—	$p = 0$	—
$x = b$	$p = P2$	—	$p = P2$, $dp/dx = 0$

Even though lubricant viscosity is assumed to be constant through out the oil film thickness between the cylinder liner and the ring face, it changes along the cylinder liner due to cylinder bore temperature variations. Many viscosity / temperature variation formulas have been proposed [10, 77]. Vogel's formula is a three-constant equation

$$\mu = \alpha \cdot e^{\frac{b}{(t + c)}} \tag{34}$$

Slotte's formula:

$$\mu = \frac{\alpha}{(b + t)^c} \tag{35}$$

Reynolds' formula:

$$\mu = k \cdot e^{-\alpha t} \tag{36}$$

Typical values for viscosity and coefficients α, b, and c for the SAE graded oils are shown in Table 2 [17].

Table 2 Viscosity and Vogel constants of the SAE graded oils

SAE Grade	Viscosity (cP)			Vogel constants		
	25° C	40° C	100° C	α	b	c
5W	41.45	21.66	4.06	0.05567	900.0	110.8
10W	76.21	37.06	5.63	0.04082	1066.0	116.5
15W	89.66	41.56	6.07	0.06681	902.0	100.2
20W	229.47	98.73	10.50	0.02370	1361.0	123.3
20	113.52	51.83	6.98	0.04987	1028.0	108.0
30	229.47	98.73	10.50	0.02370	1361.0	123.3
40	321.65	133.12	13.50	0.07227	1396.0	121.7
50	574.46	222.52	17.99	0.01963	1518.0	122.6

Piston ring friction forces are calculated based on the regime of piston ring lubrication. For hydrodynamic lubrication, the friction force between the cylinder liner and the ring face per unit area due to lubricant shear is calculated as follows:

$$f_x = \frac{h}{2} \cdot \left(\frac{dp}{dx}\right) + \frac{\mu U}{h} \qquad (37)$$

where:

h lubricant thickness

μ lubricant viscosity

U ring axial velocity

$\frac{dp}{dx}$ lubricant pressure gradient with respect to the axial coordinate x.

After integrating Eq. (37) over ring thickness HR and around the bore circumference, the total friction force is found as follows:

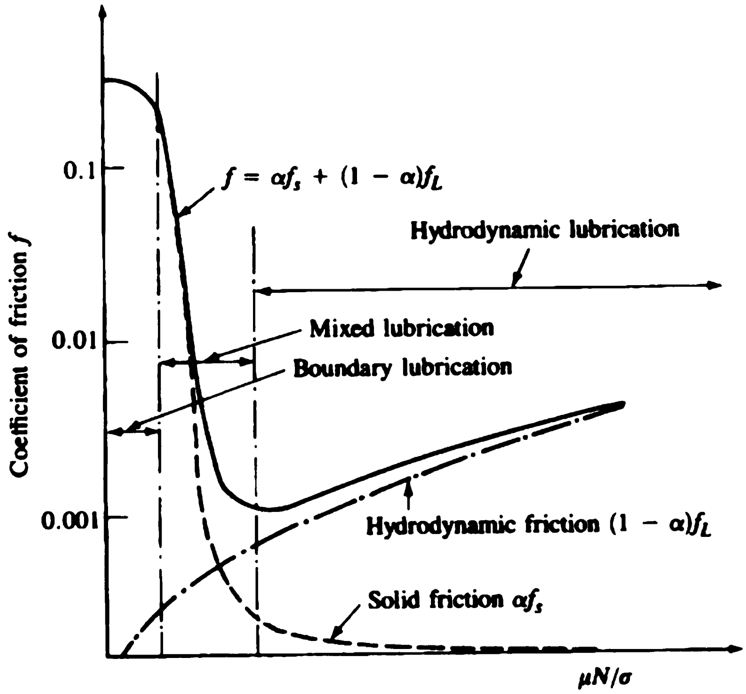

Figure 12 Stribek diagram for journal bearing: coefficient of friction f versus dimensionless duty parameter $\mu N/\sigma$, where μ is the lubricant dynamic viscosity, N is the relative velocity, σ is the loading force per unit area

$$F_x = \int_0^{2\pi} \int_0^{H_R} R \cdot f_x \, dx \, d\theta \tag{38}$$

where:

F_x friction force in axial direction

f_x hydrodynamic friction force per unit area

R cylinder bore radius

H_R axial ring thickness

When the oil film is not thick enough to develop hydrodynamic lubrication, the piston ring lubrication is in the mixed regime. For this case, the friction force is calculated as follows:

$$F_x = c \cdot F_{total} \tag{39}$$

where:

F_x friction force in axial direction

c coefficient of friction

The friction coefficient c is computed based on the parameters in the Stribek diagram (Figure 12 from reference [45]).

F_{total} normal lateral load of the piston ring (lubricant capacity between the ring and the cylinder liner)

The total friction force work W_p is calculated by integrating the friction force over the engine cycle as follows:

$$W_p = \int_0^S F_x ds \tag{40}$$

Chapter 3 SIMULATION ANALYSIS OF RING PACK BEHAVIOR IN A DEACTIVATED CYLINDER

MOTIVATION

Improvements in engine efficiency can be pursued in many ways. One of them is cylinder deactivation. The cylinder is deactivated under certain operating conditions by cutting off the fuel supply and shutting the valves off. This chapter presents the results of a simulation analysis of the ring pack behavior, inter-ring gas pressure, ring-pack breathing, and oil film thickness associated with cylinder deactivation. All of these parameters are interconnected and have a strong influence on oil consumption.

This chapter is subdivided into two parts. The first part discusses fast transient behavior of the deactivated cylinder due to heat transfer after the valves were shut off. In this part, the influence of temperature drop, ring pack-blow-by, and ring pack performance were studied. The second part presents results of slow transient processes in the deactivated cylinder due to ring pack breathing with constant temperature conditions. The main objective of this analysis was the investigation of the influence of blow-by on ring pack behavior and oil consumption.

In this analysis the RING program [16, 17, and 10] and the General Engine SIMulation program (GESIM) [30, 8, 23, 55, and 72] were used. The RING program is one of the programs in the Cylinder kit Analysis System for Engines (CASE). The GESIM program is a part of the Ford ENGine SIMulation system (ENGSIM). GESIM is a computational tool for modeling in-cylinder processes in an internal combustion engine. It simulates in-cylinder flow, heat transfer, and thermodynamics during the engine cycle for firing, as well as motoring conditions. The program accounts for heat transfer losses from the combustion chamber during breathing, compression, expansion, and from both burned and unburned gases during combustion.

FAST TRANSIENT BEHAVIOR ANALYSIS OF CYLINDER DEACTIVATION

In this analysis the performance of the deactivated cylinder was investigated. During deactivation the exhaust valve does not open at the end of the expansion stroke, and the burned gas is kept trapped inside the cylinder. This causes a high pressure increase for the next cycle and an ensuing pressure decay for the following cycles (Figure 13). The pressure increase is due to the following: under firing conditions, the peak in-cylinder pressure occurs after the piston passes the top dead center (TDC) when most of the charge has been burned. When the valves are shut off, all the burned gases are trapped inside the cylinder and compressed as the piston approaches TDC again. The cause of the pressure decay was hypothesized to be either heat transfer or ring pack breathing; these events were studied using RING and GESIM simulations which are discussed below.

Heat transfer was determined as the main factor causing the temperature drop. The influence of ring pack breathing on the pressure change during the first several cycles was small and can be neglected. Based on this conclusion, the following simulation strategy was chosen. GESIM was used to model a combustion chamber pressure trace for every

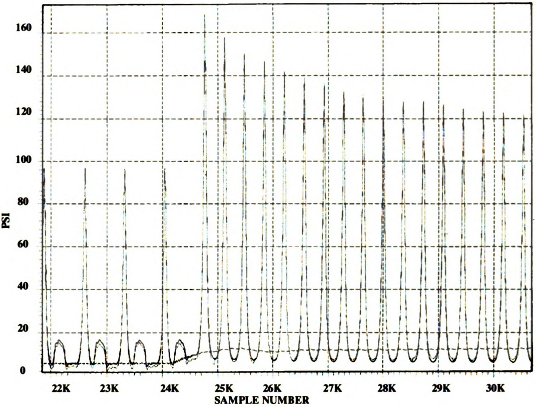

Figure 13 Experimental combustion chamber pressure traces of the deactivated cylinder obtained from Ford Motor Company

cycle considering the heat transfer losses from the combustion chamber to the walls. With this combustion chamber pressure, the RING program was used to perform gas dynamic and lubrication analysis to predict inter-ring pressures, ring pack breathing (blow-by), ring behavior, and oil film thickness.

For the analysis of the cylinder deactivation processes, several simulations were performed with the same initial conditions but different engine speeds: 1500, 2000, 2500, 3000, and 3500 rpm. Figure 14, Figure 15, Figure 16 and Figure 17 show the pressure traces for 1500 rpm and 3500 rpm with different scale resolutions. The following discussion refers to the simulation points of 1500 and 3500 rpm.

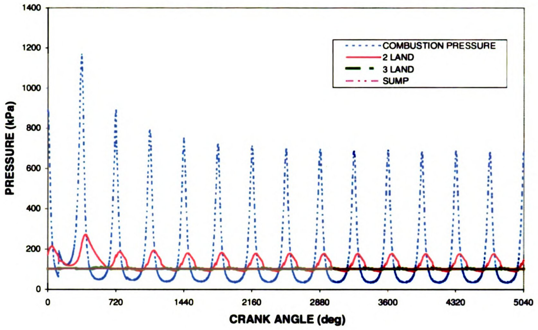

Figure 14 Pressure traces of the cylinder deactivation transient process for seven cycles at 1500 rpm

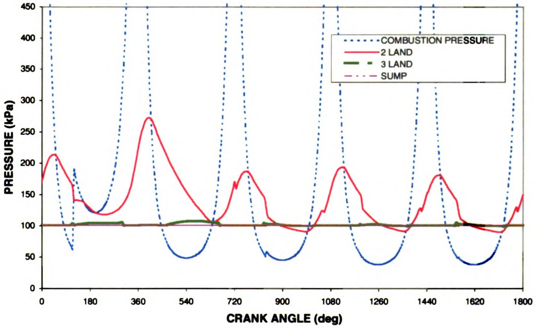

Figure 15 Pressure traces of the cylinder deactivation transient process at 1500 rpm

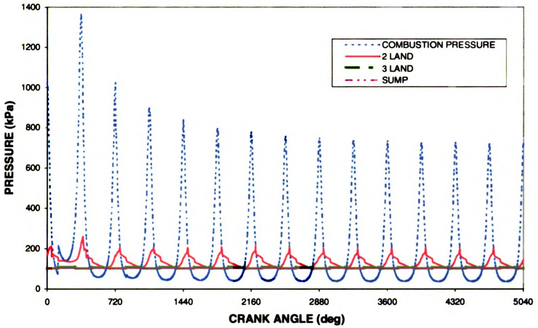

Figure 16 Pressure traces of the cylinder deactivation transient process for seven cycles at 3500 rpm

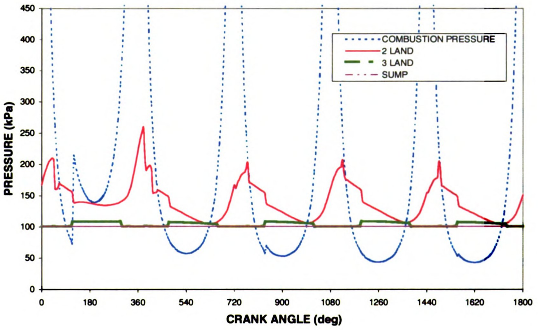

Figure 17 Pressure traces of the cylinder deactivation transient process at 3500 rpm

The duration of the fast transient of the deactivation peak cylinder pressure was determined to be seven cycles. The combustion chamber pressure achieves a steady state amplitude after the seventh cycle. As seen in Figure 14 and Figure 16, the pressure traces for the sixth and seventh cycles are only slightly different. During the first seven cycles, constant boundary conditions (such as cylinder liner temperature) are assumed. As the cylinder liner temperature and gas pressure change during the motoring process, future work should include analysis of how these temperature changes influence boundary conditions. For this study, the oil conditions, such as temperature during the simulations, were assumed to be constant.

In general, the results show changes from 1500 rpm to 3500 rpm during the first three cycles for the ring-pack pressures. After the seventh cycle these pressures reach a steady state amplitude. The second land pressure shows significant differences between the two speeds (Figure 15 and Figure 17). At 3500 rpm, the pressure on the second land cannot build up in the same way as the 1500 rpm case due to a different ring motion of the second ring. The inertial force on the ring at 3500 rpm overcomes the pressure force on the top of the second ring and initiates ring motion towards the top of the groove, allowing the second land pressure to decrease (Figure 17). Due to high pressure inside the combustion chamber and on top of the first ring, this ring is held at the bottom of the groove. This will change with higher acceleration forces at higher engine speeds. The positive effect of this lower pressure on the second land at 3500 rpm results in a decreased back flow into the combustion chamber and smaller oil consumption.

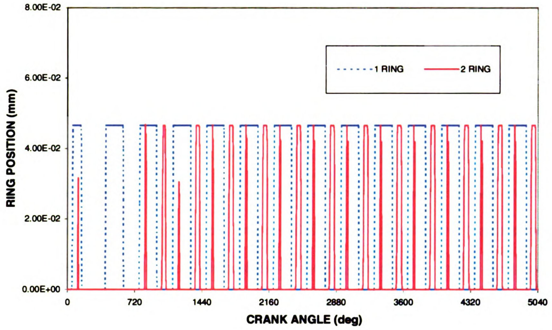

Figure 18 Top and second ring motion of the cylinder deactivation transient at 1500 rpm

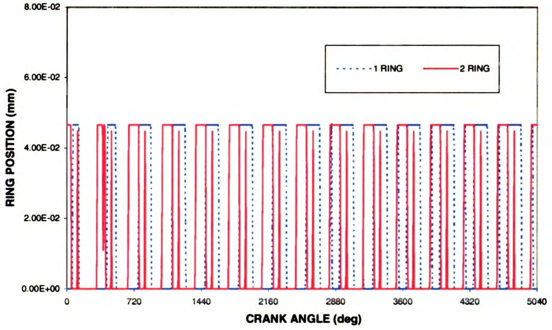

Figure 19 Top and second ring motion of the cylinder deactivation transient at 3500 rpm

Ring Motion

Ring motion is influenced by variations in inter-ring pressure and mass flow. During the cycle, the ring moves from the top to the bottom of the groove due to inertia and a pressure difference above and below the ring. This motion opens a passage behind the ring for gas flow. The gas flow affects the inter-ring pressure and consequently the ring motion. Figure 18 and Figure 19 show the motion of the compression rings for seven cycles at 1500 rpm and 3500 rpm respectively. In general, it is preferable to have the rings move uniformly without oscillations (fluctuations) in the ring groove. As shown later, movements in the ring position were found to correlate with high mass flow rates through the ring pack. However, some ring fluctuations do occur. For both engine speeds the top ring shows fewer fluctuations than the second ring. These fluctuations are shown as spikes in Figure 19. The fluctuations reduce ring pack sealing, and they cause abrupt changes of the inter-ring gas pressure and mass flow spikes at 3500 rpm and will be discussed later.

The ring motion shows transient behavior during the first three cycles. After the third cycle, as the peak pressure stabilizes, the ring follows a similar pattern for succeeding cycles.

Mass Flow and Back Flow

During a cycle the gas passes from the combustion chamber through the ring pack into the crank case and from the ring pack into the combustion chamber. The direction of back flow is from the ring pack into the combustion chamber. The direction of the forward flow and net flow is from the combustion chamber into the crankcase. The net flow is a difference between the back flow and the forward flow over a cycle.

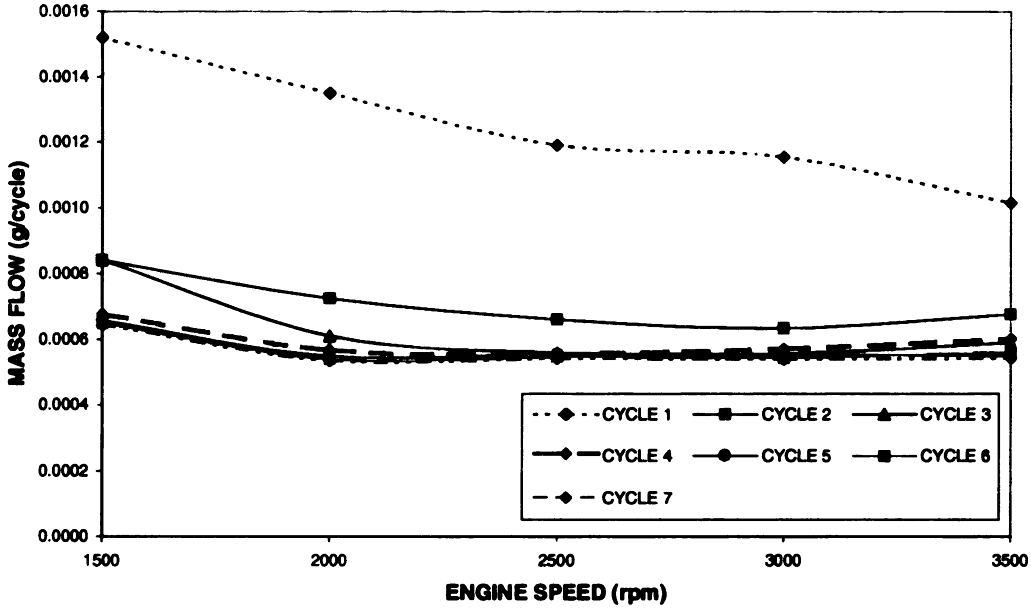

Figure 20 Averaged cycle based mass flow from the cylinder during the cylinder deactivation transient

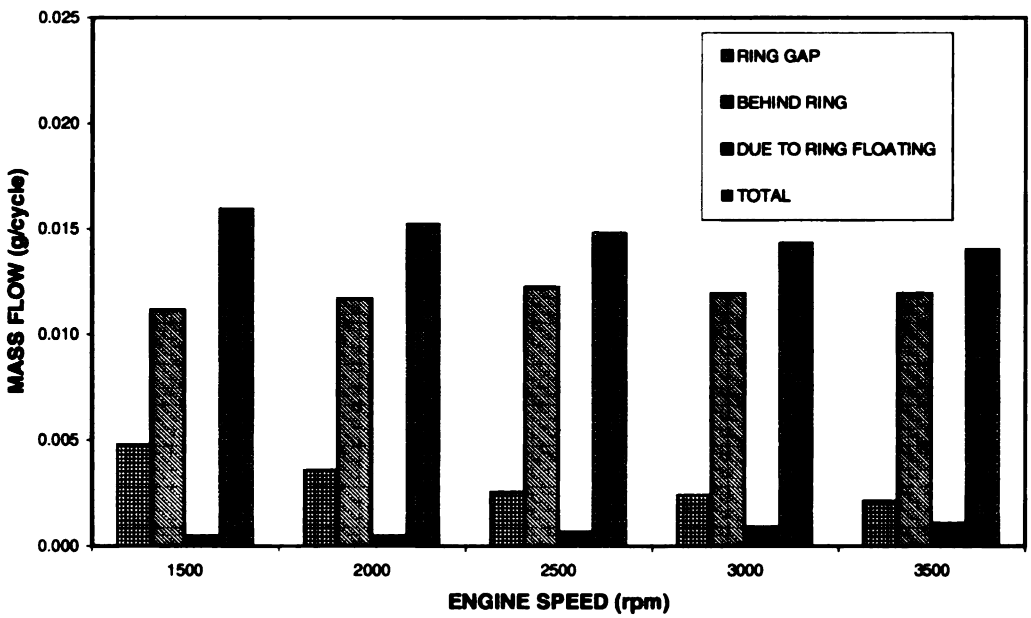

Figure 21 Cycle based back flow into the cylinder through the ring gap, behind the ring, and total

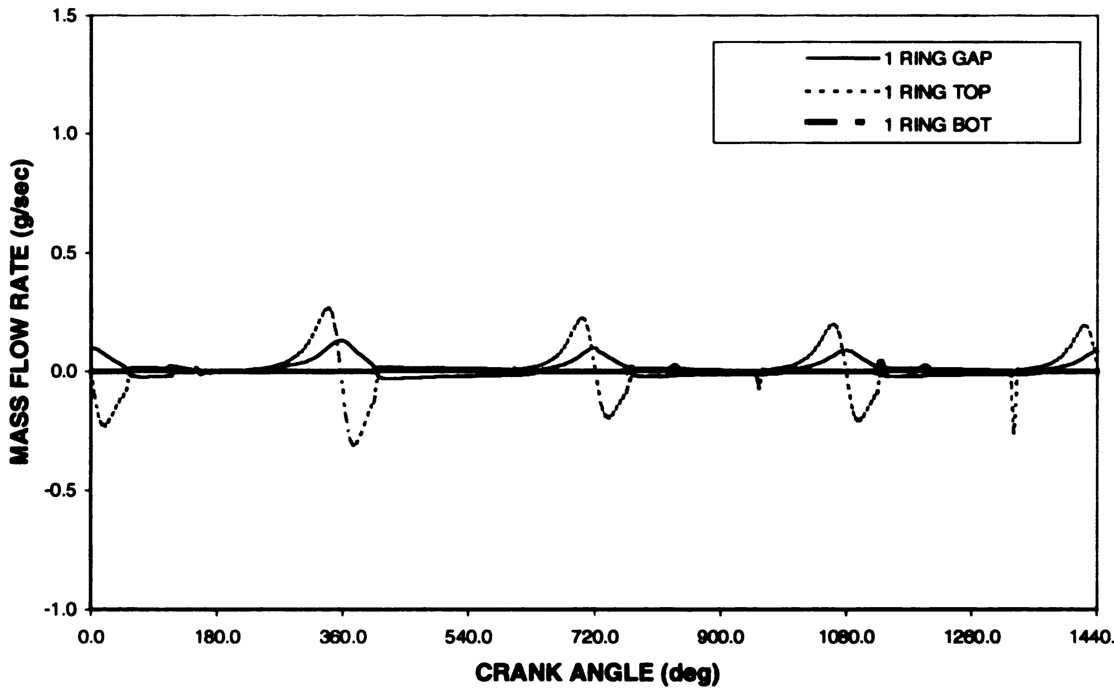

Figure 22 Mass flow rate through the ring groove at 1500 rpm

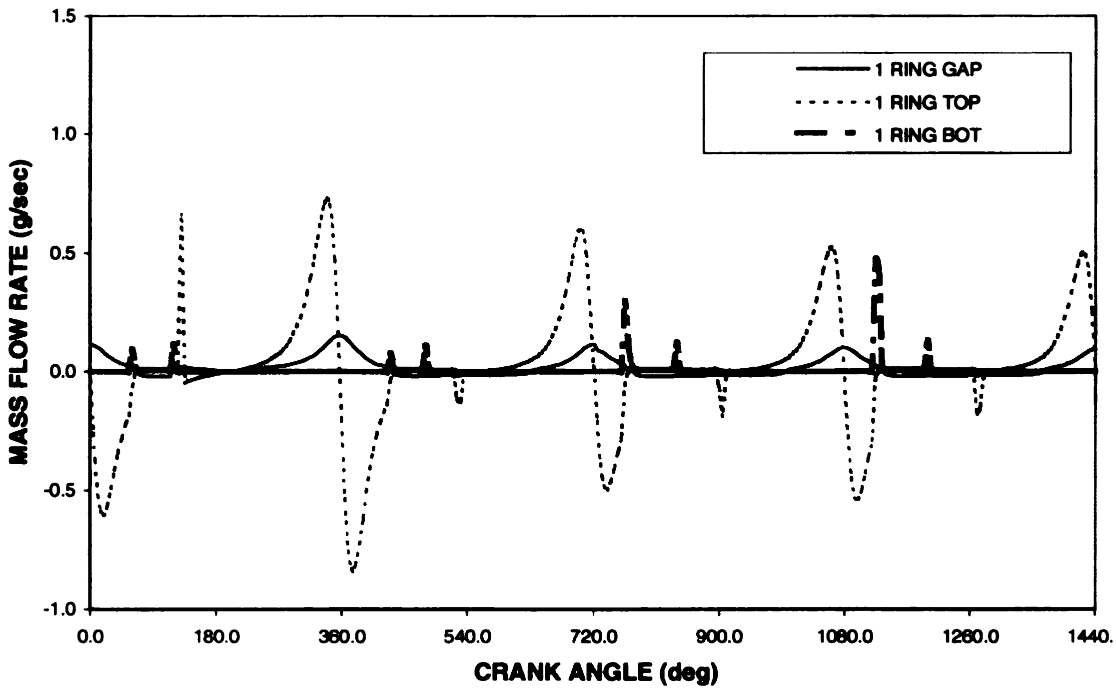

Figure 23 Mass flow rate through the ring groove at 3500 rpm

Mass flow between the volumes in the ring pack piston assembly is mainly caused by pressure differences. Another factor directly affecting the mass flow is the ring motion. As mentioned before, the ring motion and mass flow are correlated.

There are three paths for the mass flow across the ring pack: through the ring gap, through the groove behind the ring, and between the cylinder liner and the ring face (ring collapse). The latter was not observed during the simulations and is believed to be due to a relatively low engine speed and relatively low in-cylinder pressure.

During the first seven cycles after the spark is turned off, the net mass flow into the ring pack continuously decreases. By the fourth cycle the mass flow approaches steady state and for the rest of the cycles does not differ much. Figure 20 shows the mass flow from the combustion chamber for each of seven cycles at different engine speeds. It is worth noticing that the mass flow of the first cycle at 1500 rpm is almost 150 percent larger than the mass flow of the seventh cycle. However, at 3500 rpm the mass flow of the first cycle is only 80 percent larger than the mass flow at steady state.

The total back flow is a summation of two components: back flow through the groove behind the ring and back flow through the ring gap. The total cycle-based back flow and its components for seven cycle, is shown in Figure 21. Over seven cycles, the total back flow slightly decreases as the engine speed increases. However, the back flow through the groove increases but is compensated by a substantial decrease of the back flow through the ring gap. Again, it is worth noticing that the back flow through the groove due to the ring fluctuation increases with the engine speed.

The largest mass flow rate occurs at the crank angle corresponding to TDC. There are several explanations for it. The pressure in the cylinder is the highest when the piston is at TDC. The pressure pushes gas through the ring gap into the ring pack. In addition, the piston decelerates as it approaches TDC; inertia moves the ring out of the bottom of the groove, opening a passage for the gas to go from the combustion chamber into the ring pack. As the piston moves down, the in-cylinder pressure pushes the ring back to the bottom of the groove; and the flow from the volume in the groove behind the ring goes back to the combustion chamber. The plots in Figure 22 and Figure 23 show the mass flow rate through the ring groove for 1500 and 3500 rpm for the first one and a half cycles. This interval corresponds to the most rapid transients. In these plots, the notation *ring top* corresponds to the flow rate from the volume in the groove behind the ring past the top of the ring, and the notation *ring bot* corresponds to the flow past the bottom of the ring.

The plots for both engine speeds have similar features. The top ring lifts from its seat at the bottom of its groove at the same crank angle for both speeds but remains for a longer crank angle interval at the top of the groove at 3500 rpm. This, and the earlier mentioned differences in the motion of the second ring at 3500 rpm, allows a smaller net flow through the ring pack at 3500 rpm for the first seven cycles. As seen in Figure 20, the engine speed has a strong influence on the mass flow for the first seven cycles after deactivation.

Oil Film Thickness

Oil film thickness is influenced by the ring pack geometry, the piston velocity, and the inter-ring pressures as well as the in-cylinder pressure. The oil film thickness plots for seven cycles and for the first one and a half cycles at 1500 and 3500 rpm are shown in Figure 24, Figure 25, Figure 26, and Figure 27 respectively.

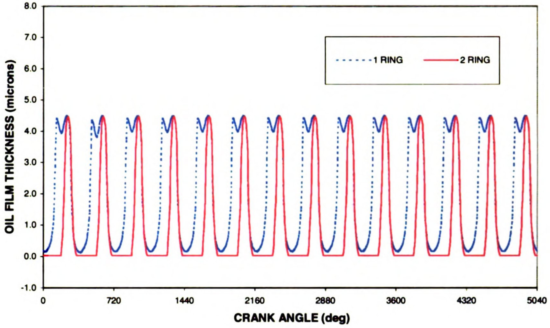

Figure 24 Oil film thickness of the cylinder deactivation transient for seven cycles at 1500 rpm

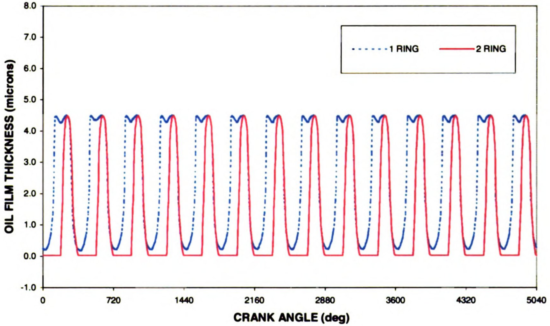

Figure 25 Oil film thickness of the cylinder deactivation transient for seven cycles at 3500 rpm

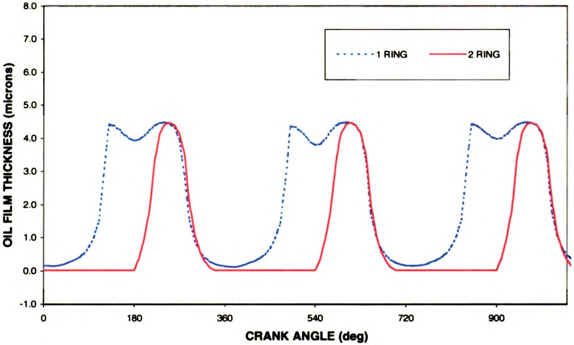

Figure 26 Oil film thickness of the cylinder deactivation transient at 1500 rpm

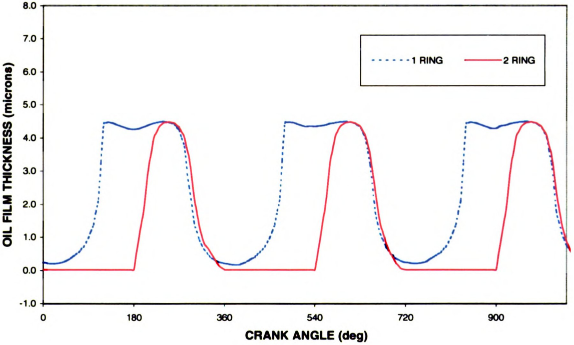

Figure 27 Oil film thickness of the cylinder deactivation transient at 3500 rpm

For the top ring the maximum oil film thickness occurs before and after the bottom dead center (BDC), near mid stroke, when the piston velocity is high, but inter-ring and in-cylinder pressures are relatively low. At BDC the film becomes thinner because the piston has low velocity. The minimum film thickness corresponds to TDC. At this point, the piston has low velocity, and the inter-ring pressure, as well as in-cylinder pressure, is high.

For the second ring, the minimum film thickness occurs at the whole downstroke because the second ring has a taper face profile and does not develop hydrodynamic lubrication. On the upstroke, the film thickness begins from the minimum at BDC, has the maximum in the middle of the stroke, and again approaches the minimum thickness at TDC.

The oil film thickness experiences only slight variations after the fuel is shut off and the valves are deactivated. The oil film thicknesses for 1500 rpm and 3500 rpm are similar except for two differences: the oil film thickness corresponding to the position of the piston at BDC is slightly different, and the minimum oil film on the first ring is about 15 percent larger for 3500 rpm.

GAS DYNAMICS ANALYSIS OF DEACTIVATED CYLINDER WITH CLOSED VALVES

The main objective of this analysis was to investigate the influence of ring pack breathing on the combustion chamber pressure. Another concern was what pressure should be kept inside the combustion chamber to attenuate oil consumption and prevent oil flow into the combustion chamber.

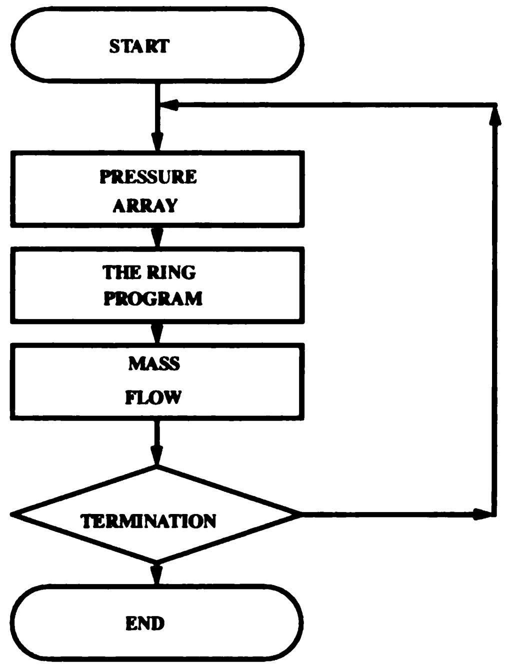

Figure 28 Flow chart of the program for calculation of the combustion chamber mass changes in the deactivated cylinder

When the valves are shut off, the piston cylinder assembly works as a compressor without an exhaust valve. The loss or gain of the air mass from the combustion chamber across the ring pack depends on the amount of air that is trapped inside the cylinder when the valves are shut off. The compression gas cycle was modeled as an isentropic process ($P\,V^{\gamma} = const$, where $\gamma = 1.4$ for air) which gives a good correlation with the experimental data measured at Ford Motor Company.

In this analysis, only the RING program was used. The standard RING program had to be modified to simulate the behavior of the cylinder with deactivated valves. The flow chart of the program is shown in Figure 28. Initially, the program generates an array of the in-cylinder pressure for every degree of crank angle based on a reference angle. A reference angle is the crank angle corresponding to the pressure inside the cylinder equal to the reference pressure. In this analysis the reference pressure was taken to be the ambient pressure. The reference angle can be considered as the angle at which the exhaust valves and the intake valves are fully closed. The main purpose of a reference angle is to model different amounts of air mass trapped inside the cylinder. A high reference angle corresponds to a large amount of mass inside the cylinder and vice versa. Evaluation of ring performance for different peak pressures (or different amounts of air mass) inside the cylinder was modeled by changing the reference angle. Based on the initial pressure array, the RING program was used to study the gas dynamics over one cycle and predict the mass flow across the ring pack from the combustion chamber and back. This flow corresponds to the mass loss or the mass gain inside the combustion chamber. Accounting for the mass change, the new combustion chamber pressure array was calculated for the next iteration. In this study the iterations were repeated 500 times which corresponds to 40 seconds of engine operation at 1500 rpm.

For each cycle the program calculated the forward flow and the back flow. During each cycle the flow moves from the combustion chamber into the ring pack and from the ring pack back into the combustion chamber. Although over a cycle the net flow is positive (from the combustion chamber into the ring pack), there can be a back flow (from the ring pack into the combustion chamber) which affects oil consumption.

For the gas dynamic analysis of the deactivated cylinder, the set of seven simulations was repeated for different engine speeds and reference angles (shut-off angles). The test points of the simulations are shown in Table 3.

Table 3 Simulation test points

500 rpm	0, 90, and 180 degrees
1500 rpm	0, 30, 60, 90, 120, 150, and 180 degrees
4000 rpm	0, 90, and 180 degrees

In-Cylinder Pressure and Mass Flow Rates

The combustion chamber loses or gains air mass over the cycle depending on the reference angle chosen. For the zero reference angle, the in-cylinder pressure at TDC is equal to the ambient pressure. At BDC there is a vacuum inside the combustion chamber. During the cycles, both the peak pressures at TDC and BDC increase due to the mass flow from the crank case to the combustion chamber. However, the total peak pressure increase over 500 cycles is less than seven percent. The lower engine speed gives a higher peak pressure increase due to a longer time span of 500 cycles at 500 rpm compared to 1500 rpm. The plots for 1500 rpm, zero reference angle are shown in Figure 29.

The 90 degree reference angle corresponds to the ambient pressure inside the cylinder at a 90 degree crank angle. The cylinder pressure is above or below the ambient pressure depending on whether the piston is at TDC or BDC. This corresponds to the mass flow from the combustion chamber on the upstroke and the mass flow to the combustion chamber on the downstroke. Overall, the pressure inside the combustion chamber decreases, but the total peak pressure decrease at TDC over 500 cycles is less than 1.5 percent.

For the 180 degree reference angle, the in-cylinder pressure at BDC is equal to the ambient pressure. The combustion chamber is highly pressurized at TDC. During the cycles the pressure inside the combustion chamber decreases. The total pressure decrease

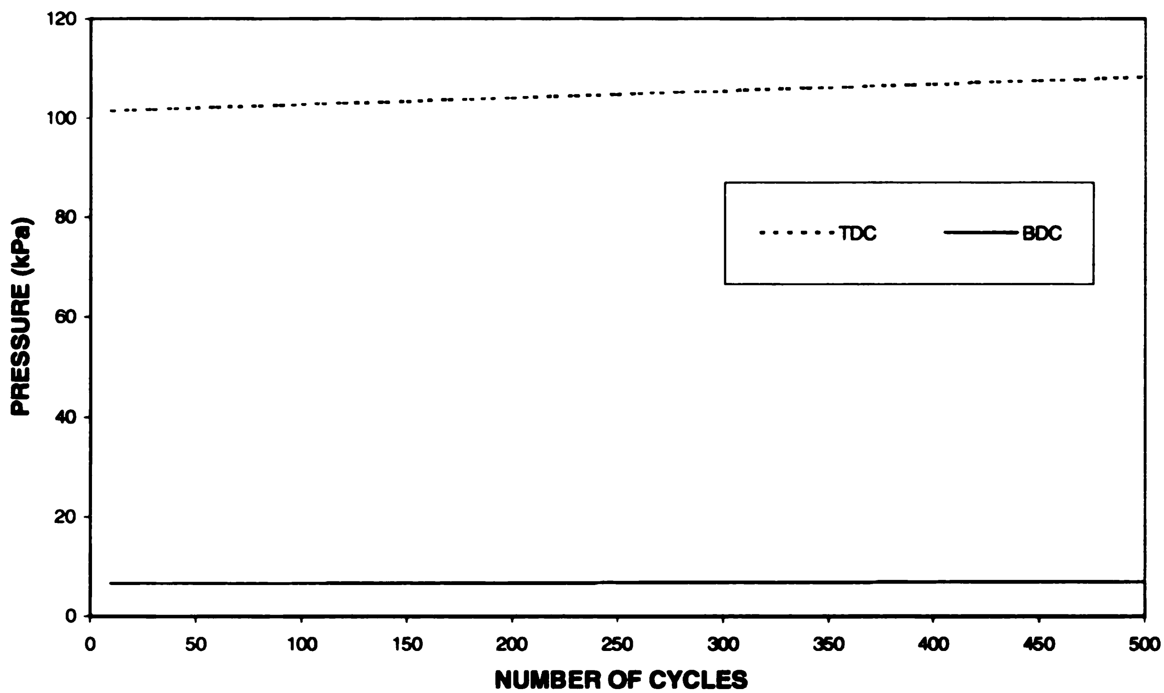

Figure 29 Top and Bottom dead center peak pressure vs. number of cycles for 0 reference angle, 1500 rpm

at TDC over 500 cycles is less than 1.5 percent. The plots for 1500 rpm and 180 degree reference angle are shown in Figure 30.

In general, all the processes of gaining or losing the air mass inside the cylinder have to converge to the steady state process in which the net mass flow is zero. Figure 31 shows a plot of reference angle (mass inside the cylinder) vs. mass flow. At 1500 rpm, the reference angle of 53 degrees corresponds to this steady state process.

The duration of the slow transient depends on the initial amount of air mass inside the cylinder. The slow transient process at 1500 rpm converges to zero net flow at the 53 degree reference angle (Figure 31). Any slow transient process can be seen as a point moving along the curve from its initial reference angle towards the zero net flow reference

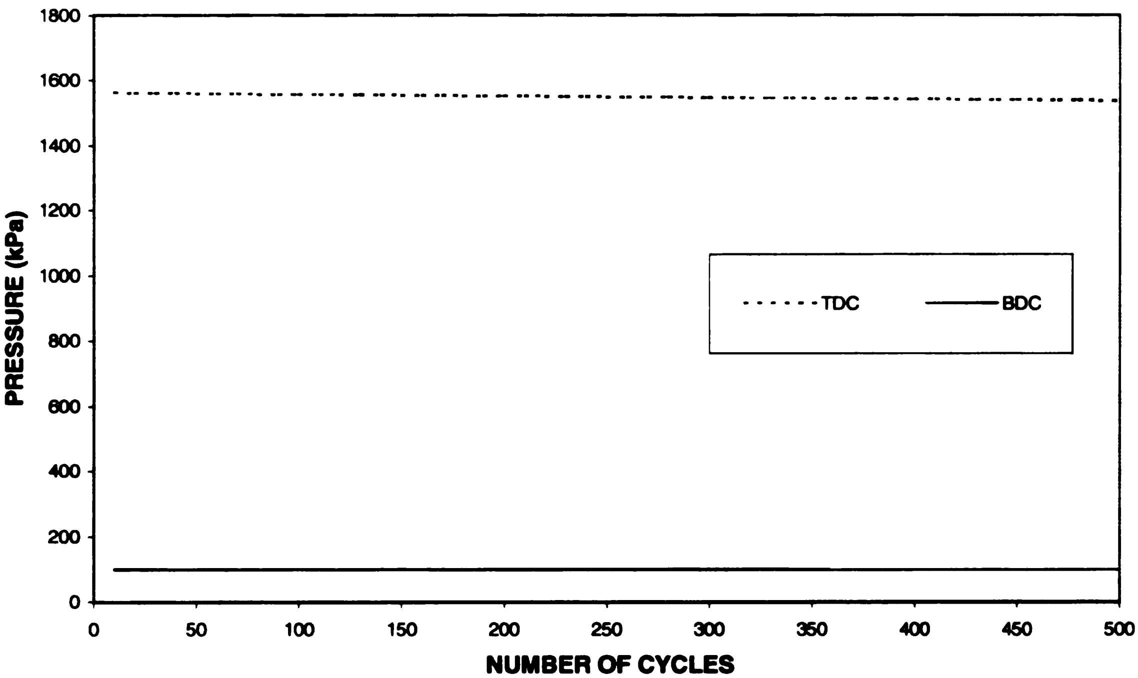

Figure 30 Top and Bottom dead center peak pressure vs. number of cycles for 180 reference angle 1500 rpm

angle. The initial 180 degree reference angle corresponds to the longest transient process which may be as long as several thousand cycles.

QUALITATIVE ANALYSIS OF OIL CONSUMPTION

The causes of oil consumption can be systematized into three main factors: oil consumption by oil mist, oil consumption by thrown-off liquid oil droplets, and oil consumption by oil vaporization from the cylinder liner. How these different mechanisms and the initial reference angle affect oil consumption is described in the next section.

Oil Consumption by Oil Mist

Back flow is believed to have an influence on oil consumption. The magnitude of back flow depends on the ring pack design and the in-cylinder pressure. In general, a high reference angle corresponds to high pressure inside the combustion chamber. Figure 31 shows the net flow and the back flow vs. reference angle for 1500 rpm, 500 cycles.

Assuming that all the gas inside the crankcase is highly saturated with oil mist (oil vapor), a negative net mass flow from the crank case to the combustion chamber will be proportional to the flow into the combustion chamber. All gas that enters the ring pack from the combustion chamber becomes partly oil saturated, so that back flow will carry oil mist into the combustion chamber. In Figure 31 the depicted mass flow can be divided into three regions:

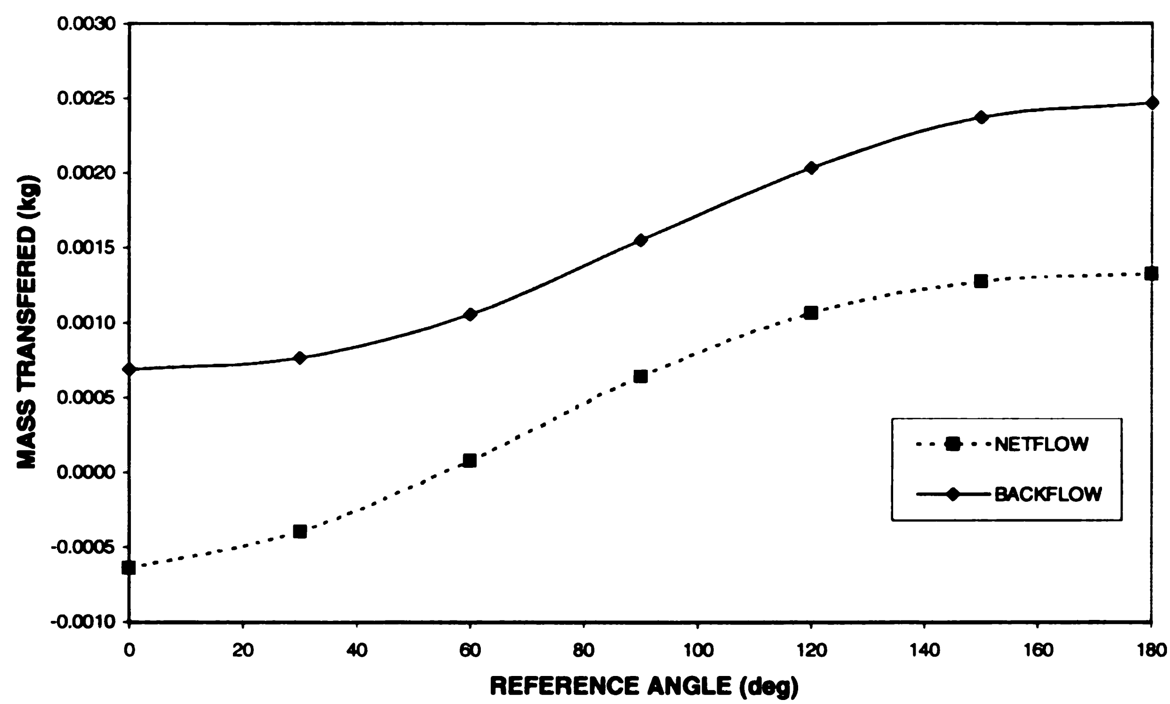

Figure 31 Mass transferred due to net flow from the combustion chamber and back flow into the combustion chamber for 500 cycles at 1500 rpm

1. 0 to 50 degree reference angle: Although the back flow is relatively small, the net flow is negative. This results in highly oil saturated gas flow from the ring pack into the combustion chamber.

2. 60 to 100 degree reference angle: This region yields a low mass back flow and no negative net flow.

3. 100 to 180 degree reference angle: The high positive net flow is compensated by a high back flow which results in oil saturated gas flow across the ring pack into the combustion chamber.

Oil Consumption by Thrown-off Liquid Oil Droplets

At TDC, oil droplets on top of the piston can be thrown off into the combustion chamber due to high deceleration. A significantly high mass flow from the combustion chamber into the ring pack restrains oil from moving into the combustion chamber. Again, in Figure 31, the depicted mass flow can be divided into three regions:

1. 0 to 50 degree reference angle: The negative mass net flow from the crank case into the combustion chamber is likely to increase the throwing off of oil droplets.

2. 60 to 100 degree reference angle: A positive mass net flow and a moderate mass back flow will reduce the process of throwing off oil droplets.

3. 100 to 180 degree reference angle: A significant positive mass net flow into the crank case and a high mass back flow into the combustion chamber will balance each other on a level of a moderate process.

Oil Consumption by Vaporized Oil From The Cylinder Liner

In a regular engine during the power stroke, the cylinder liner is exposed to the high temperature combustion chamber gases and a large heat flux. Subsequently, this can cause evaporation of the oil film left on the cylinder liner. Surface roughness and scraper face ring performance will influence the oil film thickness that remains on the liner as the piston moves down. In the deactivated cylinder, the combustion gases remain trapped inside the cylinder which can cause significant oil evaporation.

Chapter 4 SIMULATION ANALYSIS OF INTER-RING GAS PRESSURE AND RING DYNAMICS AND THEIR INFLUENCE ON BLOW-BY

MOTIVATION

In the modern world, car design is driven by two technical goals: efficiency improvement and emissions reduction. Ring pack design, as a part of the overall engine design, has a major influence on both the engine efficiency and emissions. This chapter presents the results of numerical simulations of ring pack performance for a wide range of engine operating conditions. In this analysis the ring pack simulation was used in combination with an engine thermodynamic model, the Ford Motor Company General Engine Simulation (GESIM). GESIM provided the transient boundary conditions needed for the evaluation of ring pack behavior over a wide operating range.

MODELING APPROACH

In this study, the Ring Program [16, 17, and 10] was used in combination with GESIM [30, 8, 23, 55, and 72]. The Ring Program is a part of the Cylinder kit Analysis System for Engines (CASE). The Ring Program is a model used to predict groove and inter-ring gas pressures in a piston ring pack for reciprocating gasoline and diesel engines. It also computes the oil film thickness between the rings and a distorted bore and oil volume transport past the rings for fully flooded or oil starved conditions. The oil film thickness between the piston skirt and cylinder bore is also calculated using the CASE system. Finally, friction forces, developed between the rings and bore and between the skirt and bore, are calculated. The program requires the description of the engine design parameters, engine geometry, and combustion chamber pressure over a full engine cycle.

The GESIM program is a part of the Ford ENGine SIMulation system (ENGSIM). GESIM is a computational tool for modeling in-cylinder processes in an internal combustion engine. It simulates in-cylinder flow, heat transfer, and thermodynamics during the engine cycle for firing, as well as motoring conditions. The program accounts for heat transfer losses from the combustion chamber during intake, compression, expansion, and from both burned and unburned gases during combustion.

For this analysis, GESIM was used to generate in-cylinder pressure for each operating condition point from 1000 to 5000 rpm with 500 rpm increments and from 0 inches (0 mm) to 22 inches (558.8 mm) of manifold vacuum with 2 inch (50.8 mm) increments. The engine description and the generated data with the appropriate unit and convention changes were input into the Ring Program to predict inter-ring gas pressure, ring motion and blow by. The output of the Ring Program was then post-processed to generate a global blow-by map.

GLOBAL ENGINE BLOW-BY MAP

Combustion chamber pressure, inter-ring gas pressure, and ring motion are strongly correlated. Ring motion is primarily driven by three kinds of forces: pressure forces, inertia forces, and friction forces. Inertia forces depend on primary piston dynamics and ring mass. Piston dynamics / kinematics depend on the crank mechanism geometry and are a function of engine speed. Pressure forces depend on the pressure difference above and below the ring and the area on which the pressure is acting. The pressure difference depends on the "driving" combustion chamber pressure and the ring pack capability to seal or leak gas. One of the factors affecting ring pack sealing capability is ring motion. Friction forces depend on the ring pack design and the pressure behind the ring. The ring pack can be considered as a complicated system of interrelated components. Due to the interrelations of the components and complexity of the whole system, it is very important to understand how these interdependencies affect the ring pack performance over a wide range of operating conditions.

Over the range of operating conditions, the relative magnitudes of pressure and inertia forces change. At high engine speed and low load, inertia forces dominate pressure forces in the ring dynamics. However, at low engine speed and high load, pressure forces are expected to dominate the inertia forces. An interesting question may arise: what happens between these extreme points and how does the transition between pressure forces dominating and inertia forces dominating occur? Another interesting question may be asked: how do the engine design parameters affect this force balance and transition?

A reciprocating internal combustion engine is not a steady state device. All of the processes repeat in a cycle (for a four stroke engine, one cycle is 720 degrees of crank angle). Thus, ring pack parameters must be considered as time and space dependent. This means that for each set of operating conditions, the engine parameter output such as in-cylinder pressure or temperature forms a two-dimensional map. Similarly, the operating conditions themselves are a two-dimensional map (engine load and engine speed). That is why there is a need for a scalar parameter that can represent the ring pack performance for each set of operating conditions. One of these parameters is blow-by.

5.4L V8 Measured Blow-by

Figure 32 shows the experimentally measured blow-by map of a production 5.4L V8 engine for a wide range of operating conditions (engine speed [rpm] and engine load [reciprocal to manifold vacuum]). At most of the operating conditions (high load, low rpm; low load, low rpm; and high load high rpm) the blow-by forms an inclined surface. The blow-by decreases as operating conditions move from high load (zero vacuum) to low load (22 inches of vacuum); and even smaller reduction in blow-by is seen as one moves from low speed to high speed. However, at low load high rpm, a dramatic increase in blow-by is seen (consider an imaginary line between 10 inches 5000 rpm and 22 inches 3500 rpm). In this region, the experimental results show that the ring pack does not seal and blow-by increases dramatically. This is shown in the next section and the reasons for this are discussed. This region correlating to extreme operating conditions is rarely seen in a vehicle. The blow-by map shown in Figure 32 is typical for most engines. Attention to the low load and high engine speed is primarily to correlate the model to a wider range of operating conditions than typically encountered in a vehicle.

Blow-by Simulation Results

The simulation of blow-by for the same 5.4L V8 engine in the same range of operating conditions was created using the computational procedure described above.The results are shown in Figure 33 which shows a very similar trend to the measured blow-by map. The simulation results show a gradual decrease in blow-by for high to low load and

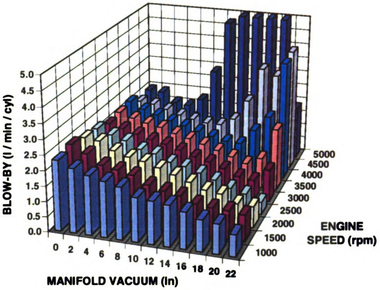

Figure 32 Measured blow-by map from the cylinder for the 5.4L V8 engine

low rpm and high load and high rpm. However, at high rpm and low load, the blow-by dramatically increases. Figure 45 and Figure 46 show the combustion and inter-ring gas pressure for 2 inches of vacuum 2000 rpm and 18 inches of vacuum 4500 rpm, respectively. The first plot corresponds to a point of a gradual decrease of blow-by. In this plot the second land pressure achieves only about 10 percent of the peak combustion pressure. It is worth noticing that the second land pressure gradient changes at 350 crank degrees. This gradient change is due to second ring motion. Figure 46 corresponds to the point at the blow-by spike. The second land pressure achieves about 90 percent of the peak combustion pressure. Tian et al. [75] described a similar phenomena for a 2.0L I4 engine. At this operating point, the ring pack loses its ability to seal the combustion chamber. This causes the spikes in the blow-by map.

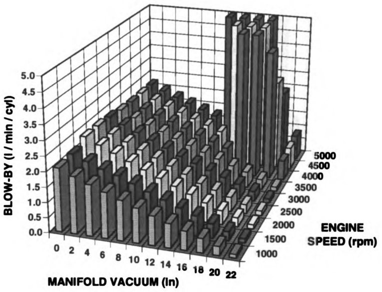

Figure 33 Predicted blow-by map from the cylinder for the 5.4L V8 engine

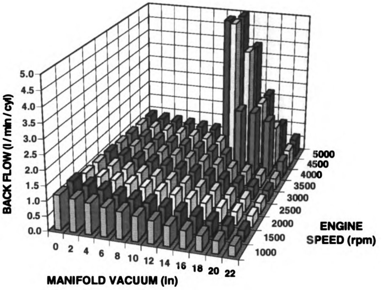

Figure 34 Predicted back flow map into the cylinder for the 5.4L V8 engine

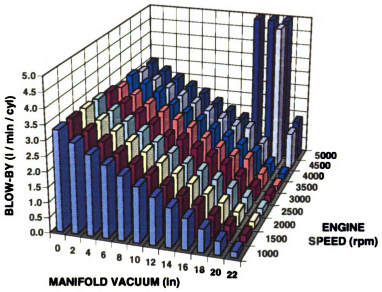

Figure 35 Predicted blow-by map from the cylinder for the 4.6L V8 engine

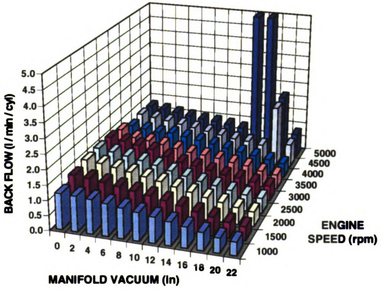

Figure 36 Predicted back flow map into the cylinder for the 4.6L V8 engine

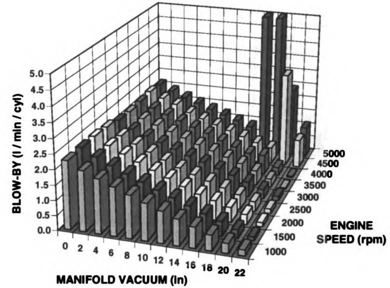

Figure 37 Predicted blow-by map from the cylinder for the 2.3L I4 engine

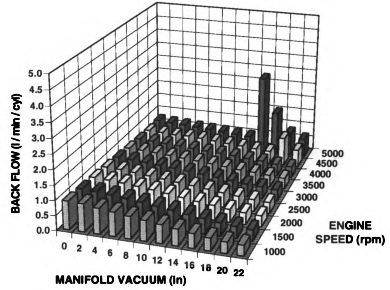

Figure 38 Predicted back flow map into the cylinder for the 2.3L I4 engine

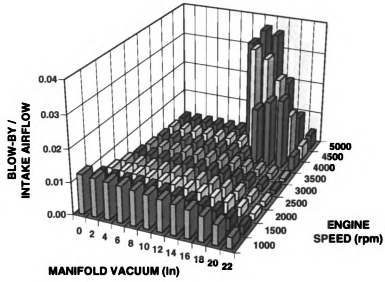

Figure 39 Predicted blow-by map from the cylinder normalized over intake airflow for the 5.4L V8 engine

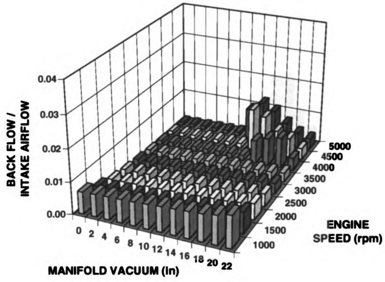

Figure 40 Predicted back flow map into the cylinder normalized over intake airflow for the 5.4L V8 engine

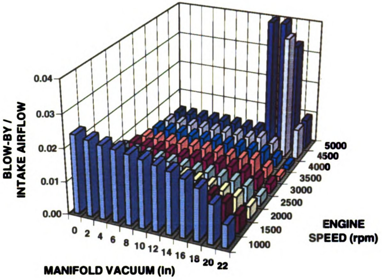

Figure 41 Predicted blow-by map from the cylinder normalized over intake airflow for the 4.6L V8 engine

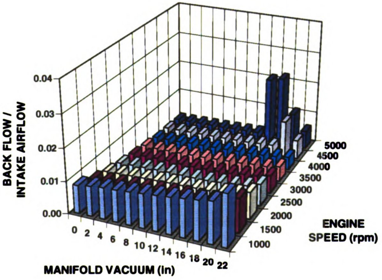

Figure 42 Predicted back flow map into the cylinder normalized over intake airflow for the 4.6L V8 engine

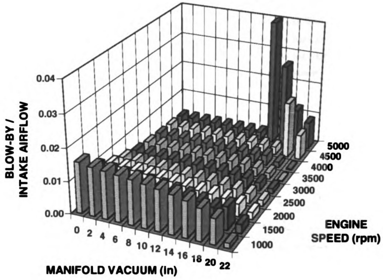

Figure 43 Predicted blow-by map from the cylinder normalized over intake airflow for the 2.3L I4 engine

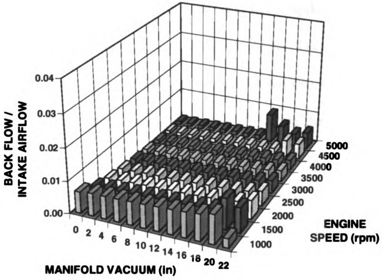

Figure 44 Predicted back flow map into the cylinder normalized over intake airflow for the 2.3L I4 engine

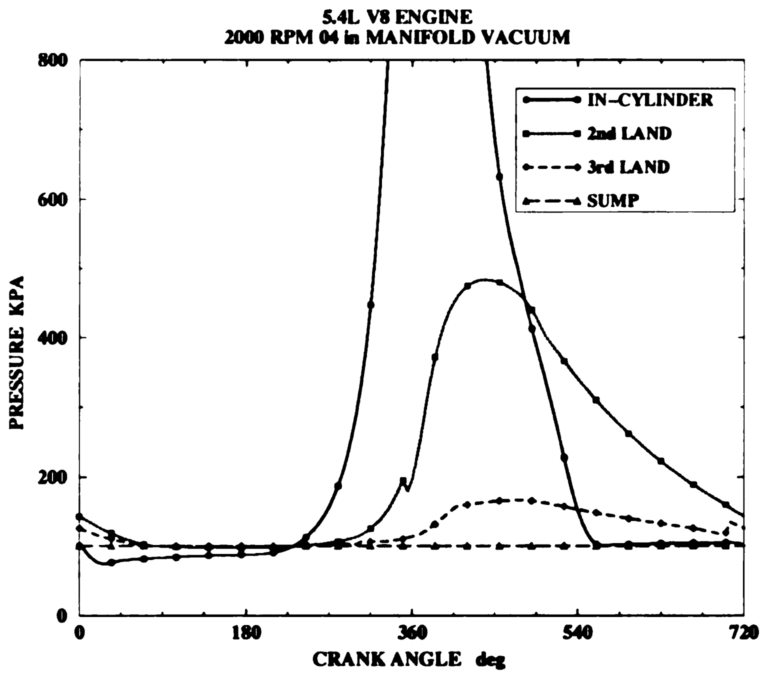

Figure 45 Combustion and inter-ring pressure at 04" manifold vacuum 2000 rpm for the 5.4L V8 engine

The spikes in the blow-by map are correlated to the spikes in the back flow map. Figure 34 shows the back flow map for the 5.4L V8 engine. The blow-by corresponds to the total net flow from the combustion chamber through the ring pack into the crank case during the complete engine cycle. In some parts of the cycle the gas flows into the ring pack (forth flow) and in other parts of the cycle the gas can flow from the ring pack into the combustion chamber (back flow). Usually, the back flow occurs at the exhaust and intake strokes when the pressure inside the combustion chamber is low; but the pressure in the ring pack chambers, especially at the second land, is high. Excessive back flow can cause an increase in hydrocarbon emissions and oil consumption.

In order to eliminate the ramp with manifold vacuum in Figure 33, Figure 34, Figure 35, Figure 36, Figure 37, and Figure 38, the blow-by maps were normalized with

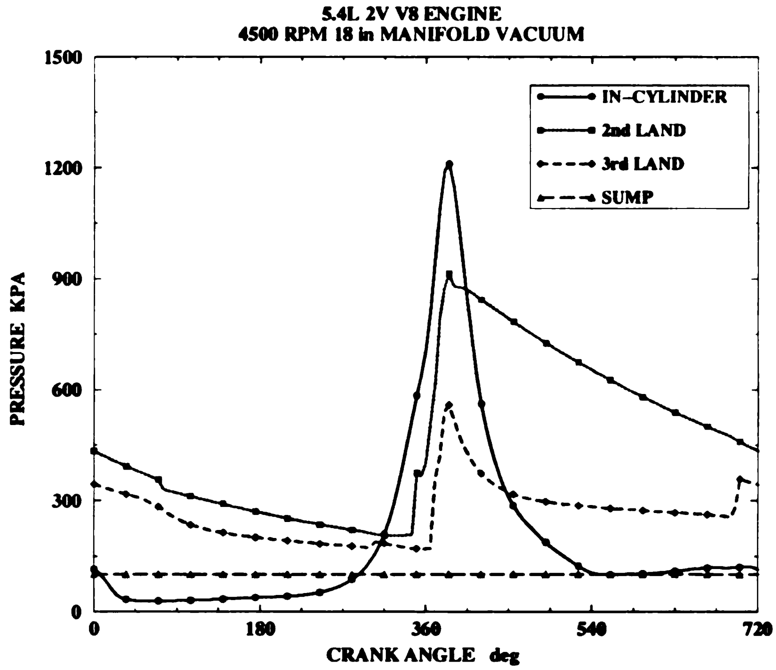

Figure 46 Combustion and inter-ring pressure at 22" manifold vacuum 4500 rpm for the 5.4L V8 engine

the intake manifold airflow into the cylinder over a cycle. The non-dimensional blow-by and back flow maps for the three engines are shown in Figure 39, Figure 40, Figure 41, Figure 42, Figure 43, and Figure 44. The normalized blow-by maps (Figure 39, Figure 41, and Figure 43) show dependence on engine speed at low rpm. However, at high engine speed, above 3000 rpm, the blow-by does not change with speed. At low engine load and high rpm, the normalized blow-by maps show spikes. The normalized back flow maps in Figure 40, Figure 42, and Figure 44 show an increase with manifold vacuum and a decrease with engine speed.

The spikes in the blow-by in Figure 33 and Figure 34 correspond to ring collapse. As mentioned before, ring dynamics are governed by the balance between pressure and inertia forces. For most operating conditions, at the end of the compression stroke and for most of the power stroke, the top ring stays at the bottom of the groove. This happens because the pressure forces exceed the inertia forces. This is shown in Figure 9 on page 25. At low engine load and high engine speed, the inertia forces may dominate the pressure forces and the top ring stays at the top of the groove during combustion. If the pressure above the ring is high enough and the pressure behind the ring is low enough, the ring can lose contact with the cylinder bore and opens a large area for gas flow. For ring collapse to occur, the following conditions of inertia forces, pressure above the ring, pressure behind the ring, and ring tension must be fulfilled.

$$\left(\frac{p_1 + p_3}{2}\right) > p_{RT} + p_2 \tag{41}$$

$$A_3 \cdot p_3 + m_r \cdot \ddot{x} > A_1 \cdot p_1 \tag{42}$$

Rearranging Eq. (41) and Eq. (42) yields the following.

$$m_r \cdot \ddot{x} > 2p_{RT} \cdot A_1 + p_3 \cdot (A_1 - A_3) \tag{43}$$

where $\ddot{x}$ is ring acceleration.

$$\ddot{x} = L_c \omega^2 \left(\cos(\omega t) + \frac{\cos^2(\omega t)}{\sqrt{\frac{L_r}{L_c} - \sin^2(\omega t)}} + \frac{\cos^2(\omega t) \cdot \sin^2(\omega t)}{\left(\frac{L_r}{L_c} - \sin^2(\omega t)\right)^{3/2}} - \frac{\sin^2(\omega t)}{\sqrt{\frac{L_r}{L_c} - \sin^2(\omega t)}} \right) \tag{44}$$

It can be seen that $\ddot{x}$ depends on the engine speed ω and slider - crank geometry, crank radius Lr and connecting rod length Lc. On the other hand, the area A_1 and A_3 as well as the ring mass m_r depend on the ring design and the bore diameter.

The same GESIM and RING modeling approach was applied to two more engines: a production 4.6L V8 and a production 2.3L I4. The 4.6L engine has an almost identical ring pack design to the 5.4L but a smaller stroke. The 2.3L engine has a similar ring pack design but a different bore / stroke ratio with a bigger bore and smaller stroke. Based on its displacement, the 2.3L I4 engine can be considered as a half of the 4.6L V8 engine with the same displacement per cylinder. Also, it is worth noting that the 2.3L engine has very low oil consumption. The predicted blow-by maps for the 4.6L V8 and 2.3L I4 are shown in Figure 35 and Figure 36 respectively. The blow-by maps for the 4.6L V8 and 2.3L I4 show a similar trend to the one for the 5.4L V8. The blow-by gradually decreases in the region of high to low rpm and high load and low rpm and low load. At high rpm low load, the maps show the spikes of blow-by. However, these spikes cover a smaller map area than for the 5.4L engine. Comparing the 5.4L, 4.6L, and 2.3L engines and keeping in mind the decreasing bore / stroke ratio for these engine, it can be seen that the balance between pressure and inertia forces is shifted.

The back flow maps for the 5.4L, 4.6L, and 2.3L engines shown in Figure 36, Figure 37, and Figure 38 form a surface similar to the original back flow map. The back flow maps show a correlation between spikes in total blow-by and back flow, very similar to the 5.4L engine.

TOP COMPRESSION RING ANALYSIS

It is very important to determine if the spikes in the blow-by map due to top ring collapse are a phenomena of the top ring or if the second ring has a significant influence on it. To examine this idea, the original ring pack was modified and left only with the top compression ring. Then, the same computational procedure was applied to the modified ring pack. Figure 47 and Figure 48 show the blow-by and back flow map for the modified one-ring 5.4L V8 engine. The blow-by map is very similar to the original blow-by map. Blow-by gradually decreases in the region of high rpm and high load, low rpm and high load and low rpm and low load and shows spikes at high rpm and low load. The blow-by magnitude in the region of a gradual decrease is higher than in the original map, but the difference is less than 10 percent. The blow-by magnitude increase is due to the absence of the second and oil control rings. At high rpm and low load, the map shows spikes which correspond to the spikes in the original map.

The back flow map (Figure 48) does not show spikes at high rpm and low load. This is due to the absence of the second and oil control ring. For the full ring set piston pack, a certain amount of gas gets trapped in the second and third land volumes during the power stroke and can cause excessive reverse back flow into the combustion chamber during the exhaust and intake strokes. For the one ring piston pack, the pressure below the top ring is assumed to be sump pressure and does not depend on the amount of blow-by.

The one ring blow-by simulation results for the 2.3L engine show the same trend as the full ring set engine. The blow-by map is similar to the original map (Figure 37), but the magnitude of blow-by is bigger by about 10 percent. Again, this is due to the absence

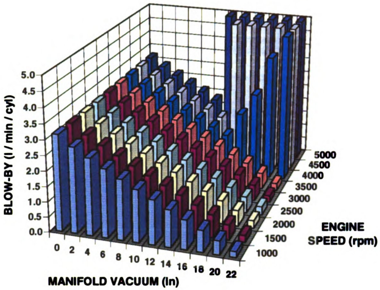

Figure 47 Predicted blow-by map from the cylinder for the 5.4L V8 engine, one ring

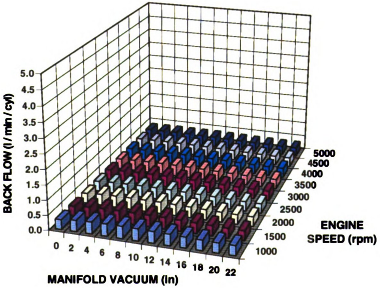

Figure 48 Predicted back flow map into the cylinder for the 5.4L V8 engine, one ring

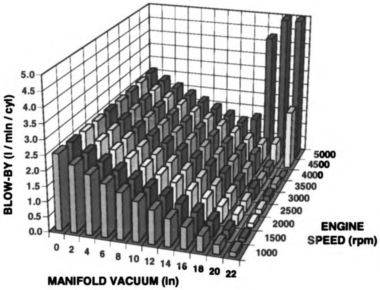

Figure 49 Predicted blow-by map from the cylinder for the 2.3L I4 engine, one ring

of the second and oil control rings. Comparing the blow-by map of the full ring set and one ring piston configurations for both the engines, it can be concluded that the ring collapse phenomena and ensuing blow-by spikes are primarily due to first ring dynamics and first ring configuration.

Since the ring collapse phenomena is primarily a local phenomena of the top ring, the top ring behavior was thoroughly examined. Figure 50 and Figure 51 show the combustion chamber pressure for the 5.4L V8 engine for a range of operating conditions, from 3000 to 5000 rpm and from 16 to 22 and 8 to 14 inches of manifold vacuum. The peak combustion pressure decreases as manifold vacuum or engine speed increase. The influence of manifold vacuum on the peak in-cylinder pressure is bigger than the influence of engine speed. Figure 52 and Figure 53 show the ring motion for 3000 to 5000 rpm 16 to 22 and 8 to 14 inches of manifold vacuum respectively for the 5.4L V8 engine with one

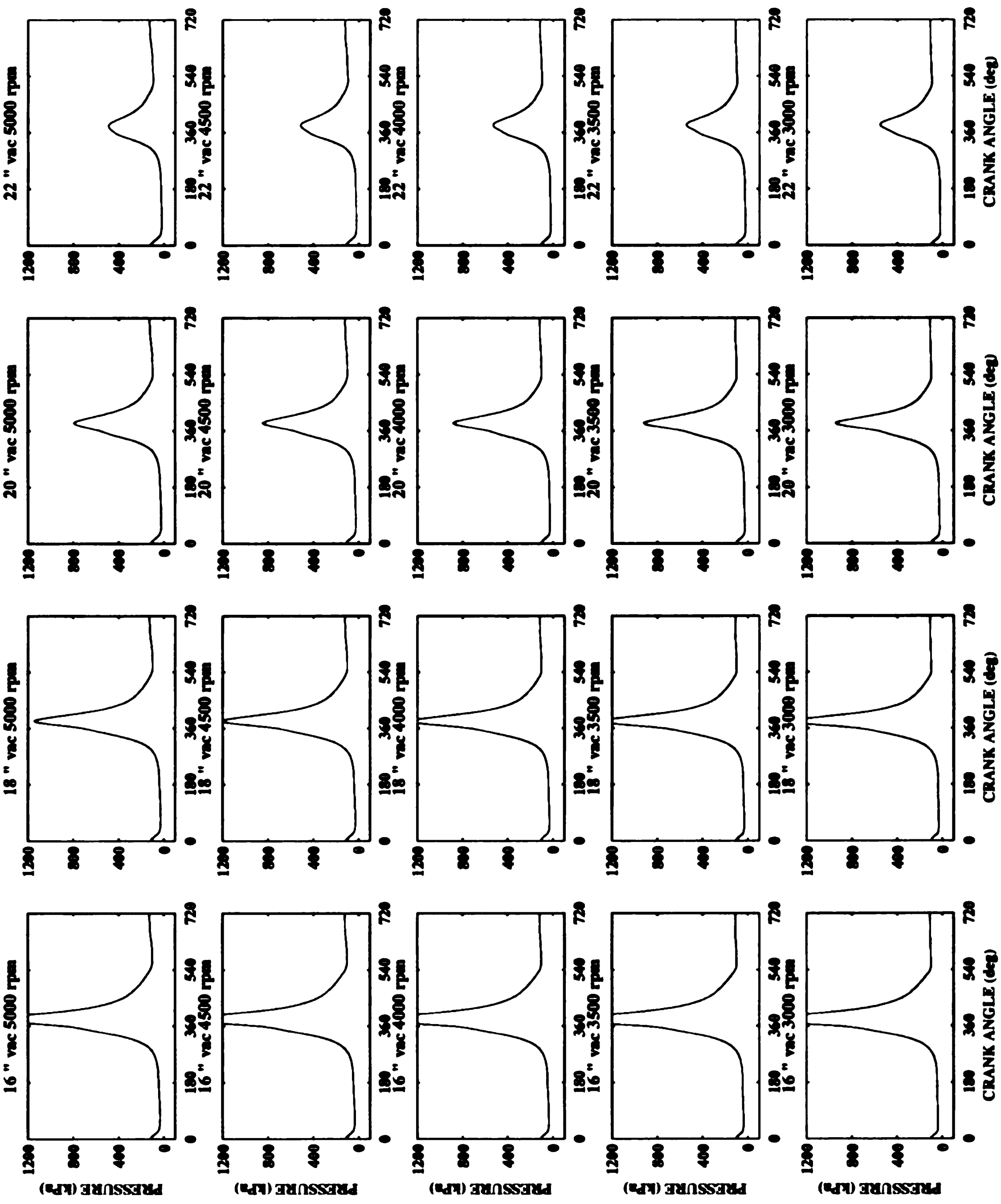

Figure 50 In-cylinder pressure traces for the 5.4L V8 engine, one ring, 16 - 22 inches of manifold vacuum, 3000 - 5000 rpm

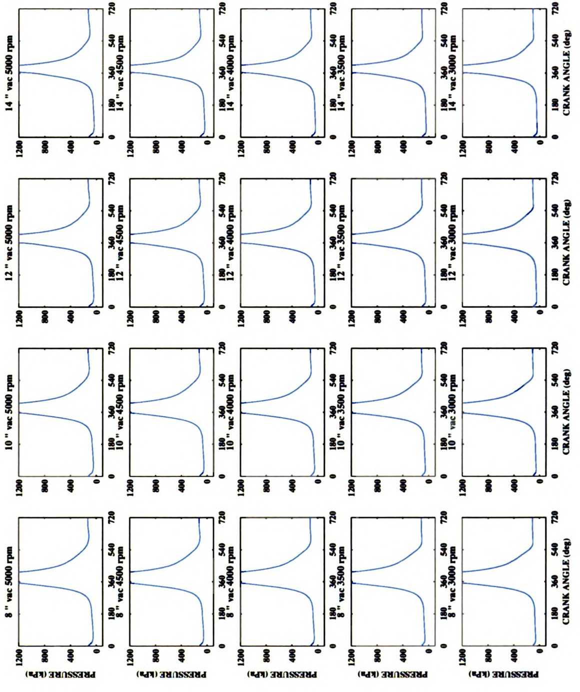

Figure 51 In-cylinder pressure traces for the 5.4L V8 engine, one ring, 08 - 14 inches of manifold vacuum, 3000 - 5000 rpm

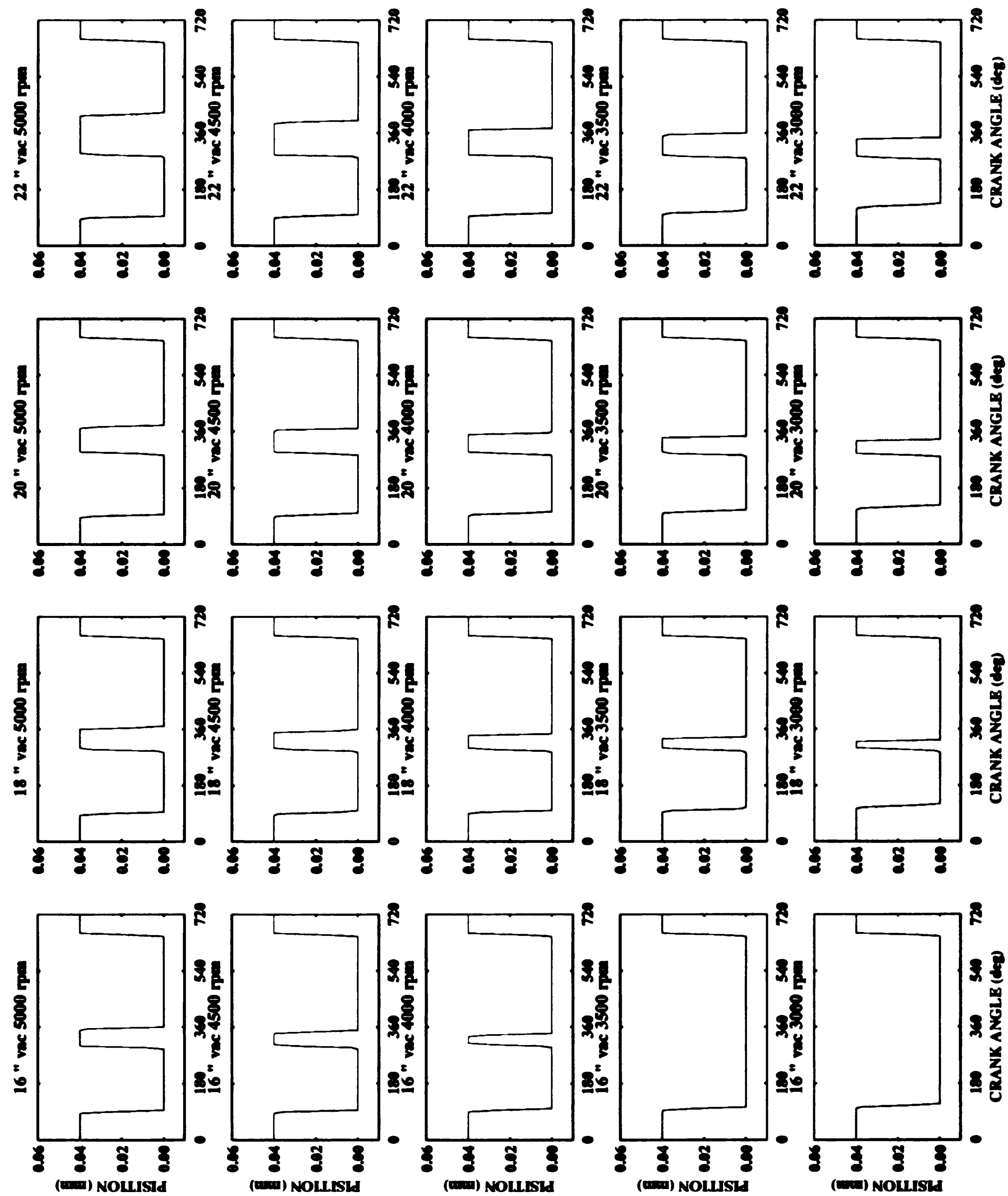

Figure 52 Top ring motion for the 5.4L V8 engine, one ring, 16 - 22 inches of manifold vacuum, 3000 - 5000 rpm

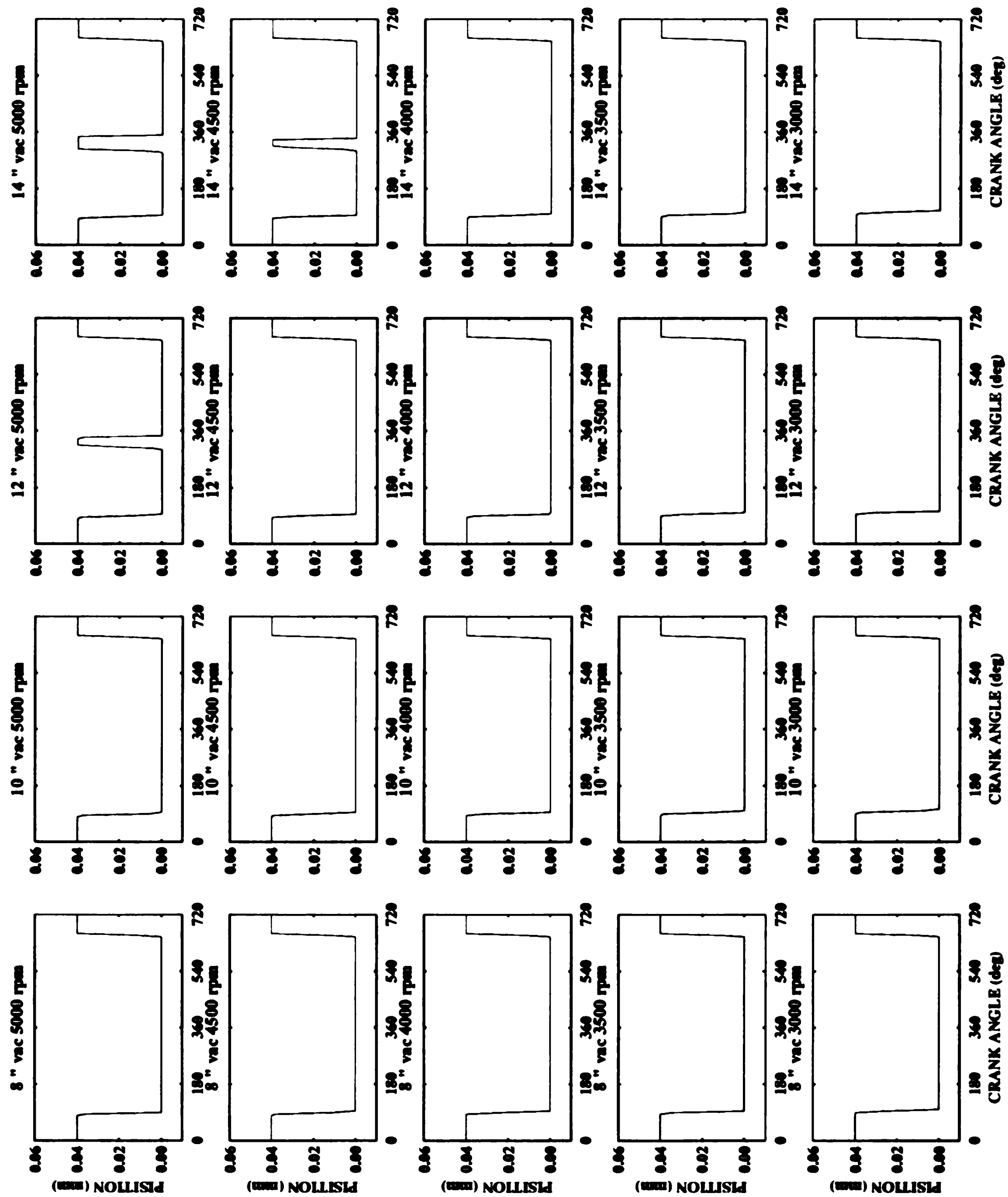

Figure 53 Top ring motion for the 5.4L V8 engine, one ring, 08 - 14 inches of manifold vacuum, 3000 - 5000 rpm

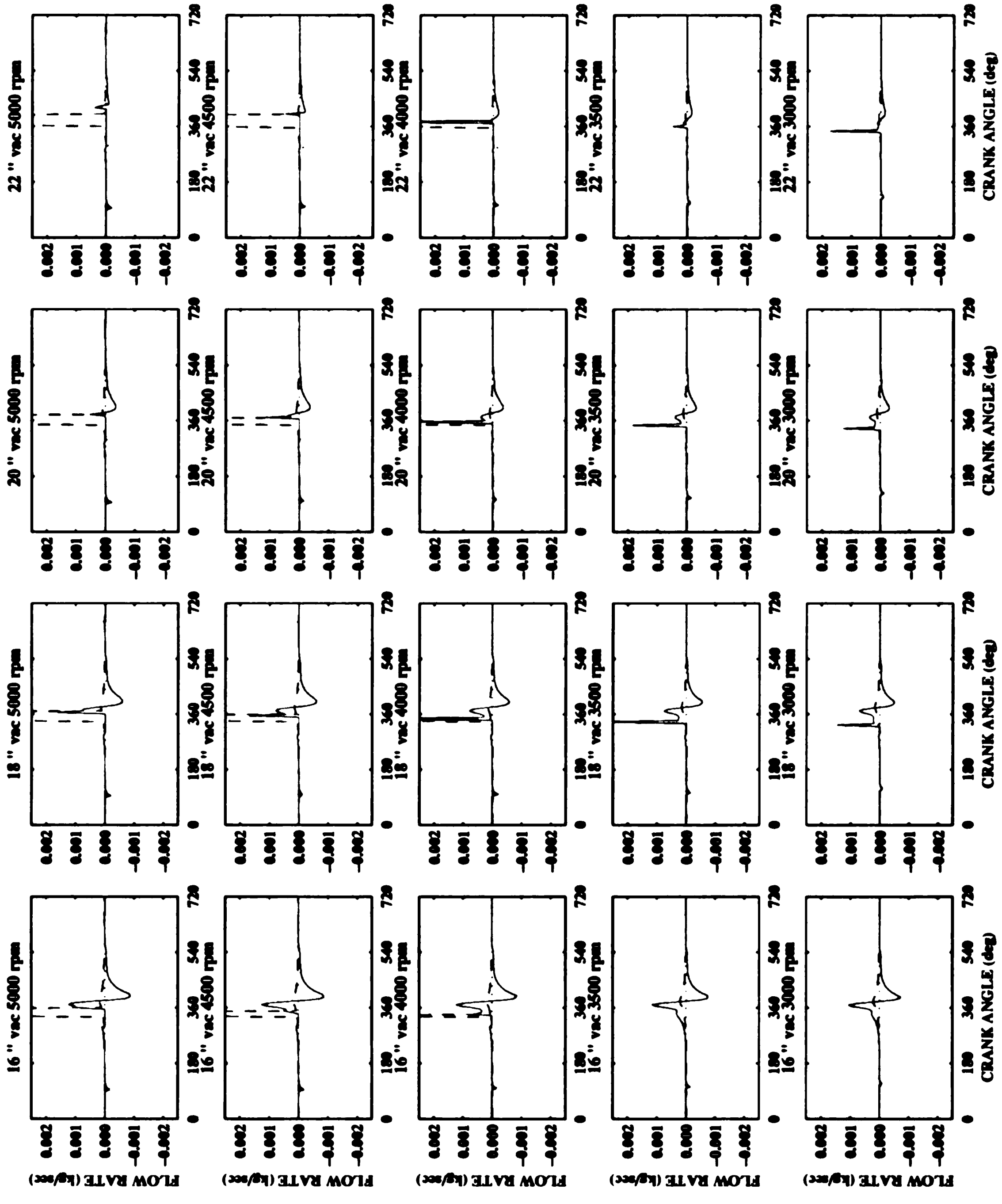

Figure 54 Mass flow rate across the top ring from the cylinder for the 5.4L V8 engine, one ring, 16 - 22 inches of manifold vacuum, 3000 - 5000 rpm

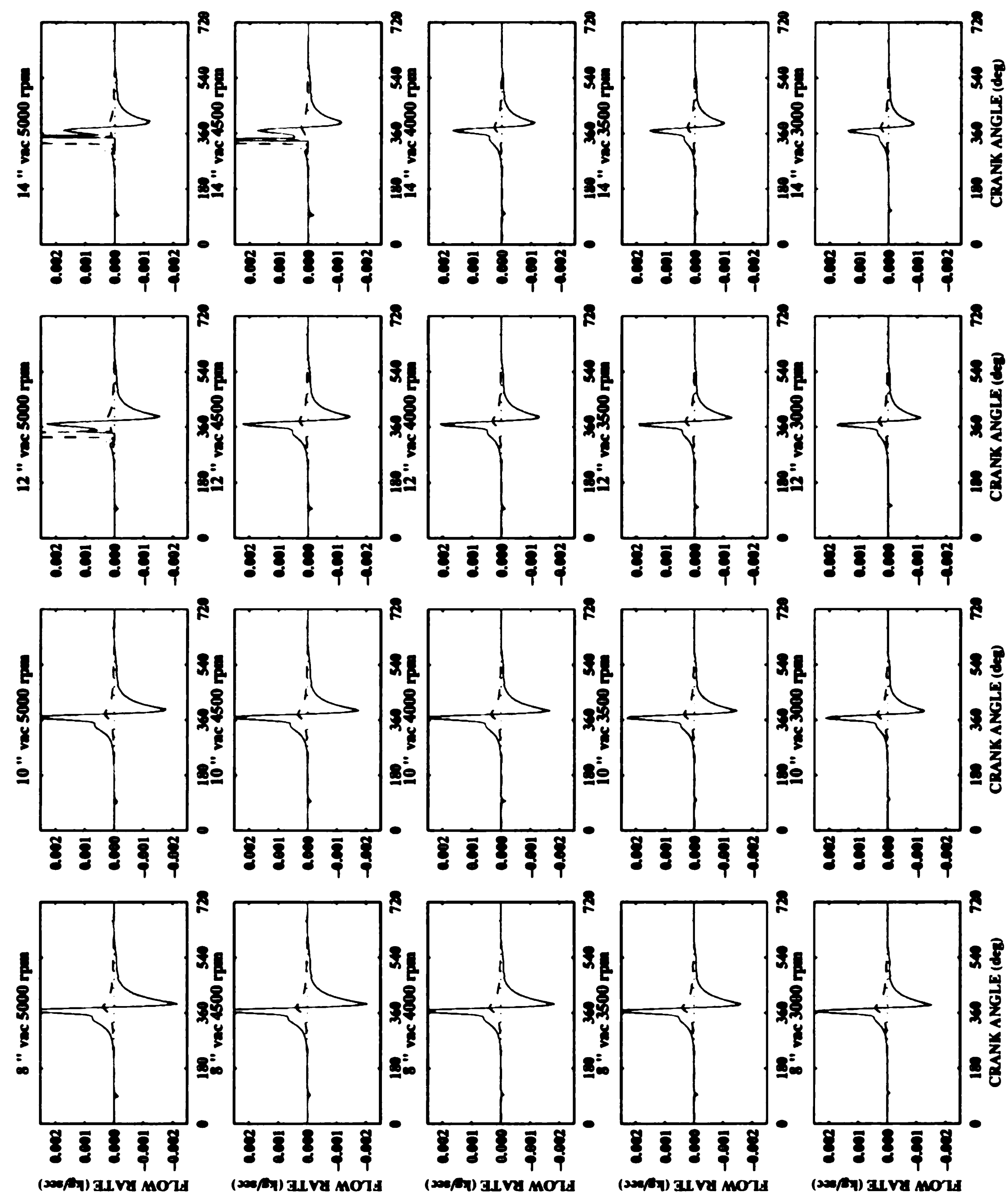

Figure 55 Mass flow rate across the top ring from the cylinder for the 5.4L V8 engine, one ring, 08 - 14 inches of manifold vacuum, 3000 - 5000 rpm

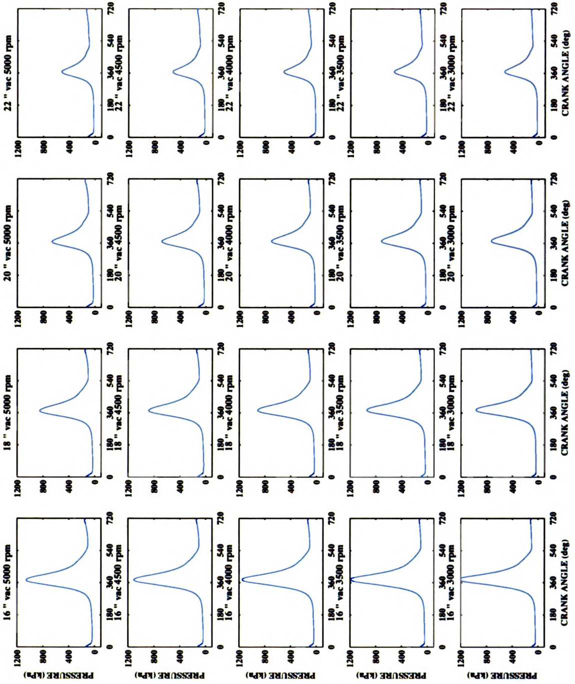

Figure 56 In-cylinder pressure traces for the 4.6L I4 engine, one ring, 16 - 22 inches of manifold vacuum, 3000 - 5000 rpm

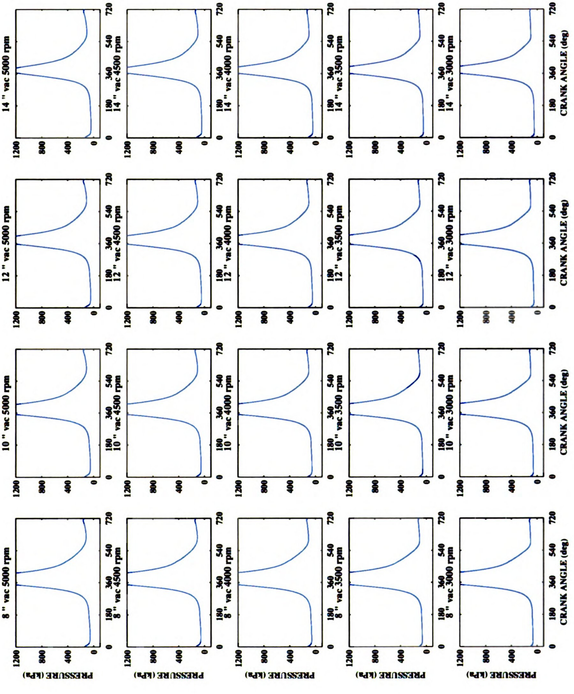

Figure 57 In-cylinder pressure traces for the 4.6L I4 engine, one ring, 08 - 14 inches of manifold vacuum, 3000 - 5000 rpm

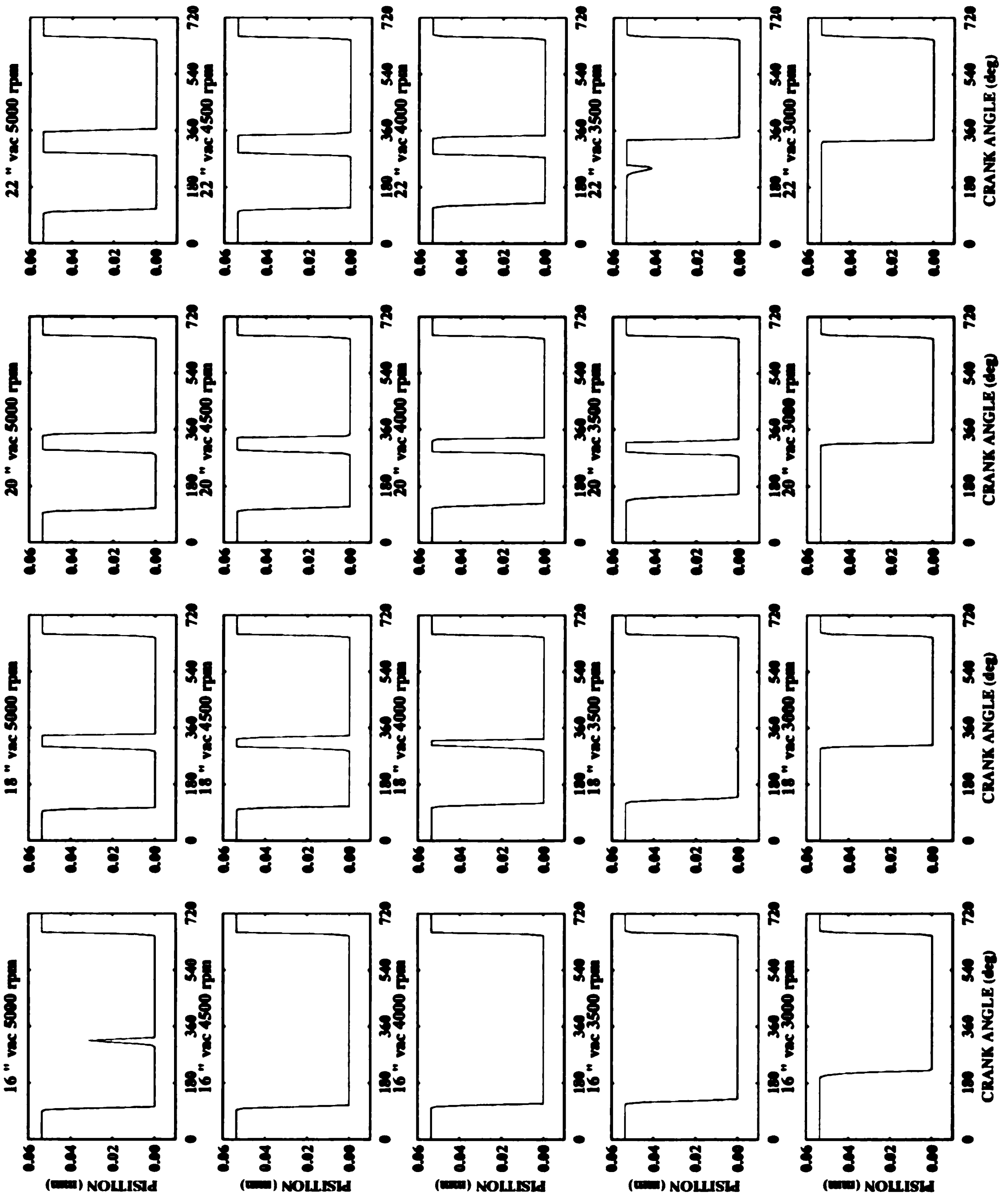

Figure 58 Top ring motion for the 4.6L I4 engine, one ring, 16 - 22 inches of manifold vacuum, 3000 - 5000 rpm

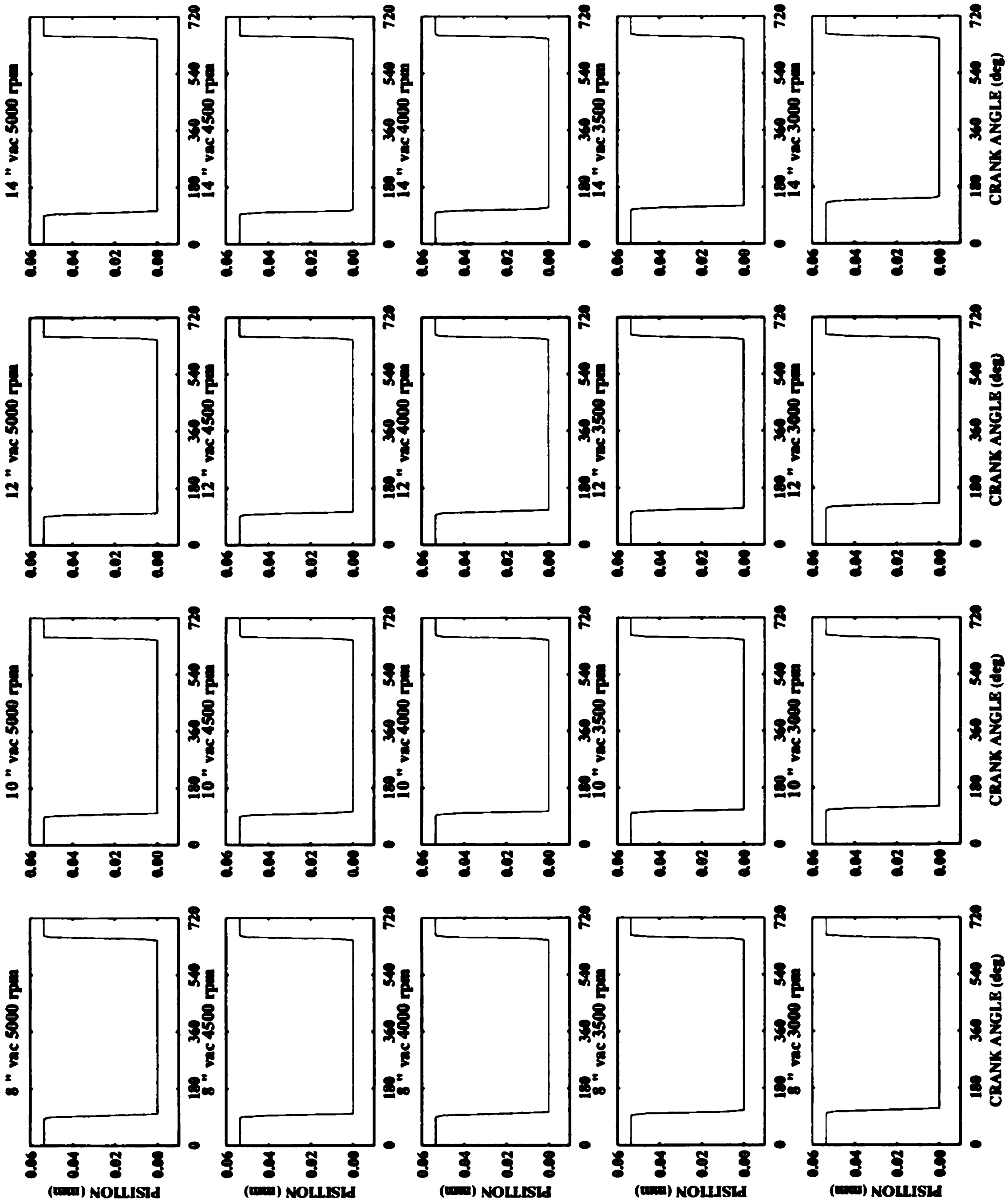

Figure 59 Top ring motion for the 4.6L I4 engine, one ring, 08 - 14 inches of manifold vacuum, 3000 - 5000 rpm

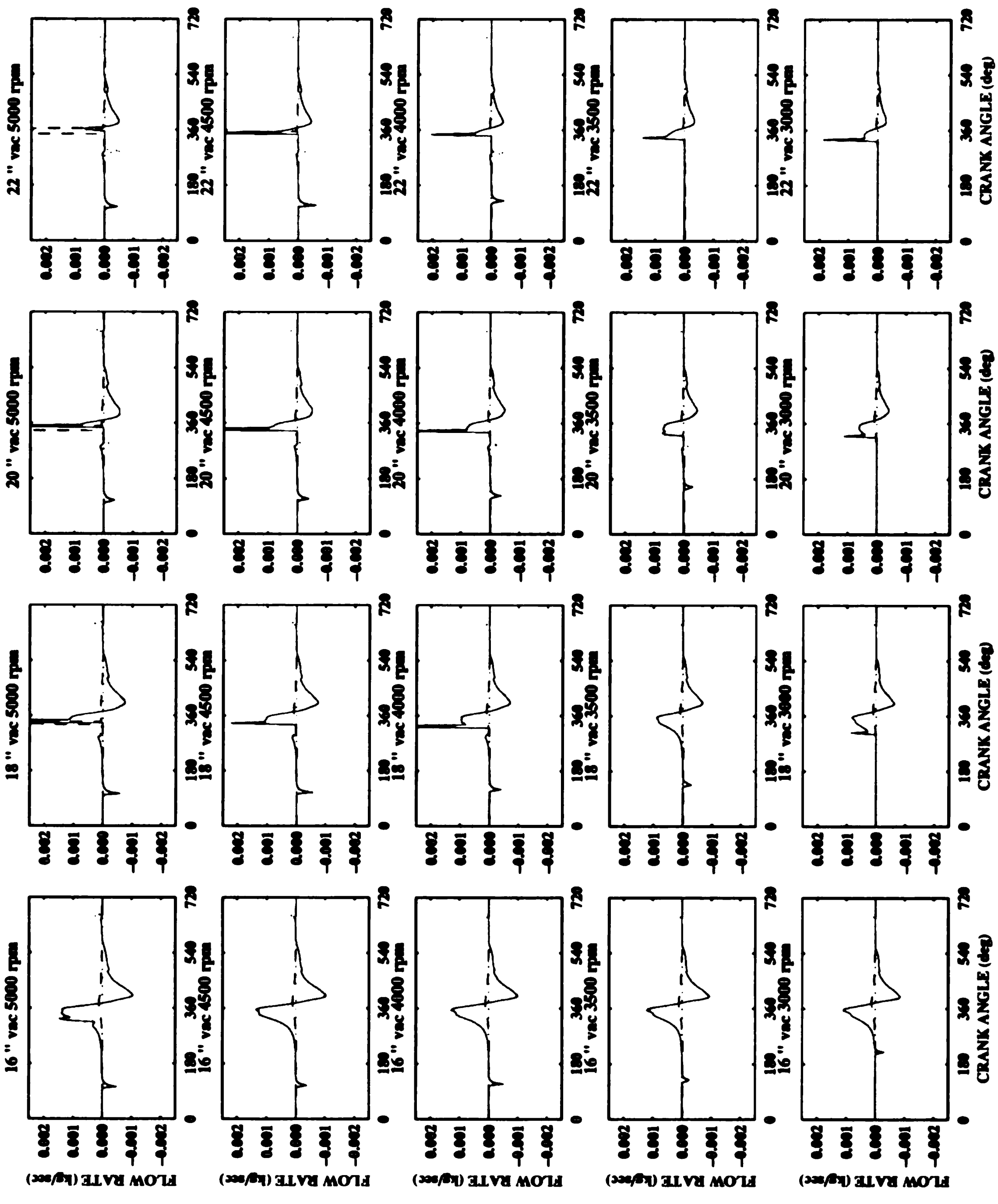

Figure 60 Mass flow rate across the top ring from the cylinder for the 4.6L I4 engine, one ring, 16 - 22 inches of manifold vacuum, 3000 - 5000 rpm

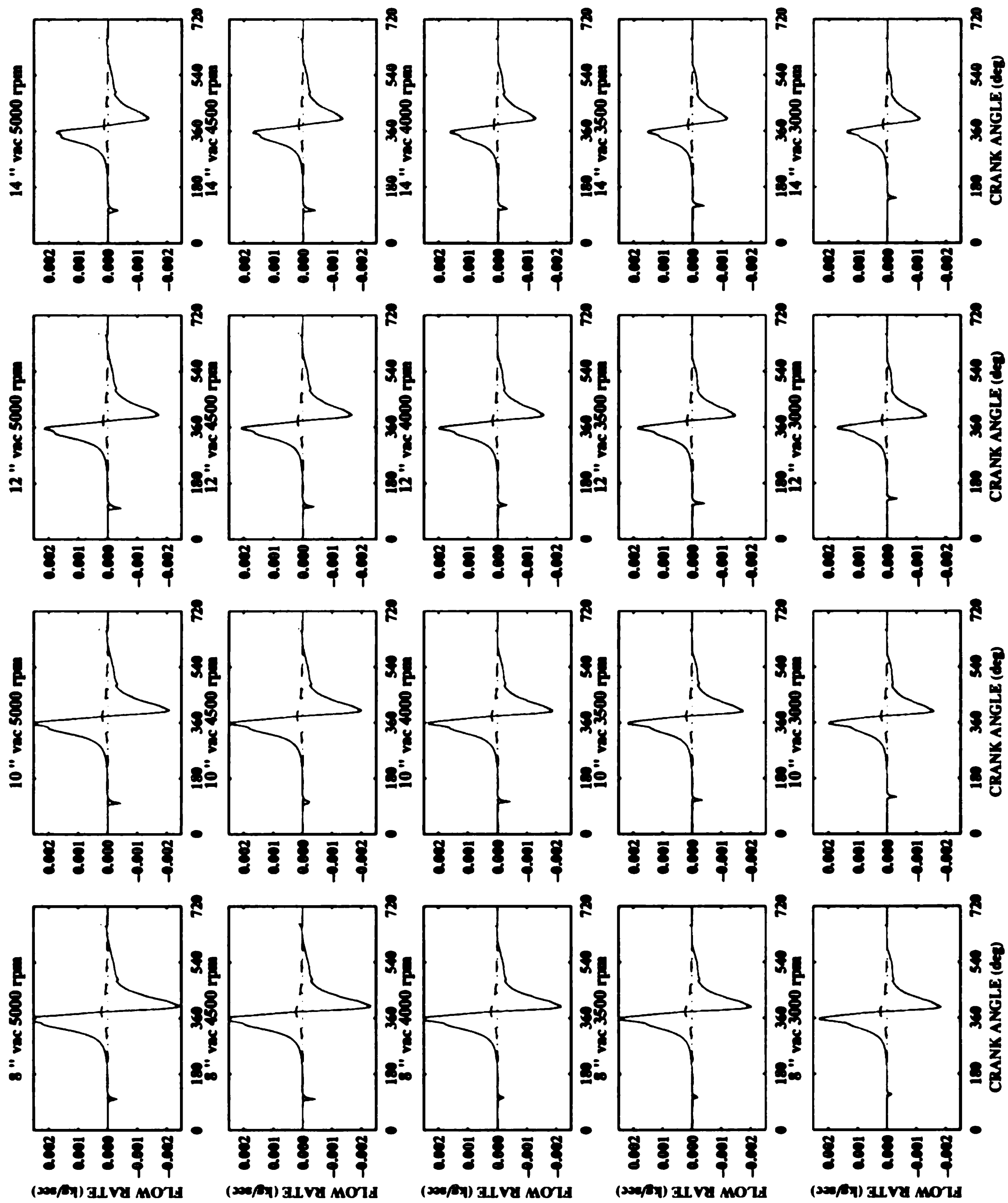

Figure 61 Mass flow rate across the top ring from the cylinder for the 4.6L I4 engine, one ring, 08 - 14 inches of manifold vacuum, 3000 - 5000 rpm

ring. Figure 54 and Figure 55 show the mass flow rates for 3000 to 5000 rpm 16 to 22 and 8 to 14 inches of manifold vacuum for the same engine configuration. Mass flow across the ring includes three components: above the ring into the groove, below the ring from the groove to the second land, and through the ring including flow through the ring end gap and due to ring collapse. Figure 56, Figure 57, Figure 58, Figure 59, Figure 60, and Figure 61 show combustion chamber pressure, ring motion, and mass flow rate, respectively, for the 2.3L I4 engine with one ring.

Ring motion has an important effect on inter-ring gas pressure, blow-by, and back flow. At moderate engine speeds and moderate loads, the top ring behaves in the following manner. At the beginning of the cycle (Top Dead Center [TDC] at the beginning of the intake stroke), it stays at the top of its groove due to the dominance of inertia forces over pressure forces. At this moment, the pressure inside the cylinder is low and the piston accelerates downward. Near the middle of the intake stroke, the ring moves to the bottom of the groove due to an increase of in-cylinder pressure and a change in the direction of the inertia forces due to piston deceleration. The ring stays at the bottom of the groove until the middle of the exhaust stroke. During this time (crank angle) interval, the in-cylinder pressure rises significantly during combustion and pressure forces exceed the inertia forces. In the middle of the exhaust stroke, the inertia force starts acting upward and the pressure inside the cylinder drops. This causes the ring to move to the top of the groove and stay there until the end of the cycle.

Changing operating conditions can change the balance between pressure and inertia forces and can lift the ring up during combustion (consider an imaginary line between points of 12 inches 5000 rpm and 18 inches 3000 rpm in the ring motion plots for the 5.4L

V8 engine with one ring [Figure 52 and Figure 53]). This is a border line of dominance between the pressure and inertia forces. Below this line, the pressure forces dominate inertia forces. Above this line, the inertia forces start dominating the pressure forces. In the extreme case, 22 inches 5000 rpm, the ring stays at the top of groove during most of the compression and exhaust strokes.

Mass flow rate depends on the area and the pressure difference (unless the flow is choked). When the in-cylinder pressure rises and the ring is at the bottom of the groove, the gas flows from the cylinder to the volume behind the ring and the pressure in this volume increases. During the exhaust stroke the pressure in the cylinder drops and gas flows from the volume behind the ring into the cylinder causing the pressure to decrease in this volume. If during the power and exhaust strokes the ring moves to the top of the groove, it opens a passage for gas to flow from the volume behind the groove to the second land. If at this moment the pressure behind the ring is relatively high, the gas flows into the volume on the second land causing blow-by.

The other paths for gas flow are through the ring end gap and due to ring collapse. The ring end gap flow is an inevitable process due to the presence of the ring end gap and a pressure difference above and below the ring. Another case is the flow between the ring face and cylinder liner due to ring collapse [9]. For ring collapse, the ring stays at the top of the groove during the power stroke. Since the pressure behind the ring is low, the high pressure force due to the high pressure above the ring can overcome the ring tension and the pressure force behind the ring. This causes the ring to collapse and open a wide area for gas flow.

The 2.3L engine with one ring shows very similar ring motion to the 5.4L V8 one ring engine. The major difference is that the ring motion pattern is shifted toward lower engine loads or higher manifold vacuum (consider the line 16 inches 5000 rpm and 20 inches 3500 rpm in the top ring motion plot for the 2.3L one ring engine in Figure 58 and the line between points of 12 inches 5000 rpm and 18 inches 3000 rpm in the ring motion plots for the 5.4L V8 engine with one ring in Figure 52 and Figure 53). This means that for the 2.3L one ring engine the balance between pressure and inertia forces is shifted toward the pressure forces, compare to the 5.4L engine with one ring.

INFLUENCE OF DESIGN PARAMETERS ON BLOW-BY AND RING COLLAPSE

As mentioned in the previous section, ring collapse occurs for certain combinations of pressure and inertia forces and is affected by ring tension. In order to investigate the influence of the balance between pressure and inertia forces, the mass of the top ring was halved for the 5.4L one ring engine and doubled for the 2.3L one ring engine. In order to investigate the influence of the top ring tension, the ring tension was doubled for the 5.4L one ring engine. The blow-by maps for these cases are shown in Figure 62, Figure 66, and Figure 64 respectively.

Changes of the ring mass shift the balance between pressure and inertia forces. The reduction of the ring mass for the 5.4L V8 one ring engine moves the force balance to the region of high rpm and low load making ring collapse less likely (compare Figure 47 and Figure 62). The increase of ring mass for the 2.3L one ring engine shifts the force balance

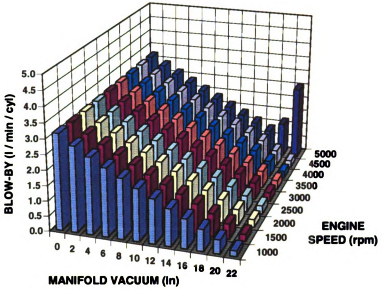

Figure 62 Predicted blow-by map from the cylinder for the 5.4L V8 engine, one ring, reduced ring mass

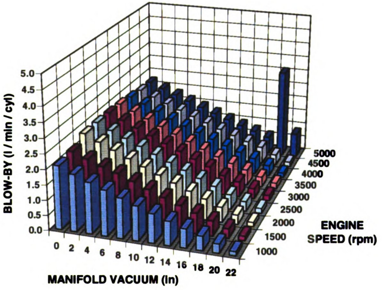

Figure 63 Predicted blow-by map from the cylinder for the 5.4L V8 engine, reduced ring mass

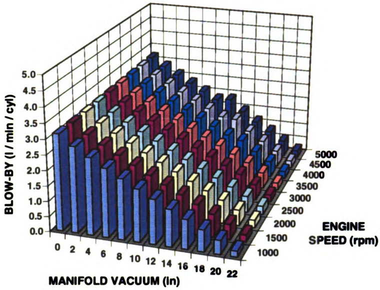

Figure 64 Predicted blow-by map from the cylinder for the 5.4L V8 engine, one ring, increased ring tension

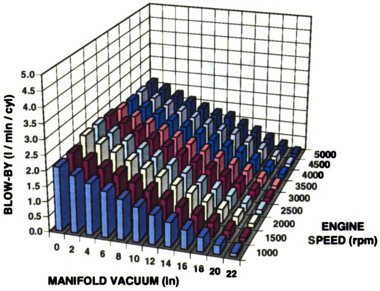

Figure 65 Predicted blow-by map from the cylinder for the 5.4L V8 engine, increased ring tension

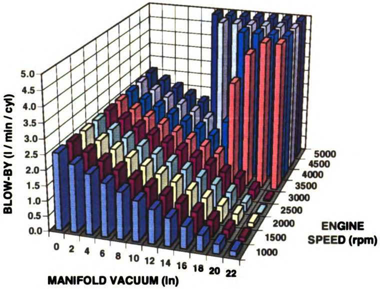

Figure 66 Predicted blow-by map from the cylinder for the 2.3L I4 engine, one ring, increased ring mass

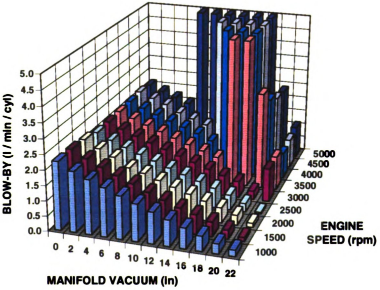

Figure 67 Predicted blow-by map from the cylinder for the 2.3L I4 engine, one ring, increased ring mass

toward lower engine speed and higher load and increases occurrences of ring collapse and ensuing blow-by spikes (compare Figure 49 and Figure 66).

Ring tension has a different effect on ring dynamics and ring collapse than does varying ring mass. It does not change axial ring motion but can prevent the ring from collapsing (Eq. (41) and Eq. (42)). The blow-by map for the 5.4L V8 one ring shows that with increased ring tension (Figure 64) no large blow-by occurs. However, high ring tension can increase ring friction and ensuing ring wear.

The ring mass and ring tension of the top ring have a similar effect on the blow-by map for the full ring set piston as on the one ring cases. The blow-by maps for the full ring set cases are shown in Figure 63, Figure 65, and Figure 67. The ring mass increase moves the force balance toward lower rpm and higher load and causes large blow-by (Figure 67). Ring mass reduction shifts the force balance to the region of high rpm and low load and reduces blow-by (Figure 63). The high top ring tension prevents ring collapse (Figure 65).

Engine Bore Stroke Ratio and Its Affect on Ring Pack Performance

Another way to shift the balance between pressure and inertia forces is to consider the engine design parameters. The pressure forces depend on the areas on which the pressure is acting. These areas are functions of the bore diameter. The inertia forces depend on piston acceleration. The piston acceleration is a function of the connecting rod length, crank radius, and engine speed (Eq. (44)). Comparing blow-by maps for the 4.6L V8 to these for the 2.3L I4 engine (Figure 35 and Figure 37), it can be seen that the force balance is shifted further to the high rpm and low load region. It is worth mentioning that both of the engines have very similar ring pack designs and the same displacement per cylinder.

The 5.4L V8 and 4.6L V8 engines have the same bore diameters and almost identical ring pack designs but different strokes. The blow-by maps for these engines (Figure 33 and Figure 35) show the shift in the force balance toward high load and low engine speed for the 5.4L engine in comparison to the 4.6L V8 engine. Based on this, it can be concluded that the bore / stroke ratio affects the ring pack performance.

Chapter 5 THREE-DIMENSIONAL RING TWIST MODELING

INTRODUCTION

Ring dynamics and ring twist have a major influence on ring pack performance. The main purpose of the ring pack is to seal the combustion chamber from its surroundings or, in other words, to prevent the combustion gases from penetrating into the crank case. In addition to its main purpose, the ring pack has to satisfy the constraints set by durability, emissions and efficiency requirements. All of these factors are self-excluding. A good ring pack design represents the compromise among all of these factors.

In recent years a number of attempts has been made to model ring pack performance including ring motion and ring twist [24, 37, 39, 46, 67, 64, 75, 74, 78]. The limitation of these attempts is in the two-dimensional approach to a truly three-dimensional phenomenon. In the case of an untwisted ring, this approach is valid and correlates well with experimental data. In the case of a twisted ring this approach has to be applied with special care because of the three-dimensional nature of ring twist. The limitations of a three-dimensional ring twist model are in its complexity, size, and time required to perform the analysis. This chapter presents the first operational three-dimensional ring twist model.

MODELING APPROACH

During an engine cycle, the ring is subjected to different kinds of loads which change in time (Figure 68). These loads include a pressure load due to a pressure difference above and below the ring, an inertia load due to piston acceleration and decceleration, a friction load due to ring contact with the cylinder liner, and an oil film damping load due to the oil film presence on the top and bottom of the ring groove. All of the loads acting on the ring can be projected as a combination of a radial force, an axial force, and a twisting moment acting at the ring cross-section center of gravity. Depending on the pressure difference above, below, and behind the ring and the position of the ring in its groove, gas flows between cavities above, below, and behind the ring. The gas flow changes the inter-ring gas pressures and the pressure load acting on the ring [16, 24, 27, 25, 37, 75]. Depending on the loads acting on the ring, the ring changes its position relative to its groove. This changes the gas flow. The whole process forms a dynamic system with multiple feed back loops [25].

In order to maintain the relative simplicity of the two-dimensional model and have the three-dimensional capability of the model, the following modeling strategy was chosen. First, the quasi-static three-dimensional ring analysis is performed. In this analysis, the ring is deformed due to a static radial load because of ring tension and a set of axial force and twisting moment pairs acting at the ring cross section center of gravity and geometrical constraints due to ring / ring groove geometry. For each pair of the twisting moment and the axial force, the ring position in the groove is determined. Based on the ring position for every load case, the clearances between the ring and its groove are calcu-

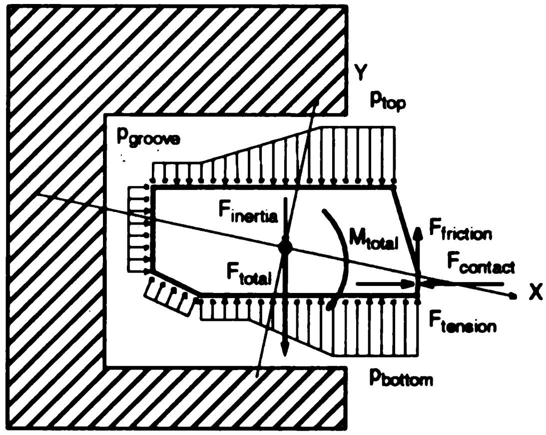

Figure 68 Forces acting on the ring

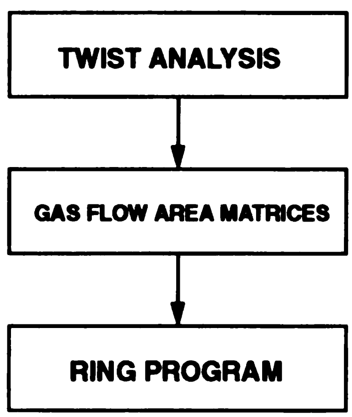

Figure 69 The Program Flow Chart

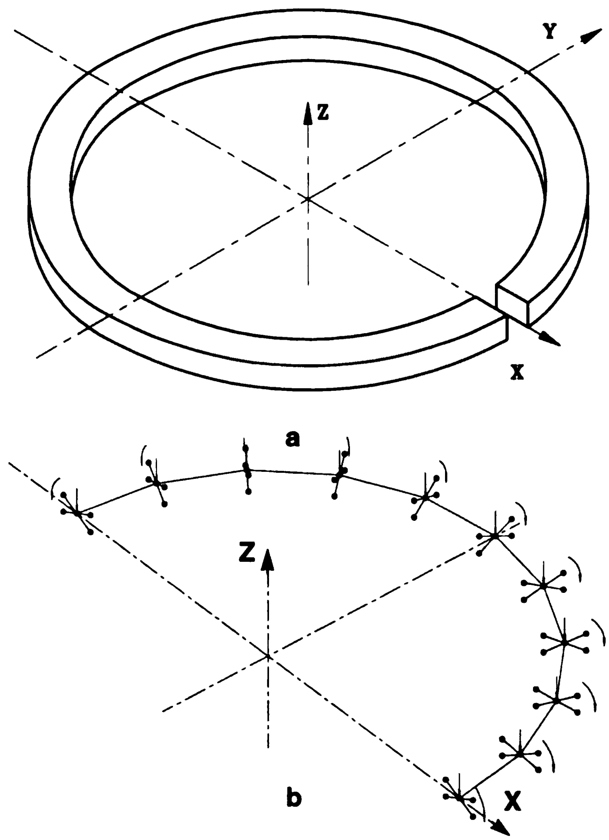

Figure 70 The actual ring view (a) vs. the three-dimensional ring beam model (b)

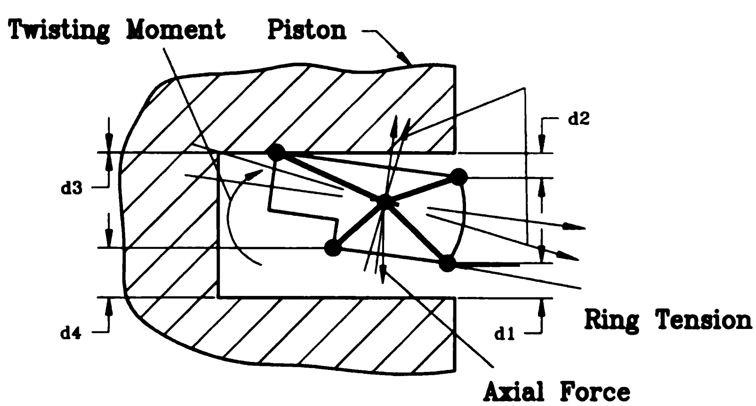

Figure 71 Ring cross section beam model

lated. These clearances determine the areas for gas flow above and below the ring. These gas flow areas, for a wide range of the axial forces and twisting moments, are then forwarded to the RING program [16, 17, 10, 9, 27, 25] and used to determine the gas flow areas at each crank angle increment during multi-cycle iterations. The flow-chart of the procedure is shown in Figure 69.

In the TWIST program, the ring is modeled with a three-dimensional Finite Element Analysis (FEA) beam model (Figure 70 and Figure 71). In order to reduce the analysis time, the model includes one half of the ring. Each cross section of the ring is modeled with five node points: four at each corner of the ring cross section and a central node located at the cross section center of gravity. The central nodes are connected with circumferential beam elements. The circumferential beam elements represent the ring itself and have the cross section properties of the ring. The corner nodes are connected to the central node with four beam elements. These beam elements have extremely high stiffness, and their purpose is to apply the displacement constraints to the end node points of the cross section due to the ring and groove geometries. With the corner node points it is possible to specify any arbitrary geometry of the ring cross section.

At each cross section central node, a combination of loads is applied. The loads include radial force due to ring tension, twisting moment due to ring tension, and two set loads: axial force and twisting moment. The radial force and twisting moment due to ring tension depend on the magnitude of the ring tension and the point where the ring tension is applied. The ring tension is assumed to be uniform around the circumference. The ring tension is applied along a circumferential line depending on the ring face profile. It is assumed that the circumferential elevation of this line does not change from one cross section to another. At the initial stage all but one of the nodes are free in all of the six degrees of freedom.

The displacement constraints due to ring and groove geometry are enforced by applying high stiffness springs at the cross section end nodes which violate the constraints. During the analysis, it is very important to ensure that the constraint springs work only on compression.

The ring twist analysis is logically subdivided into two stages. At the first stage of the analysis, the ring is "inserted" into the groove without violating the geometry constraints. During the next stage, the ring position is calculated for each pair of the axial force and the twisting moment applied at every cross section central node. Based on these calculations, the ring side clearances are determined and two matrices of gas flow areas, above and below the ring, are generated for a wide range of the twisting moments and the axial forces. The gas flow area matrices are forwarded to the RING program [16, 17, 10, 9, 27, 25] to determine the gas mass flow rates above and below the ring at every crank angle increment.

During the analysis at each crank angle increment in the RING program, all the loads acting on the ring due to pressure, inertia, friction, and oil damping forces are calculated (Figure 68). As mentioned before, all of these loads can be represented as a combination of radial force, axial force, and twisting moment acting at the ring center of gravity. Based on the pairs of the twisting moments and axial forces acting on the ring, the areas for gas flow above and below the ring are determined from the area matrices from the TWIST analysis. The gas flow areas are calculated by interpolating four neighboring entries in the area matrices

$$A = A_{(i-1,j-1)} \cdot \left(1 - \frac{F - F_{i-1}}{F_i - F_{i-1}}\right) \cdot \left(1 - \frac{W - W_{i-1}}{W_i - W_{i-1}}\right)$$
$$+ A_{(i,j-1)} \cdot \left(\frac{F - F_{i-1}}{F_i - F_{i-1}}\right) \cdot \left(1 - \frac{W - W_{i-1}}{W_i - W_{i-1}}\right)$$
$$+ A_{(i,j)} \cdot \left(\frac{F - F_{i-1}}{F_i - F_{i-1}}\right) \cdot \left(\frac{W - W_{i-1}}{W_i - W_{i-1}}\right)$$
$$+ A_{(i-1,j)} \cdot \left(1 - \frac{F - F_{i-1}}{F_i - F_{i-1}}\right) \cdot \left(\frac{W - W_{i-1}}{W_i - W_{i-1}}\right) \quad (45)$$

The crank angle iterations are repeated until the convergence is achieved. Then, the twisting moment and axial force pairs for each crank angle increment can be used in the TWIST program to calculate the actual ring position in the groove at each crank angle increment over the whole engine cycle.

THREE-DIMENSIONAL FEA BEAM MODEL

The ring twist model uses a general three-dimensional structural analysis algorithm. The key model assumptions can be summarized as follows. The structure is perfectly elastic. Beam elements are represented by straight lines and have uniform section properties between their two node points. Axial forces act along the centroidal axis of beam elements. The shear center of a beam element cross section coincides with the centroid of the section. Only small deflections are considered.

The structure to be analyzed is assumed to lay in the three-dimensional space. The global coordinate system is used to describe the locations of nodes points, node point displacements, external loads to the system, and reaction of supports (Figure 72). A local coordinate system (Figure 73) is assigned to each element. The local coordinate system is

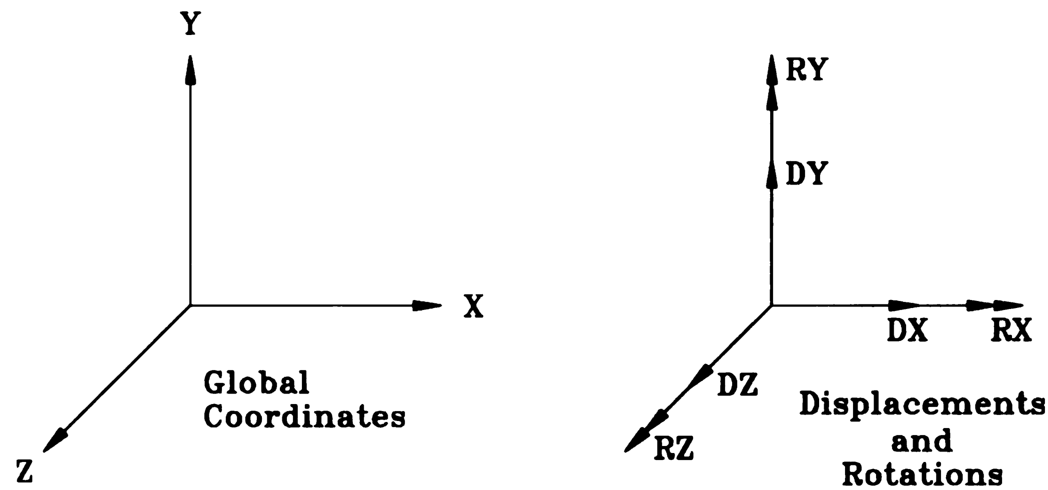

Figure 72 Global coordinate system and displacements and rotations in the global coordinate system

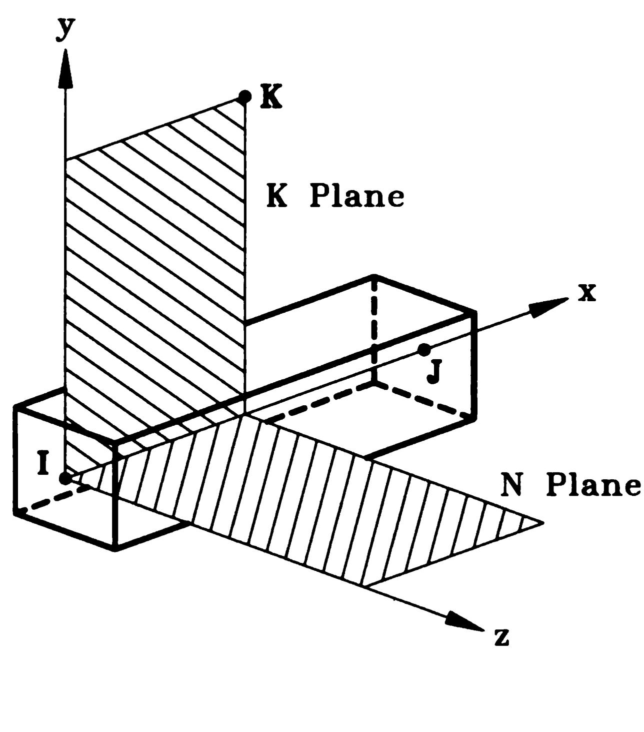

Figure 73 Plane locations in the local coordinate system

necessary to define the element loadings, orientation of the element cross section, and the end reaction forces. The K-plane contains nodes I, J, and K. The N-plane is normal to the K-plane. The K- and N-planes are the planes formed by the cross section principal axes. The coordinate transformation between the local and global system is the following:

$$\{u\} = [\lambda]\{U\} \tag{46}$$

where $\{u\}$ is the local coordinate vector, $\{U\}$ is the global coordinate vector, and $[\lambda]$ is the directional cosines matrix.

In the model, the direct stiffness method is used to determine the node point displacements, element end forces, and stresses. In this method, the element stiffness properties are combined into a local stiffness matrix $[k]$. The local stiffness matrices are assembled into a global stiffness matrix $[K]$. Nodal forces and moments are transformed into a global load vector $\{P\}$. Nodal displacements $\{U\}$ are found by solving the matrix equation

$$[K]\{U\} = \{P\} \tag{47}$$

The beam element is assumed to a straight bar of uniform cross section capable of resisting axial forces, bending moments about the two principal axes in the plane of its cross section, and torsional moments about its centroid axis. The forces and moments acting on the beam element are the following: axial forces S_1 and S_7; shearing forces S_2, S_3; S_8, and S_9; bending moments S_5, S_6, S_{11}, and S_{12}; and torsional moments S_4 and S_{10}. The locations and positive directions of these forces and moments are shown in Figure 74.

The element stiffnesses form a 12x12 matrix. According to the bending and torsion theory, the axial and torsional displacements can be considered independently. In addition,

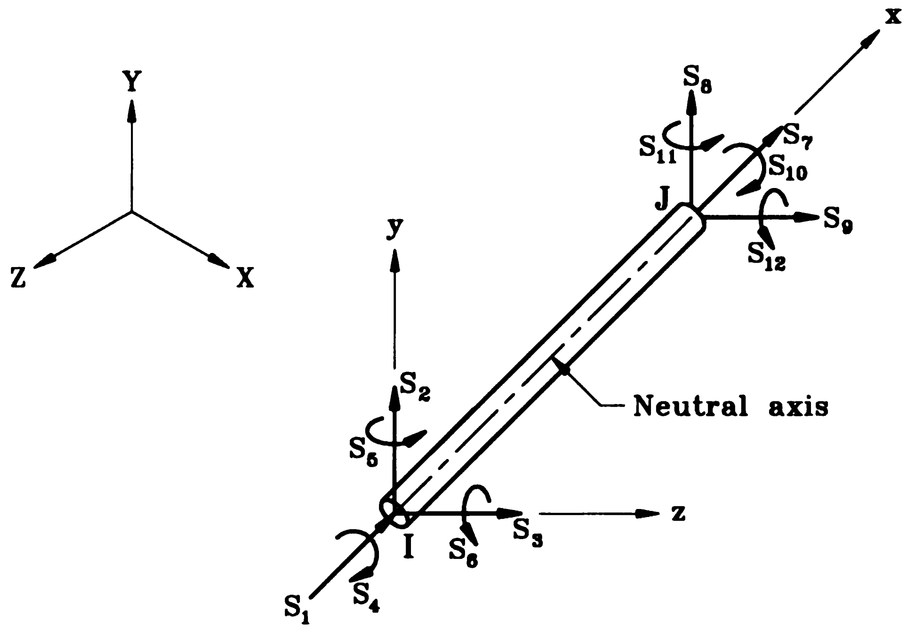

Figure 74 Forces and moments in the local coordinate system

the displacements due to shear forces and bending moments in the *xy* and *xz* planes can be analyzed independently as well because the cross section principal axes lay in the local *xy* and *xz* planes.

Axial Forces (S_1 and S_7)

The governing differential equation for the axial displacements is the following:

$$S_1 = -EA \cdot \left(\frac{du}{dx}\right) \tag{48}$$

After direct integration and applying the boundary conditions shown in Figure 75, it yields:

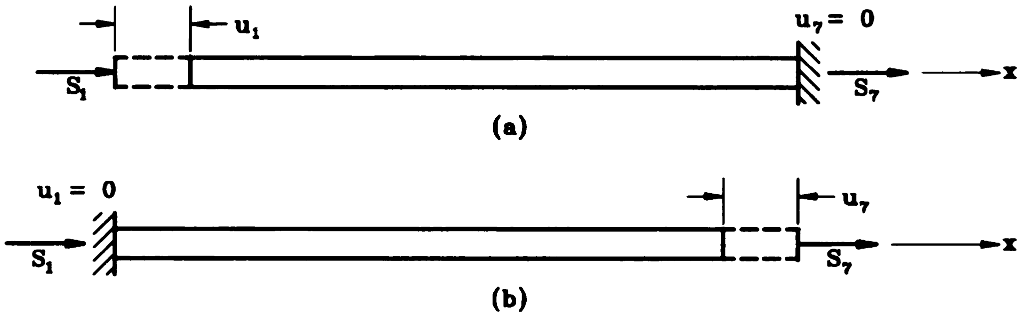

Figure 75 Axial forces

$$S_1 = \frac{EA}{L}u_1 \tag{49}$$

The individual entries into the total stiffness matrix due to symmetry are

$$k_{1,1} = \frac{EA}{L} \tag{50}$$

$$k_{1,1} = k_{7,7} = -k_{7,1} = -k_{1,7} \tag{51}$$

Torsional Moments (S_4 and S_{10})

The governing differential equation for the twist of the beam is the following:

$$S_4 = -GJ \cdot \left(\frac{d\theta}{dx}\right) \tag{52}$$

where $G\,J$ is the torsional stiffness of the beam cross section. After direct integration and applying the boundary conditions shown in Figure 76, it yields

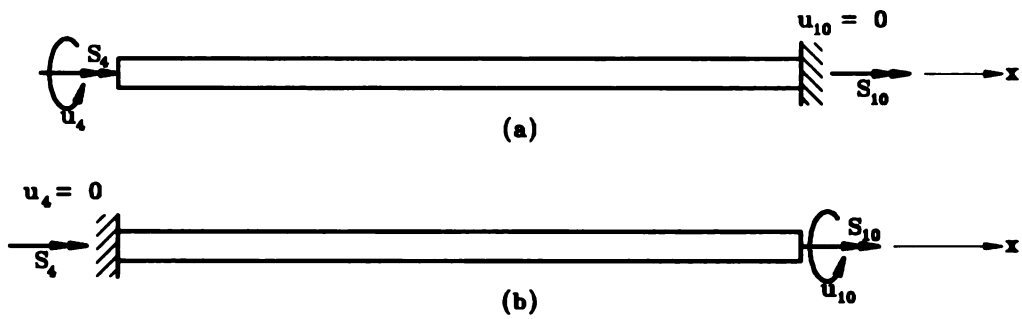

Figure 76 Torsional moments

$$S_4 = \frac{GJ}{L}u_4 \tag{53}$$

The individual entries into the element stiffness matrix due to symmetry are

$$k_{4,4} = \frac{GJ}{L} \tag{54}$$

$$k_{4,4} = k_{10,10} = -k_{4,10} = -k_{10,4} \tag{55}$$

Shearing Forces (S_2 and S_8)

The lateral deflection v of the beam element with applied shearing forces and associated moments is given by

$$v = v_b + v_s \tag{56}$$

where v_b is the lateral deflection due to bending and v_s is the additional deflection due to shearing strains, such that

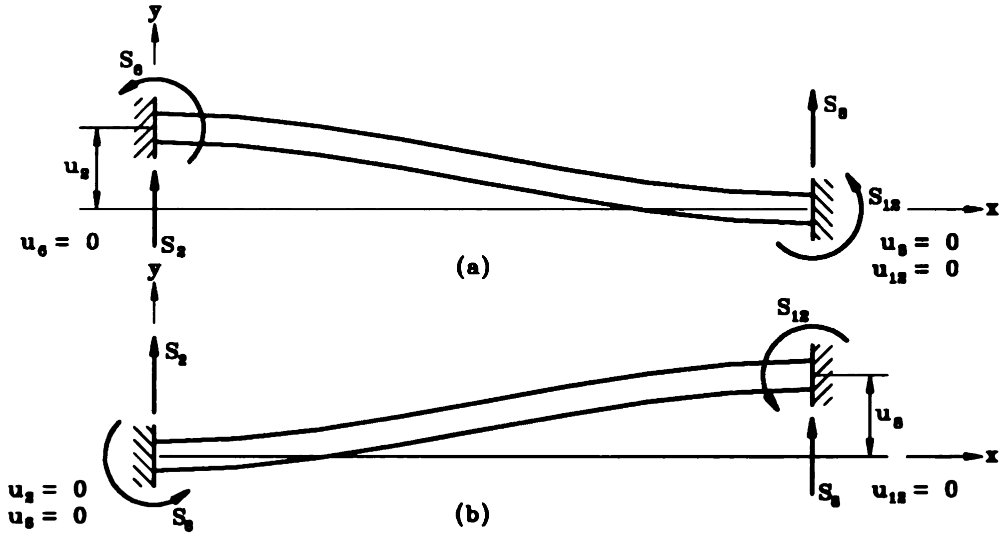

Figure 77 Shear forces

$$\frac{dv_s}{dx} = -\frac{S_2}{GA_y} \tag{57}$$

where A_y is the beam effective shear area.

The bending deflection is governed by the following differential equation:

$$EI_z\frac{d^2v_b}{dx^2} = S_2x - S_6 \tag{58}$$

After direct integration, applying the boundary conditions shown in Figure 77, and using the equations of equilibrium, it yields

$$EI_zv = \frac{S_2x^3}{6} - \frac{S_6x^2}{2} - \frac{S_2\phi_yxL^2}{12} + (1+\phi_y)\frac{L^3S_2}{12} \tag{59}$$

where:

$$\phi_y = \frac{12 I_z}{G A_y L^2} \tag{60}$$

$$S_6 = \frac{S_2 L}{2} \tag{61}$$

$$u_2 = (1 + \phi_y) \frac{L^3 S_2}{12 E I_z} \tag{62}$$

The individual entries into the element stiffness matrix are

$$k_{2,2} = \frac{S_2}{u_2} = \frac{12 E I_z}{(1 + \phi_y) L^3} \tag{63}$$

$$k_{6,2} = \frac{S_6}{u_2} = \frac{S_2 L}{2 u_2} = \frac{6 E I_z}{(1 + \phi_y) L^2} \tag{64}$$

$$k_{8,2} = \frac{S_8}{u_2} = -\frac{12 E I_z}{(1 + \phi_y) L^3} \tag{65}$$

$$k_{12,2} = \frac{S_{12}}{u_2} = \frac{S_2 L - S_6}{u_2} = \frac{6 E I_z}{(1 + \phi_y) L^2} \tag{66}$$

$$k_{8,8} = k_{2,2} \tag{67}$$

$$k_{12,8} = -k_{6,2} \tag{68}$$

Bending Moments (S_6 and S_{12})

The deflections due to bending moments S_6 and S_{12} are governed by the same differential Eq. (58) as for the shearing forces S_2 and S_8 but with different boundary condi-

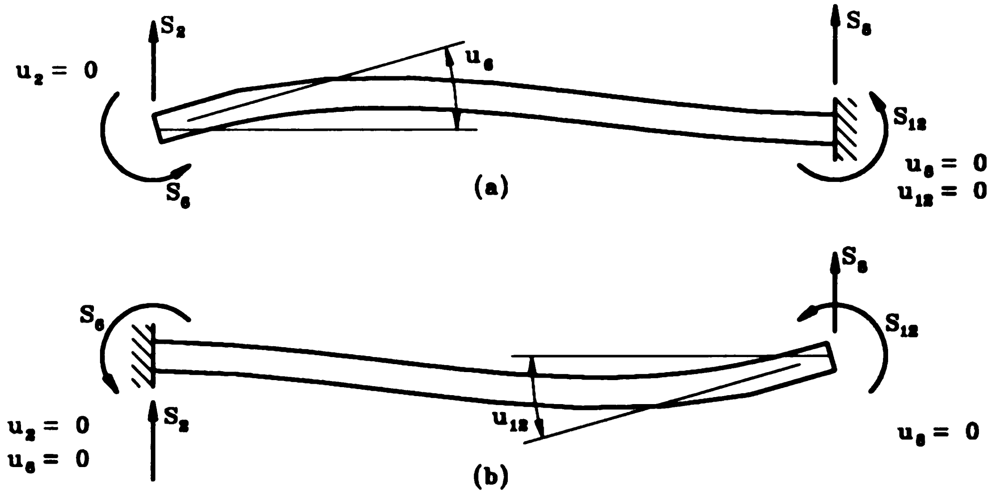

Figure 78 Bending moments

tions as shown in Figure 78. After direct integration, applying the boundary conditions, and using the equations of equilibrium, it yields

$$EI_z v = \frac{S_2}{6}(x^3 - L^2 x) + \frac{S_6}{2}(Lx - x^2) \tag{69}$$

$$S_2 = \frac{6S_6}{(4 + \phi_y)L} \tag{70}$$

$$\phi_y = \frac{12I_z}{GA_y L^2} \tag{71}$$

$$u_6 = \frac{S_6(1 + \phi_y)L}{EI_z(4 + \phi_y)} \tag{72}$$

The individual entries into the element stiffness matrix are

$$k_{6,6} = \frac{S_6}{u_6} = \frac{(4+\phi_y)EI_z}{(1+\phi_y)L} \tag{73}$$

$$k_{8,6} = \frac{S_8}{u_6} = -\frac{S_2}{u_6} = -\frac{6EI_z}{(1+\phi_y)L^2} \tag{74}$$

$$k_{12,6} = \frac{S_{12}}{u_6} = \frac{S_2 L - S_6}{u_6} = \frac{(2-\phi_y)EI_z}{(1+\phi_y)L} \tag{75}$$

$$k_{12,12} = k_{6,6} \tag{76}$$

Shearing Forces (S_3 and S_9)

The case of the shearing forces S_3 and S_9 is similar to the case of the shearing forces S_2 and S_8 but with the opposite sign convention.

Bending Moments (S_5 and S_{11})

The case of the bending moments S_5 and S_{11} is similar to the case of the bending moments S_6 and S_{12} but with the opposite sign convention.

Beam Element Stiffness Matrix:

$$\{S\} = \begin{bmatrix} k_{11} & k_{12} \\ k_{21} & k_{22} \end{bmatrix} \{U\} \tag{77}$$

where:

$$\{S\} = \begin{bmatrix} S_1 & S_2 & S_3 & S_4 & S_5 & S_6 & S_7 & S_8 & S_9 & S_{10} & S_{11} & S_{12} \end{bmatrix}^T \tag{78}$$

$$\{U\} = [U_1 U_2 U_3 U_4 U_5 U_6 U_7 U_8 U_9 U_{10} U_{11} U_{12}]^T \tag{79}$$

$$[k_{11}] = \begin{bmatrix} \frac{EA}{L} & 0 & 0 & 0 & 0 & 0 \\ 0 & \frac{12EI_z}{L^3(1+\phi_y)} & 0 & 0 & 0 & \frac{6EI_z}{L^2(1+\phi_y)} \\ 0 & 0 & \frac{12EI_y}{L^3(1+\phi_z)} & 0 & \frac{-6EI_y}{L^2(1+\phi_z)} & 0 \\ 0 & 0 & 0 & \frac{GJ}{L} & 0 & 0 \\ 0 & 0 & \frac{-6EI_y}{L^2(1+\phi_z)} & 0 & \frac{(4+\phi_z)EI_y}{L(1+\phi_z)} & 0 \\ 0 & \frac{6EI_z}{L^2(1+\phi_y)} & 0 & 0 & 0 & \frac{(4+\phi_y)EI_z}{L(1+\phi_y)} \end{bmatrix} \tag{80}$$

$$[k_{12}] = \begin{bmatrix} -\frac{EA}{L} & 0 & 0 & 0 & 0 & 0 \\ 0 & \frac{-12EI_z}{L^3(1+\phi_y)} & 0 & 0 & 0 & \frac{6EI_z}{L^2(1+\phi_y)} \\ 0 & 0 & \frac{-12EI_y}{L^3(1+\phi_z)} & 0 & \frac{-6EI_y}{L^2(1+\phi_z)} & 0 \\ 0 & 0 & 0 & -\frac{GJ}{L} & 0 & 0 \\ 0 & 0 & \frac{6EI_y}{L^2(1+\phi_z)} & 0 & \frac{(2-\phi_z)EI_y}{L(1+\phi_z)} & 0 \\ 0 & \frac{-6EI_z}{L^2(1+\phi_y)} & 0 & 0 & 0 & \frac{(2-\phi_y)EI_z}{L(1+\phi_y)} \end{bmatrix} \tag{81}$$

$$
[k_{21}] = \begin{bmatrix}
-\frac{EA}{L} & 0 & 0 & 0 & 0 & 0 \\
0 & \frac{-12EI_z}{L^3(1+\phi_y)} & 0 & 0 & 0 & \frac{-6EI_z}{L^2(1+\phi_y)} \\
0 & 0 & \frac{-12EI_y}{L^3(1+\phi_z)} & 0 & \frac{6EI_y}{L^2(1+\phi_z)} & 0 \\
0 & 0 & 0 & -\frac{GJ}{L} & 0 & 0 \\
0 & 0 & \frac{-6EI_y}{L^2(1+\phi_z)} & 0 & \frac{(2-\phi_z)EI_y}{L(1+\phi_z)} & 0 \\
0 & \frac{6EI_z}{L^2(1+\phi_y)} & 0 & 0 & 0 & \frac{(2-\phi_y)EI_z}{L(1+\phi_y)}
\end{bmatrix} \tag{82}
$$

$$
[k_{22}] = \begin{bmatrix}
\frac{EA}{L} & 0 & 0 & 0 & 0 & 0 \\
0 & \frac{12EI_z}{L^3(1+\phi_y)} & 0 & 0 & 0 & \frac{-6EI_z}{L^2(1+\phi_y)} \\
0 & 0 & \frac{12EI_y}{L^3(1+\phi_z)} & 0 & \frac{6EI_y}{L^2(1+\phi_z)} & 0 \\
0 & 0 & 0 & \frac{GJ}{L} & 0 & 0 \\
0 & 0 & \frac{6EI_y}{L^2(1+\phi_z)} & 0 & \frac{(4+\phi_z)EI_y}{L(1+\phi_z)} & 0 \\
0 & \frac{-6EI_z}{L^2(1+\phi_y)} & 0 & 0 & 0 & \frac{(4+\phi_y)EI_z}{L(1+\phi_y)}
\end{bmatrix} \tag{83}
$$

MODEL APPLICATION

The model described in the previous section was applied to a production gasoline engine. In order to compare the results, the twist analysis was performed for both the top

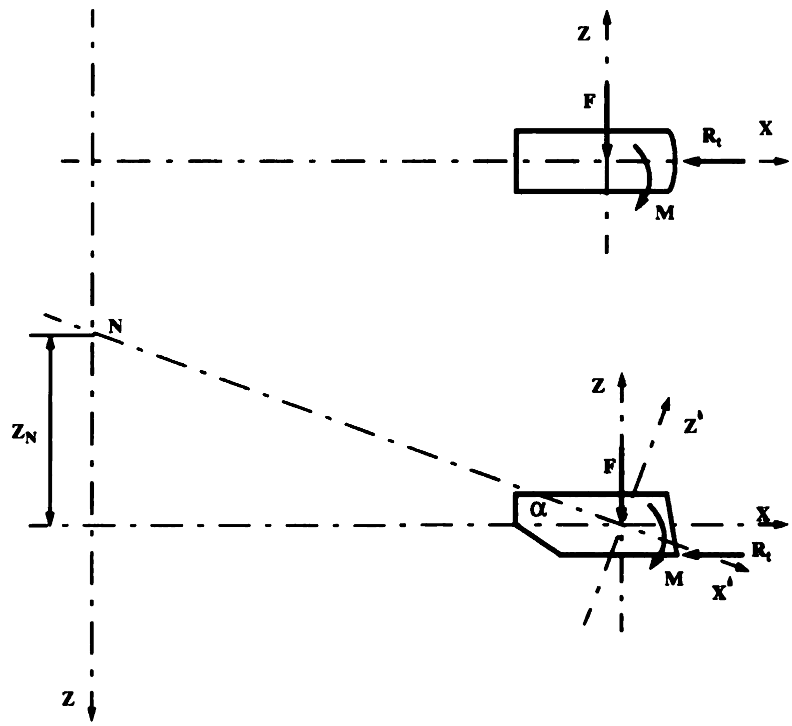

Figure 79 Top (a) and second (b) compression ring configuration

and second compression rings. The twist data obtained was used for comparison of the original RING program calculations and the calculations using the new feature.

A typical ring pack for a gasoline engine includes an untwisted top compression ring with a barrel face profile and a negatively twisted second compression ring with a taper face profile (Figure 79). The principal differences between the two rings that affects the twist capabilities can be characterized by two factors: the point of the ring face-cylinder liner contact and the orientation of the ring cross section principal axes. The contact point affects the initial (static) ring twist due to ring tension and ring conformability to the cylinder bore. In the case of the top compression ring with a barrel face profile without offset, the ring tension causes a static radial force on the ring cross section and no initial static twisting moment. In the case of the second compression ring with a taper face profile, the contact force due to ring tension is applied with an offset. In addition to a static radial force, this causes an initial static twisting moment.

The orientation of the cross section principal axes depends on symmetry of the cross section [9, 71, 84]. The principal axes of the top ring lay in the plane of the ring due to the symmetry of the ring cross section. Because of the asymmetry of the second ring cross section, its principal axes are pivoted by angle α and do not lay in the plane of the ring. The major consequence of the pivoted principal axes is in the nature of the ring twist. In the case of the principal axes laying in the plane of the ring, the ring twists in the plane of the ring. If the principal axes do not lay in the plane of the ring, the ring does not twist in the plane of the ring [84]. For this case of the ring cross section geometry, a three-dimensional ring twist model has to be considered.

GAS FLOW AREA MATRICES

The gas flow area matrices represent the twist characteristics of the ring. The difference between the gas flow area matrices for the top and second compression rings is determined by the differences in the nature of the twist for each ring. The gas flow areas above and below the ring for the top and second compression rings are shown in Figure 80 and Figure 81 respectively.

The ring position in the groove depends on the ring material properties, geometry of the ring cross section, initial static radial force, initial static twisting moment due to ring tension, and an applied load case (twisting moment and axial force). In the case of the axial force acting upward and a zero twisting moment, the top untwisted compression ring stays at the top of the groove opening the passage for gas flow below it and closing the

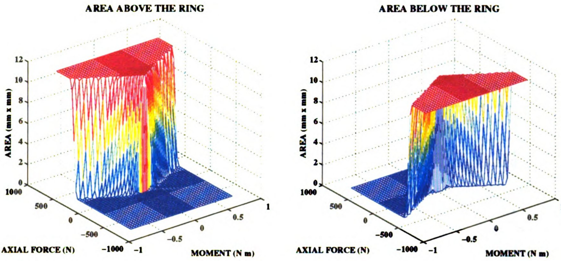

Figure 80 Gas flow areas above and below the ring vs. axial force and twisting moment for the top compression ring

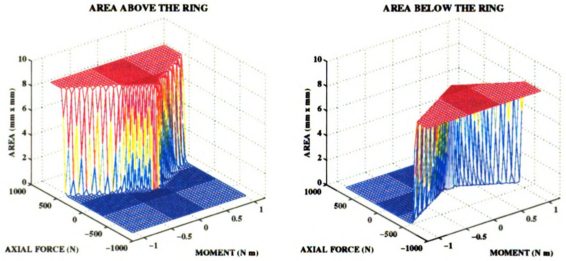

Figure 81 Gas flow areas above and below the ring vs. axial force and twisting moment for the second compression ring

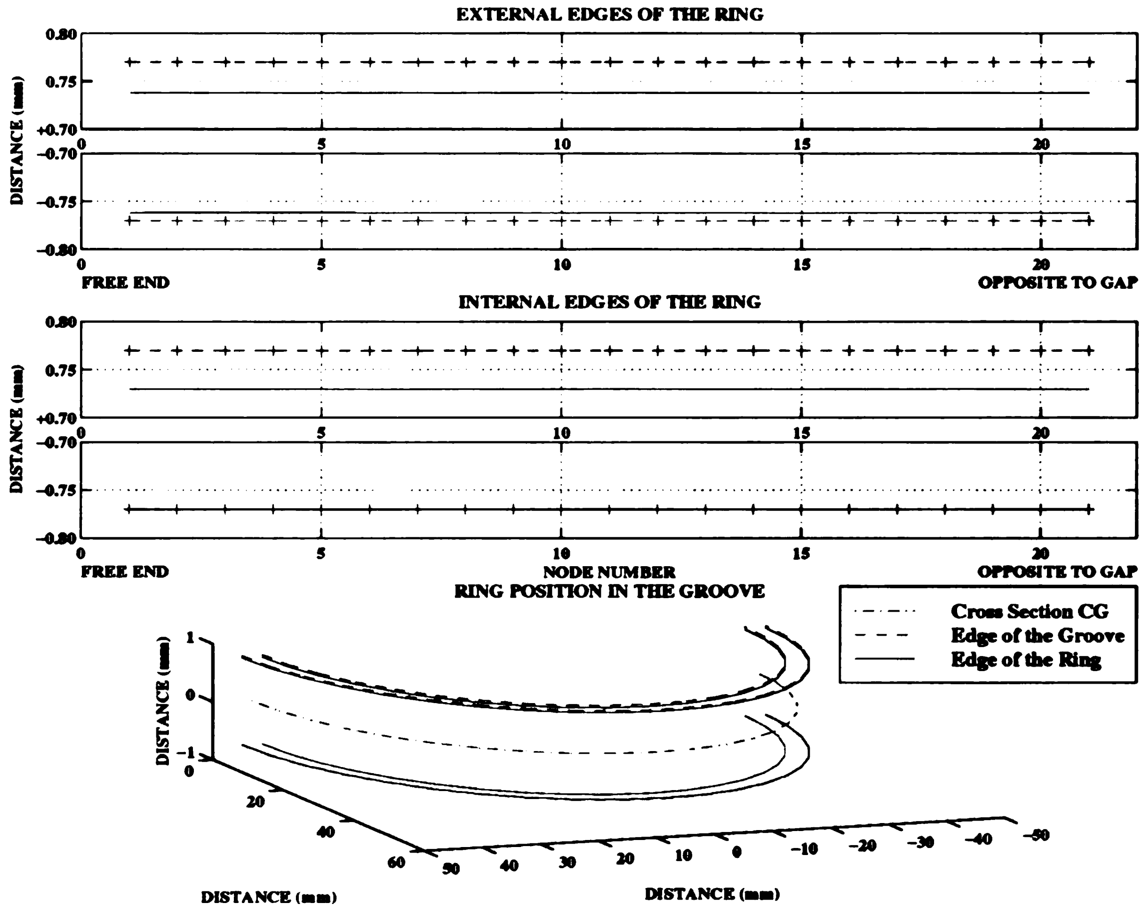

Figure 82 Top compression ring position in the groove for an axial force 66.8485 N and twisting moment 0.1495 Nm

area for gas flow above it. If the axial force acts downward and the twisting moment is zero, the top compression ring stays at the bottom of the groove opening the area above it and closing the area below it. In the case of small or zero axial force and high twisting moment, the ring twists and stays in contact with the top of the groove and the bottom of the groove with one of its edges, depending on the direction of the twisting moment. In the case of the second ring, two additional factors need to be considered. First, the second compression ring has an initial static twist. Second, the ring does not twist uniformly due to an asymmetric ring cross section. Figure 82 and Figure 83 show examples of the ring

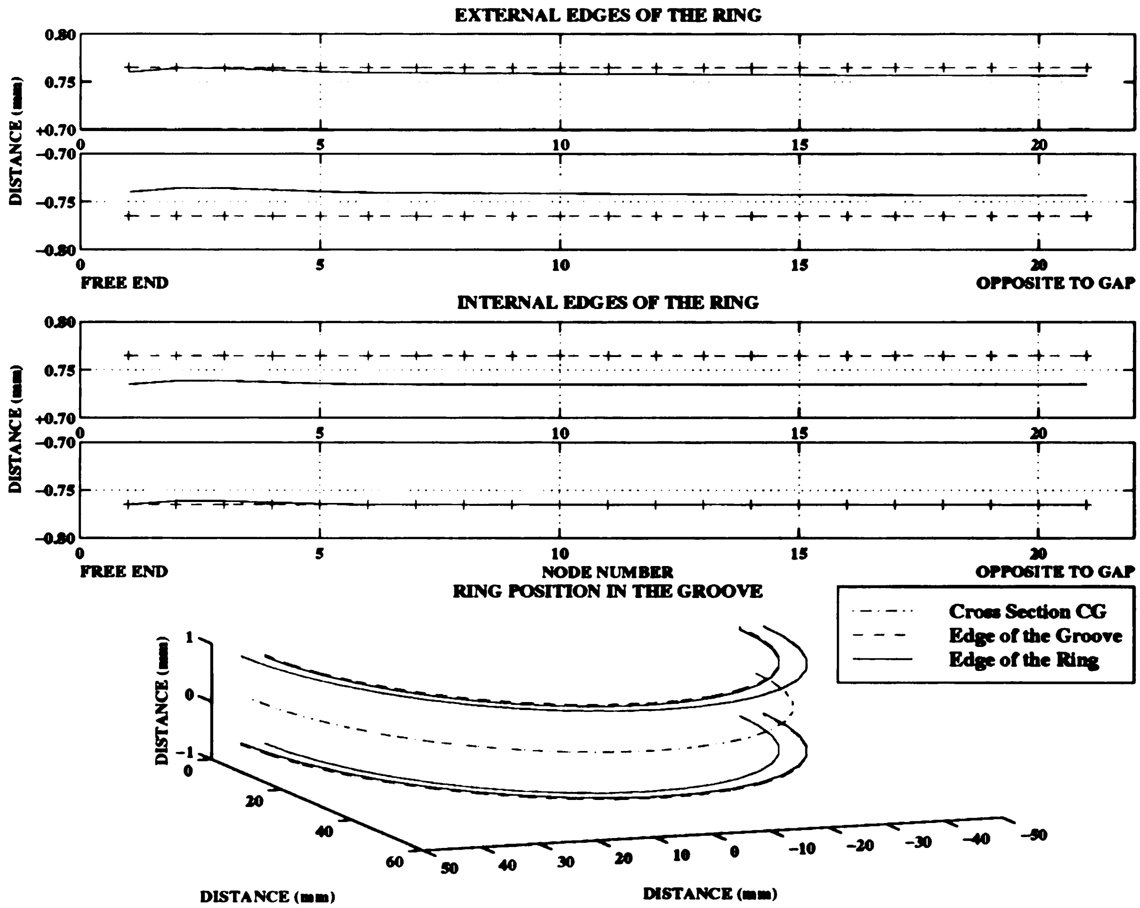

Figure 83 Second compression ring position in the groove for an axial force 10.4689 N and twisting moment 0.2276 Nm

position in the groove for the top and second compression rings. It should be mentioned again that each result from these figures represents only one entry in the area matrices shown in Figure 80 and Figure 81.

The comparison of the gas flow areas for the top and second compression rings gives three major differences: the location of the tip, the type of the edges, and the vertex angle. The vertex angle depends on the ring torsional resistance. Ring torsional resistance is a function of the cross section torsional constant and the modulus of elasticity of the ring material.

The type of the edges depends on the difference in the nature of the twist for the top and second rings. The top ring areas show sharp edges between the ring position at the top and the bottom of the groove. However, for the second ring, these edges are rounded. The second ring does not twist uniformly around the circumference because its cross section principal axes do not lay in the plane of the ring.

The tip position describes the initial static ring twist. The different tip position (different static twist) for the top and second rings is due to a difference in initial static twisting moments. As mentioned before, the initial twisting moment depends on ring tension and the position of the contact point between the ring face and the cylinder liner. In the case of the top compression ring with a barrel face profile without offset, the ring tension does not give an initial twisting moment. However, in the case of the second ring with a taper face, the ring face / cylinder liner contact point lays off the ring cross section center line causing an initial twisting moment.

ENGINE CYCLE ANALYSIS

The engine cycles were modeled for a gasoline IC engine for 2000 rpm and 50.8 mm (2 inches) of mercury manifold vacuum. The combustion chamber pressure, inter-ring gas pressures, and corresponding ring positions (area ratios) are shown in Figure 84, Figure 85, Figure 86, and Figure 87. The top and second ring motions for the plots in Figure 84 are calculated with the ring twist data from the flow area matrices. In Figure 85 the second ring motion is calculated with the ring twist data from the flow area matrices. The calculations of the top ring motion do not include the ring twist data. In Figure 86 the top ring motion is calculated with the ring twist data from the gas flow matrices. The cal-

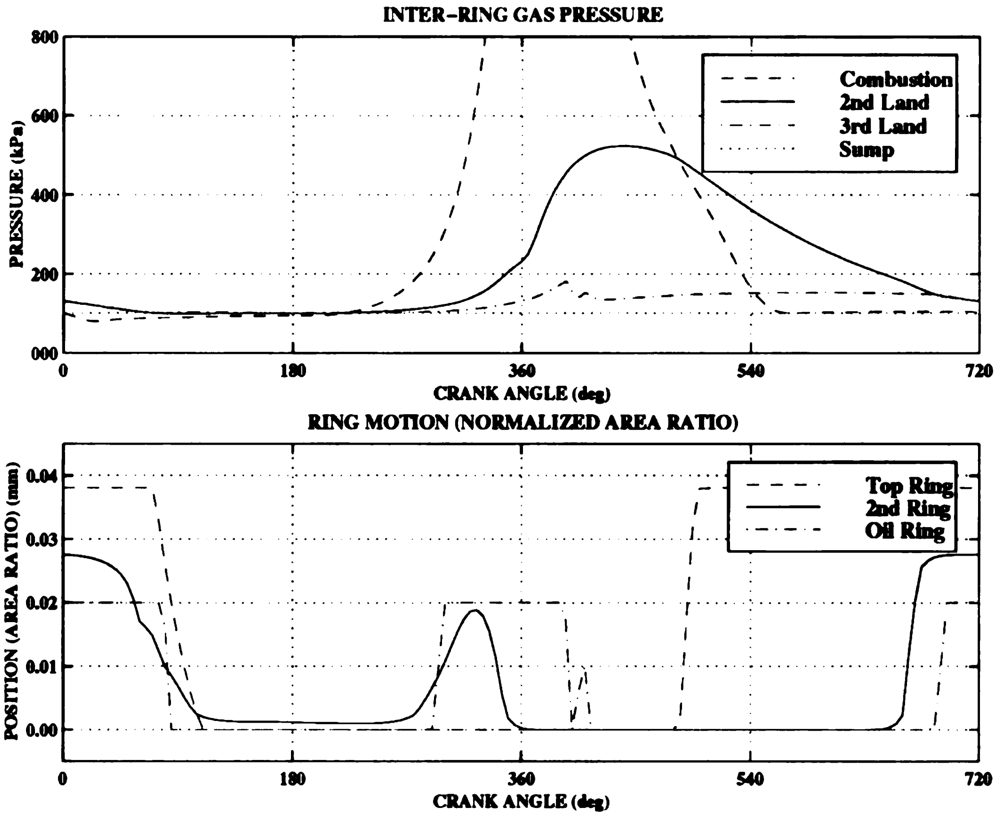

Figure 84 Inter-ring gas pressures and ring positions for 2000 rpm 2 inch manifold vacuum. Calculations of the top and second ring positions include ring twist. Note: the graphs for the top and second ring positions show the average scaled area ratios.

culations of the second compression ring motion do not include the ring twist data. In Figure 87, the top and second ring motions are calculated without the ring twist data. For the case without the ring twist calculation (the top ring in Figure 85, the second ring in Figure 86, and the top and second rings in Figure 87), the plots show the actual ring position in the groove vs. crank angle. For the case of the calculations including the ring twist data (the top and second compression rings in Figure 84, the second ring in Figure 85, and the top ring in Figure 86, the plots show averaged scaled area ratios

$$x = \frac{A_2}{A_1 + A_2} \cdot d_{gr} \quad (84)$$

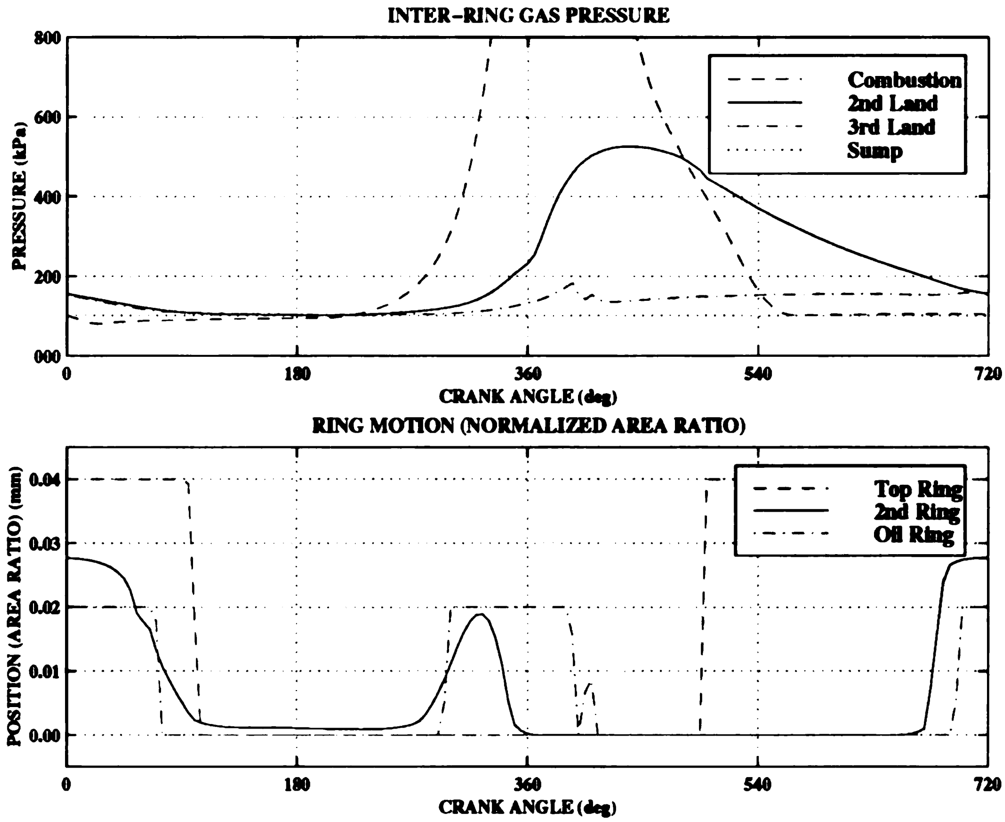

Figure 85 Inter-ring gas pressure and ring position for 2000 rpm 2 inch manifold vacuum. Calculations of the second ring position include ring twist. Calculation for the top ring position do not include ring twist. Note: the graph for the second ring position shows the average scaled area ratio.

where A_1 is the area below the ring, A_2 is the area above the ring, and the d_{gr} is the side clearance between the ring and its groove (the difference between the groove height and the ring thickness). For the case with no twist calculations, the average scaled area ratio is identical to the position of the ring center of gravity.

Piston ring dynamics is primarily controlled by three factors: pressure forces, inertia forces, and friction forces as well as moments associated with them [16, 25]. It is easier to understand the ring dynamics first without considering the ring twist (Figure 87). At the beginning of the cycle (zero degree crank angle, the piston at Top Dead Center [TDC]) all

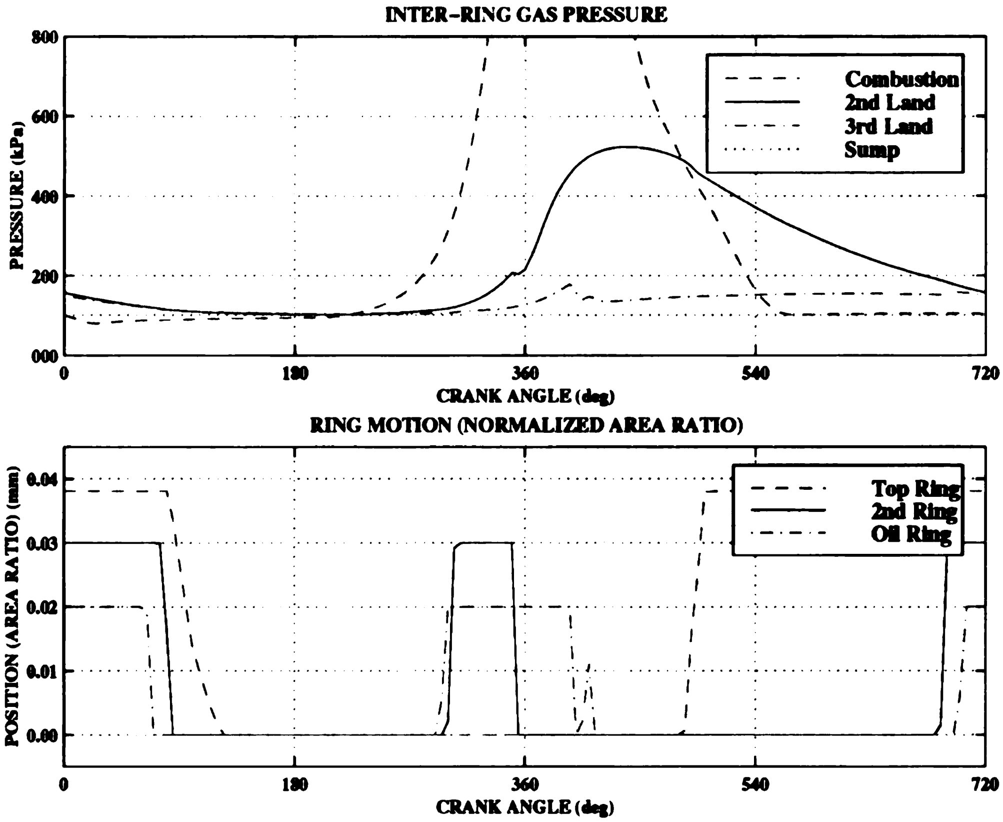

Figure 86 Inter-ring gas pressure and ring position for 2000 rpm 2 inch manifold vacuum. Calculations of the top ring position include ring twist. Calculation for the second ring position do not include ring twist. Note: the graph for the top ring position shows the average scaled area ratio.

of the rings stay at the top of their grooves because the inertia forces act upward and the pressure differences above and below each ring are small. As the piston passes the mid-stroke, the inertia force changes direction, causing the rings to move to the bottom of their grooves. The rings do not move simultaneously because of different pressures above and below each ring, different areas exposed to the pressures, and different ring masses (different inertia forces). During the compression and most of power stroke, the top ring still stays at the bottom of the groove. Even though at this crank angle interval the inertia force pushes the ring upward during the second half of the compression stroke and the first half

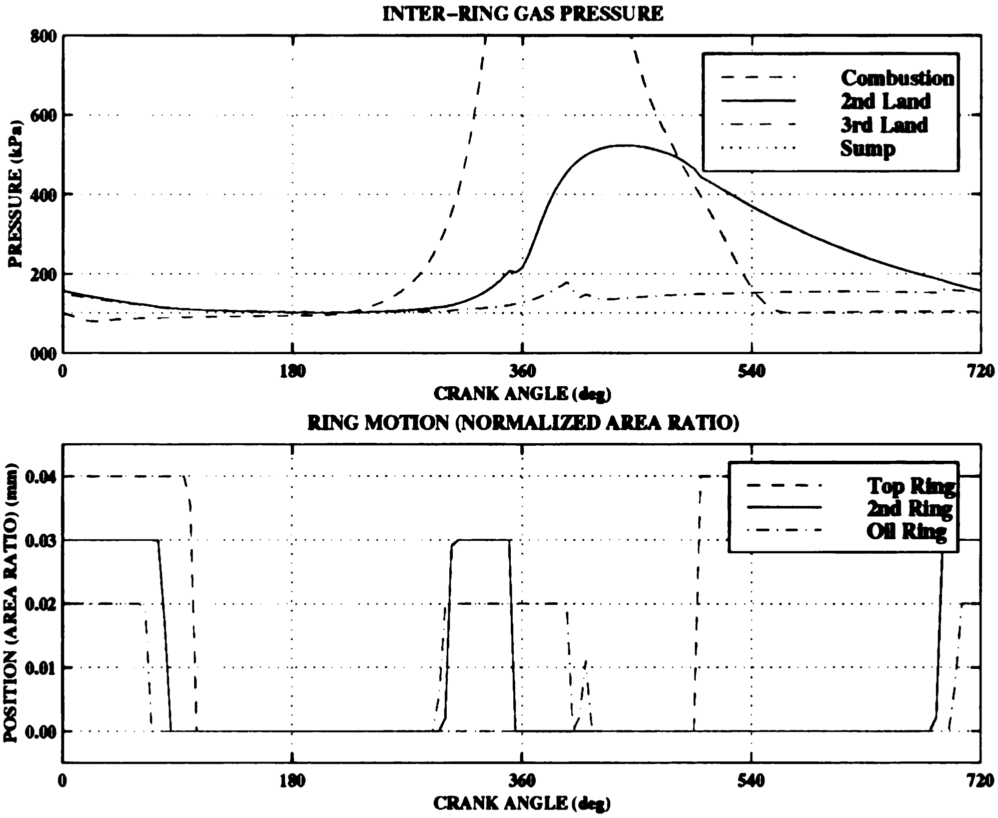

Figure 87 Inter-ring gas pressure and ring position for 2000 rpm 2 inch manifold vacuum. Calculations for the top and second ring positions do not include ring twist.

of the power stroke, the high pressure force due to high in-cylinder pressure keeps the ring at the bottom of the groove. By the end of the power stroke, the combustion chamber pressure drops while the second land pressure remains high due to blow-by from the combustion chamber into the second land during the compression and power stroke. Even though at this crank angle interval the inertia force acts downward, the pressure force due to pressure difference above and below the ring pushes the ring to the top of the groove. The ring stays there until the end of the cycle. The second ring stays at the bottom of the groove until the second half of the compression stroke. At this point, the inertia force acting upward overcomes the pressure force, moving the ring to the top of the groove. As the sec-

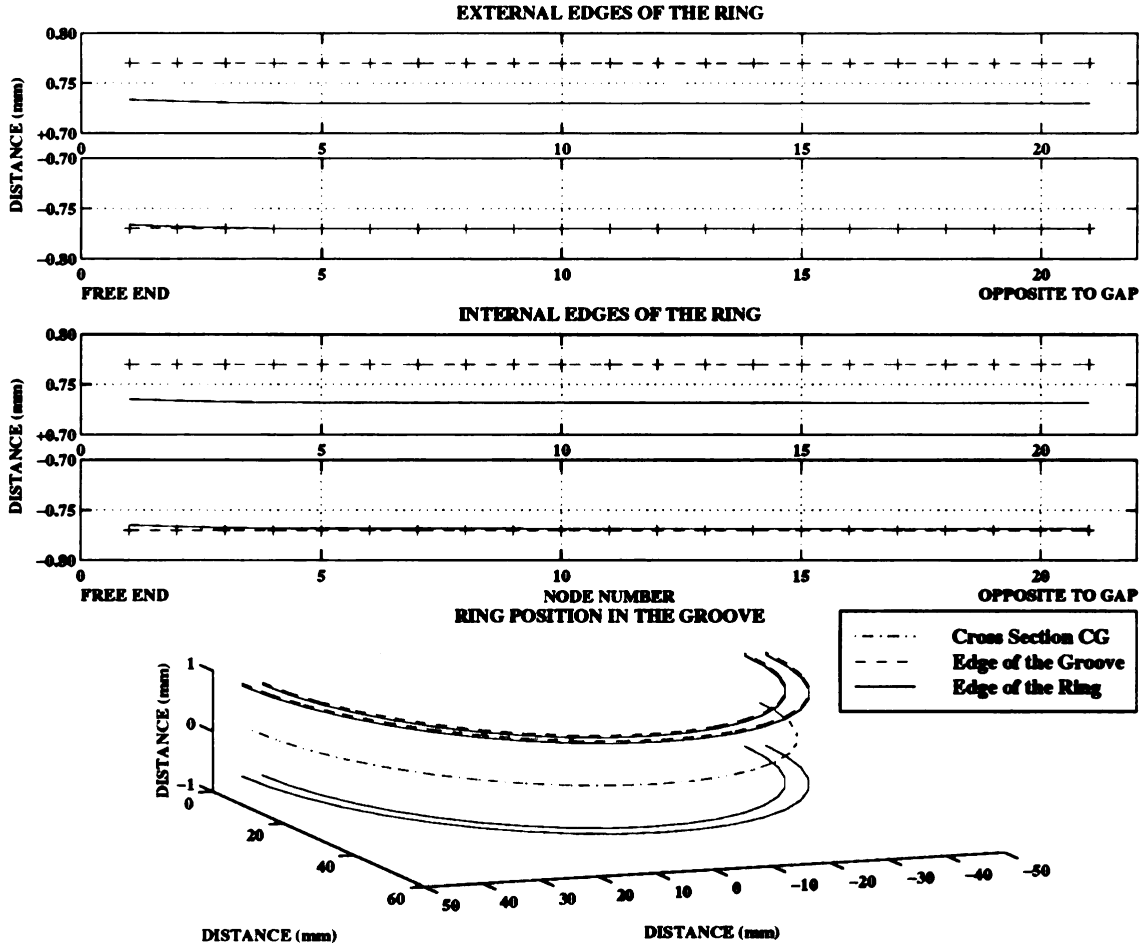

Figure 88 Top compression ring position in the groove at 97 degrees of crank angle

ond land pressure builds up due to blow-by past the top ring, the pressure force overcomes the inertia force and moves the ring to the bottom of the groove. The second ring stays at the bottom of the groove until the end of the exhaust stroke when the inertia force acts upward and the second land pressure has dropped. The third ring dynamics are very similar to those of the second ring with a few exceptions. The third ring stays longer at the top of the groove at the end of the compression stroke and the first half of the power stroke because at this moment its motion is mostly controlled by the inertia force due to a lower pressure difference above and below the ring and higher ring mass compared to the second

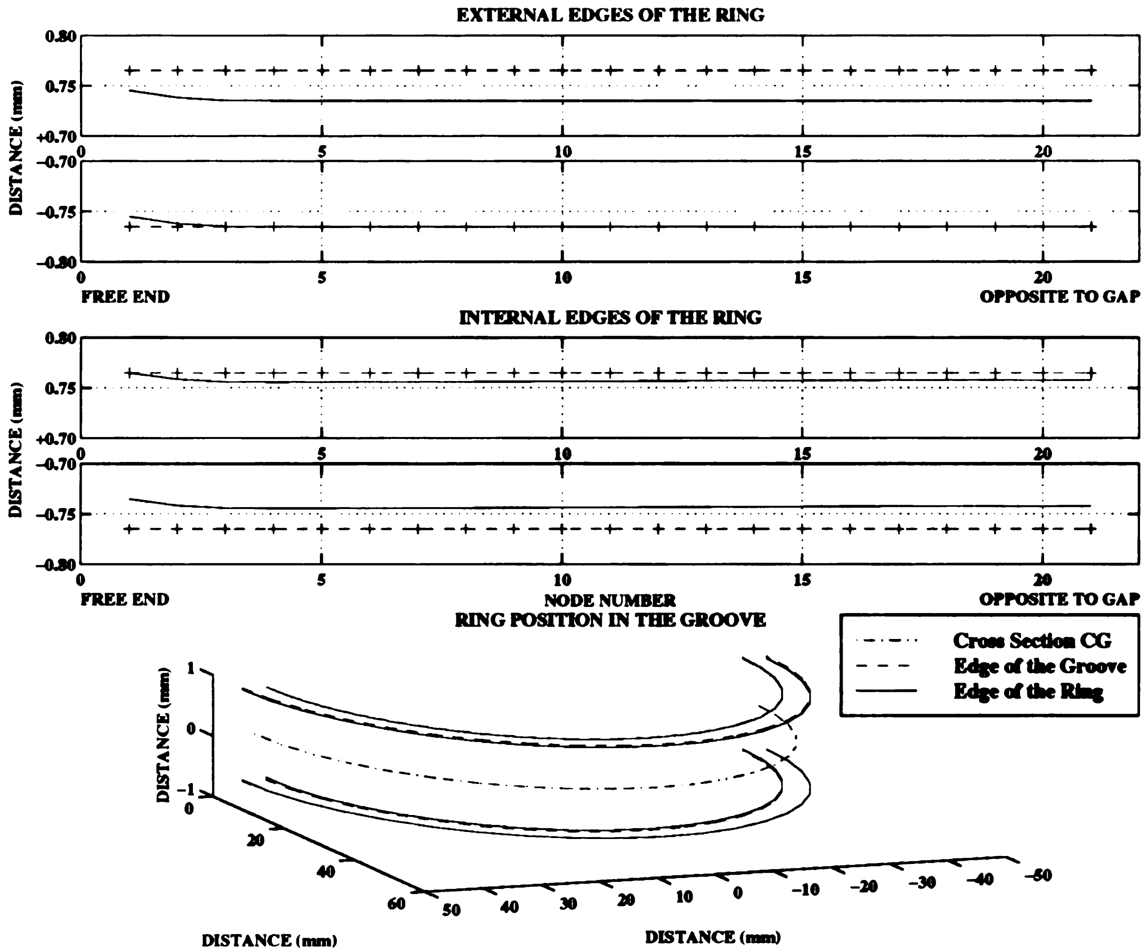

Figure 89 Second compression ring position in the groove at 346 degrees of crank angle

ring. Also, the third ring shows an oscillatory motion (ring fluttering) at 400 crank degrees. This oscillatory motion is due to an unstable equilibrium between the pressure and inertia forces.

Ring motion is closely inter-related with inter-ring gas pressures. The inter-ring gas pressures affect ring motion, the ring motion affects blow-by, and the blow-by affects the inter-ring gas pressures. A close examination of the inter-ring pressure traces in Figure 87 shows that the pressures change their magnitude and, more important, their gradients several times during the cycle. From the beginning of the intake stroke until the middle of the compression stroke, the combustion chamber pressure is low. The second and third land pressures are also low and exhibit only small changes. As the in-cylinder pressure rises, the second land pressure increases due to blow-by across the top ring. At 350 crank degrees, the second land pressure changes its gradient and forms a "plateau". This "plateau" corresponds to the second ring motion. As the second ring moves from the top to the bottom of the groove, it opens an additional passage for gas flow behind the ring which increases the blow-by from the second to the third land.

The other second land pressure gradient change occurs at 550 crank degrees. At this moment, the combustion chamber pressure is lower than the pressure on the second land. When the top ring moves from the bottom to the top of the groove, it opens an additional passage for gas flow and increases the gas flow from the second land back to the combustion chamber, causing a pressure drop on the second land.

Another interesting relationship between the combustion and second land pressures is the "cross-over point" at the end of the power stroke when the combustion pressure equals to the second land pressure. The importance of the "cross-over point" is in indication of an unstable equilibrium between the pressure force due to a difference between the combustion chamber and second land pressures and the inertia force in this region. This unstable equilibrium may result in the top ring fluttering causing excessive blow-by and back flow.

An introduction of ring twist to ring dynamics makes the ring motion analysis more complicated. In addition to staying at the top or the bottom of the groove, the ring can twist with a contact of its internal edge (the edge inside the groove) at the top of the groove and the external edge (the edge closer to the cylinder liner) at the bottom of the

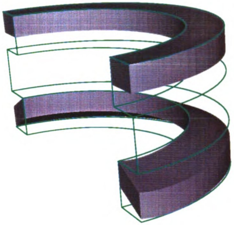

Crank Angle: 58.00

Figure 90 Top and second ring position in the grooves at 58 degrees of crank angle

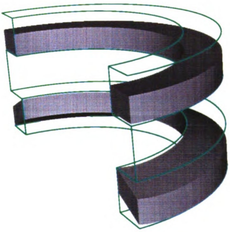

Crank Angle: 97.00

Figure 91 Top and second ring position in the grooves at 97 degrees of crank angle

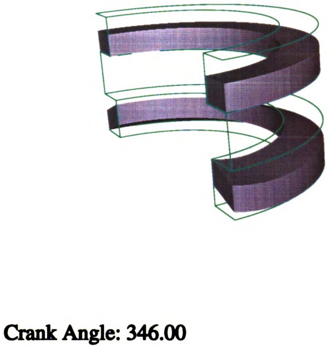

Figure 92 Top and second ring position in the grooves at 346 degrees of crank angle

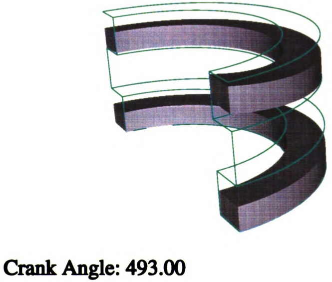

Figure 93 Top and second ring position in the grooves at 493 degrees of crank angle

groove, or vise versa. In general, a twisted ring does not twist uniformly and does not stay in contact with the top or bottom of the groove uniformly around the circumference, but changes its position and twisting angle. Figure 84 shows the combustion and inter-ring gas pressures, the third ring position and the top and second area ratios. Overall, the inter-ring gas pressures for this case show a similar trend to the untwisted case. The second land pressure experiences gradient changes at 350 and 500 crank degrees due to the second and top ring motions respectively. The top and second ring scaled average area ratios resemble the ring position plots for the untwisted case but look smoother especially for the second ring. (In the case of the no twist calculation, the scaled average area ratios are identical to the ring position.) The main difference between the twisted and untwisted cases for the top ring is in the transition time from the top to the bottom of the groove and back at 90 crank degrees (Figure 91) and 490 crank degrees (Figure 93). This difference is due to top ring twisting in addition to axial ring translation.

The second (twisted) ring shows much more difference in its motion between the twisted and untwisted case in comparison to the top (untwisted) ring. At the beginning of the cycle at 60 crank degrees (Figure 90), as it moves from the top to the bottom of the groove, the second ring experiences a significant twisting motion.

Another crank angle interval, when the second ring shows a different motion in comparison to the untwisted case, is between 270 and 360 degrees (Figure 92). First, the ring stays flat at the bottom of its groove. As the piston decceleration, the inertia force pushes the ring to the top of the groove and the ring starts twisting. The external edge of the ring, the edge close to the cylinder liner, stays at the bottom of the groove but the internal edge of the ring, the edge inside the groove, rises opening a passage for gas flow behind the ring. As the pressure inside the cylinder increases at the end of the compression stroke and the beginning of the power stroke, the pressure force pushes the ring back to the bottom of its groove. The ring untwists and stays flat against the bottom of groove. This twisting and untwisting motion of the second ring causes smooth gradient changes of the second land pressure. Figure 88 and Figure 89 show the top and second ring position in the groove at 97 and 346 degrees of crank angle respectively. Figure 90, Figure 91, Figure 92, and Figure 93 show the scaled relative position of the top and second rings in their grooves at 58, 97, 346, and 493 crank angle degrees.

Figure 85 and Figure 86 show the predictions for the cases of ring position calculations for the top ring with no twist and for the second ring with twist and vise versa. As expected, both of the plots show features of twisted and untwisted rings. It is worth pointing out the effect of ring twist on the second land pressure and pressure gradient changes at 350 crank degrees due to second ring motion and 500 crank degrees due to top ring motion.

Chapter 6 RING PACK OPTIMIZATION

INTRODUCTION

Optimization of mechanical systems is becoming an important issue in engineering. A significant amount of work has been done in the area of optimization [40, 42, 43, 15, 59, 80]. However, there is no available information on how optimization techniques have been applied toward ring pack design and analysis. The strategy of the ring pack optimization is logically subdivided into two parts. In the first part, an optimization algorithm searches for the optimal set of the design variables which satisfy the objective function criteria and the set of constraints. The second stage includes calculations of the objective function with a given set of design variables as well as sensitivities of the objective function and design constrains with respect to the design variables.

There is a large number of optimization algorithms available [40, 42, 43, 15, 59, 80, 60]. These algorithms can be classified as constrained and unconstrained depending on the constraints on the design variables. Depending on the search strategy, the algorithms can be classified as gradient based algorithms and non-gradient ones. In non-gradient algorithms the direction of the search methods use only function evaluation. The genetic algorithm is an example of a non-gradient optimization method. In gradient based algorithms the search method is determined based on the gradient of the objective function and the active constraints.

A general optimization problem can be stated as follows:

$$
\begin{aligned}
&\underset{x \in \Re^n}{min} f(x) \\
&\text{such that:} \\
&h_i(x) = 0 \qquad i = 1 \ldots m_e \\
&g_i(x) \le 0 \qquad i = m_e + 1 \ldots m
\end{aligned}
\tag{85}
$$

where $f(x)$ is the objective function be optimized, $h_i(x)$ is an equality constraint, and $g_i(x)$ is an inequality constraint. For the case of the constraint optimization, the Lagrangian function is defined as follows:

$$
\begin{aligned}
&L(x, \mu, \lambda) = f(x) + \sum_{i=1}^{m_e} \mu_i h_i(x) + \sum_{i=m_e+1}^{m} \lambda_i g_i(x) \\
&\text{such that} \\
&\lambda_i = \begin{cases} \lambda_i \le 0 & g_i(x) = 0 \\ \lambda_i = 0 & g_i(x) < 0 \end{cases} \\
&\mu_i \le 0
\end{aligned}
\tag{86}
$$

The necessary conditions for a stationary point (The Kuhn-Tucker equations) are

$$
\begin{aligned}
&\frac{\partial L(x, \mu, \lambda)}{\partial x_i} = \frac{\partial f}{\partial x_i} - \sum_{j=1}^{m_e} \mu_j \frac{h_j(x)}{\partial x_i} + \sum_{j=m_e}^{m} \lambda_j \frac{g_j(x)}{\partial x_i} \qquad i = 1, \ldots, n \\
&\frac{\partial L(x, \mu, \lambda)}{\partial \mu_j} = h_j(x) = 0 \qquad j = 1, \ldots, m_e \\
&\frac{\partial L(x, \mu, \lambda)}{\partial \lambda_j} \lambda = g_j(x) \lambda = 0 \qquad j = m_e, \ldots, m \\
&\text{such that} \\
&\lambda_i = \begin{cases} \lambda_i \le 0 & g_i(x) = 0 \\ \lambda_i = 0 & g_i(x) < 0 \end{cases} \\
&\mu_i \le 0
\end{aligned}
\tag{87}
$$

The Sequential Quadratic Programing (SQP) algorithm has been used [40, 52] for the ring pack optimization. SQP is a gradient based algorithm for non-linear optimization. In this algorithm, a Quadratic Programming (QP) sub-problem is solved at each major iteration. The QP sub-problem is formulated based on a quadratic approximation of the Lagrangian function (Eq. (86)).

RING PACK OPTIMAZATION

Problem Statement

The formalized ring pack optimization problem can be stated as follows:

$$\begin{aligned}
&\min_{x} G(x, z) \\
&\text{such that:} \\
&A\dot{z} = F(z, x, t) \qquad z(T) = z(0) \qquad (\text{or } z(t) = z(t+nT)) \\
&h_i(x) = 0 \qquad i = 1 \ldots m_e \\
&g_i(x) \leq 0 \qquad i = m_e + 1 \ldots m
\end{aligned} \tag{88}$$

where:

$$G(x, z) = \int_0^T p(x, z, t)dt \tag{89}$$

is the objective function, x is a vector of the design variables, and z is a state variable with the state equation as a constraint. The physical meaning of the objective function $G(x, z)$ [as well as $p(x, z, t)$] depends on the ring pack criteria to be optimized. If the total blow-by is to be optimized, $p(x,z,t)$ represents the mass flow rates across the ring pack. The integral of the maas flow rates over the engine cycle gives the total blow-by. If second ring fluttering is to be optimized, $G(x, z)$ represents the total traveling of the second ring, and $p(x,z,t)$ is the absolute value of the second ring velocity.

The state space equation with cyclic conditions is the following:

$$A\dot{z} = F(z, x, t) \qquad z(T) = z(0) \qquad (\text{or } z(t) = z(t+nT)) \tag{90}$$

The state space representation of the governing equations of the physical processes in the ring pack are described in Chapter 2 on page 9. The functions $g(x, z)$ and $h(x, z)$ in Eq. (88) represent a set of the inequality and equality constraints on the design variables respectively.

SENSITIVITY ANALYSIS

The derivatives of the objective function and constraints with respect to the design variables are the following:

$$\frac{dG}{dx} = \int_0^T \left[\frac{\partial p}{\partial x} - \frac{\partial p}{\partial z}\frac{dz}{dx}\right] dt \tag{91}$$

$$\begin{aligned} \frac{dg_i}{dx} &= \frac{\partial g_i}{\partial x} \\ \frac{dh_i}{dx} &= \frac{\partial h_i}{\partial x} \end{aligned} \tag{92}$$

All terms on the right hand side except one in Eq. (91) and Eq. (92) can easily calculated since $p(x, z, t)$ is an explicit function of x and z, and $g(x)$ and $h(x)$ are explicit functions of x. However, the term $\frac{dz}{dx}$ needs special consideration since the state vector z does not explicitly depend on the design vector x. The sensitivities can be determined analytically using the direct method or the adjoint variable method [40, 42], or numerically.

Direct Method

In the direct differentiation method, Eq. (90) is differentiated to obtain an equation for $\frac{dz}{dx}$ with the cyclic conditions

$$A\frac{d\dot{z}}{dx} = J\frac{dz}{dx} - \frac{dA}{dx}\dot{z} + \frac{\partial F}{\partial x} \qquad \frac{dz}{dx}(0) = \frac{dz}{dx}(T) \tag{93}$$

where J is the Jacobian matrix

$$j_{ij} = \frac{\partial f_i}{\partial z_j} \tag{94}$$

The direct method consists of solving Eq. (93) and substituting $\frac{dz}{dx}(t)$ into Eq. (91). This process has to be repeated for each design variable.

Adjoint Variable Method

The adjoint variable method consists of multiplying Eq. (93) by the transposed adjoint vector Λ^T and integrating it

$$\int_0^T \Lambda^T\left[A\frac{d\dot{z}}{dx} - J\frac{dz}{dx}\right]dt = \int_0^T \Lambda^T\left[\frac{\partial F}{\partial x} - \frac{dA}{dx}\dot{z}\right]dt \tag{95}$$

Integrating by parts yields

$$\Lambda^T \frac{dz}{dx}\bigg|_0^T - \int_0^T [\dot{\Lambda}^T A + \Lambda^T \dot{A} + \Lambda^T J] \frac{dz}{dx} dt = \int_0^T \Lambda^T \left[\frac{\partial F}{\partial x} - \frac{dA}{dx}\dot{z}\right] dt \tag{96}$$

Applying conditions on Λ gives

$$A^T \dot{\Lambda} + (J^T + \dot{A}^T)\Lambda = \left(\frac{\partial p}{\partial x}\right)^T \qquad \Lambda(T) = \Lambda(0) \tag{97}$$

$$\int_0^T \frac{\partial p}{\partial z}\frac{dz}{dx} dt = -\int_0^T \Lambda^T \left[\frac{\partial F}{\partial x} - \frac{dA}{dx}\dot{z}\right] dt \tag{98}$$

Substituting Eq. (98) into Eq. (91) yields

$$\frac{dG}{dx} = \int_0^T \left[\frac{\partial p}{\partial x} - \Lambda^T \left(\frac{\partial F}{\partial x} - \frac{dA}{dx}\dot{z}\right)\right] dt \tag{99}$$

An adjoint equation (Eq. (97)) needs to be solved for the objective function and every constraint function required.

Finite Difference Approximation

Sensitivity derivatives can be approximated numerically using the Finite Difference Method as follows:

$$\frac{dG}{dx} \approx \frac{G(z, x + \delta x) - G(z, x)}{\delta x} \qquad \delta x \to 0 \tag{100}$$

MODELING STRATEGY

Optimization Algorithm

In this study, the ring pack analysis model, the RING program, has been used with the MATLAB Optimization Toolbox [53]. The MATLAB Optimization Toolbox provides a set of algorithms for constrained and unconstrained optimization. In this analysis, a constrained optimization algorithm was used. This algorithm employs a Sequential Quadratic Programing (SQP) technique as a search method. At each iteration, the algorithm requires evaluation of the objective function and the gradients of the objective function and constraints with respect to the design variables. In order to obtain this information, an interface between the optimizer and the RING program has been established. The flow chart of the interface is shown in Figure 94.

The RING program calculates the value of the objective function with the set of the design variables provided as well as the design parameters and in-cylinder pressure obtained from a data file. The gradients of the objective function with respect to the design variables are calculated numerically using the finite difference method, perturbing the design variables with sufficiently small increments. The finite difference approximation provides an intelligent compromise in calculating the gradients. The problem associated with the analytical method for gradient calculations is in the discontinuity of some of the state variables (velocities of the rings). During an engine cycle, the piston ring travels from the top of the groove to the bottom of the groove and back with an impact contact with the groove. During the ring / groove impact, the ring changes its velocity. The time scale of this process is an order of magnitude smaller than the time scale of the overall ring dynam-

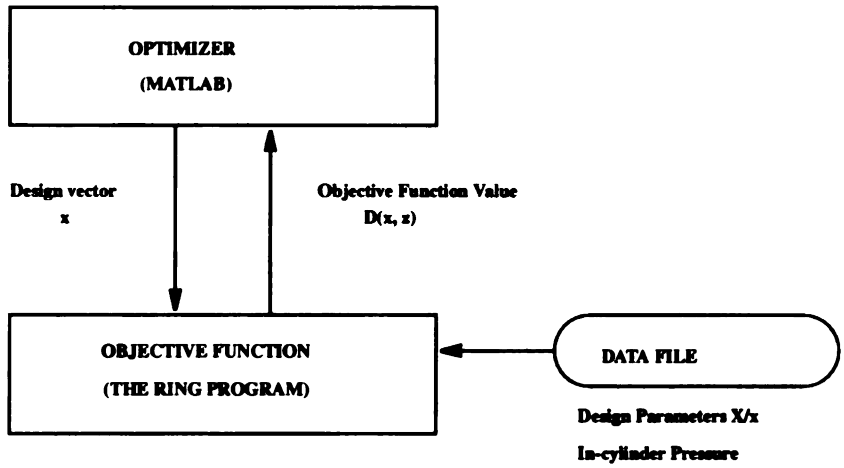

Figure 94 Flow chart of the ring pack optimization strategy

ics [68, 3]. In the RING model, ring / groove impact is modeled with a coefficient of restitution. Using this technique avoids numerical difficulties associated with the stiff problems due to different time scales. The analytical calculations of the objective function gradients is challenging due to a discontinuity in the system Jacobian. The finite difference approximation provides a reasonable alternative to the analytical methods. A special precaution is taken in order to achieve a reasonable accuracy using the finite difference method. For this purpose, the design variables and the objective function have been carefully scaled.

The objective function is calculated as follows:

$$G(x) = \mu \sum_{i=1}^{n} (|\psi_i| \cdot w_i) \tag{101}$$

where w_i is the weight for the operating condition iteration i, ψ_i is the total blow-by calculated by the RING program for the operating condition iteration i, and μ is the objective function scaling factor.

Model Application

The ring pack optimization routine has been applied to two engines: the 4.6L V8 and the 5.4L V8. These two engines have similar ring pack designs, similar pistons, and the same bore diameter. The major difference between them is in the length of the engine stroke. The similarities and differences in ring pack behaviors for these two engines are described in Chapter 6 on page 132. The design parameters being optimized include the top ring end gap clearance, the top ring thickness, the second ring end gap clearance, and the second ring thickness (Figure 95). For each engine, four optimization runs have been performed to find the optimal design parameters based on single and multiple engine operating conditions. The description of the runs is given in Table 4. Two optimization runs use a single engine operating condition of 2500 rpm and 8 inches of the intake manifold vacuum. The other two runs employ sixteen engine operating conditions based on the Ford engine test cycle [7]. The diagram of the Ford engine test cycle is shown in Figure 96. Duration and weights of the test point operating conditions used for the optimization are shown in Table 5. During its operation, an engine is run more often at certain operating conditions than others. The engine test cycle represents distribution of operating conditions for typical driving conditions. The operating conditions at which the engine is run more often contribute more to overall engine performance. These operating conditions require more attention during engine design and analysis.

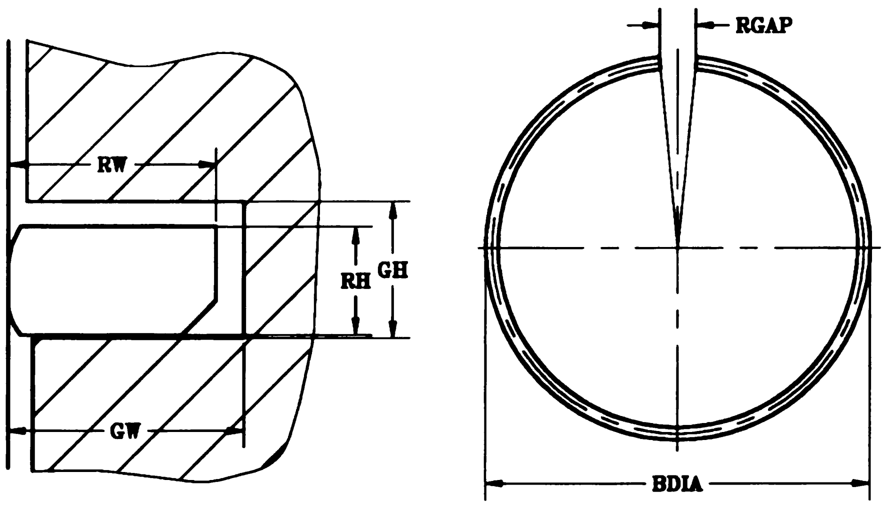

Figure 95 Ring design parameters. RH and RGAP are optimized

Table 4 Optimization test run designation

Optimization Runs	Operating Conditions	Design Parameters
Single 1	single point	test 1 from Table 6
Single 2	single point	test 2 from Table 6
Cycle 1	cycle from Table 5	test 1 from Table 6
Cycle 2	cycle from Table 5	test 2 from Table 6

Based on minimum and maximum limits on the allowable ring pack design parameters, the optimization runs are divided into two groups, test runs 1 and test runs 2. The differences between test runs 1and test runs 2 are in the minimum ring thicknesses and end gap clearances for the top and second compression rings. For all optimization runs, the maximum ring thicknesses are limited by 0.99 of the corresponding ring groove

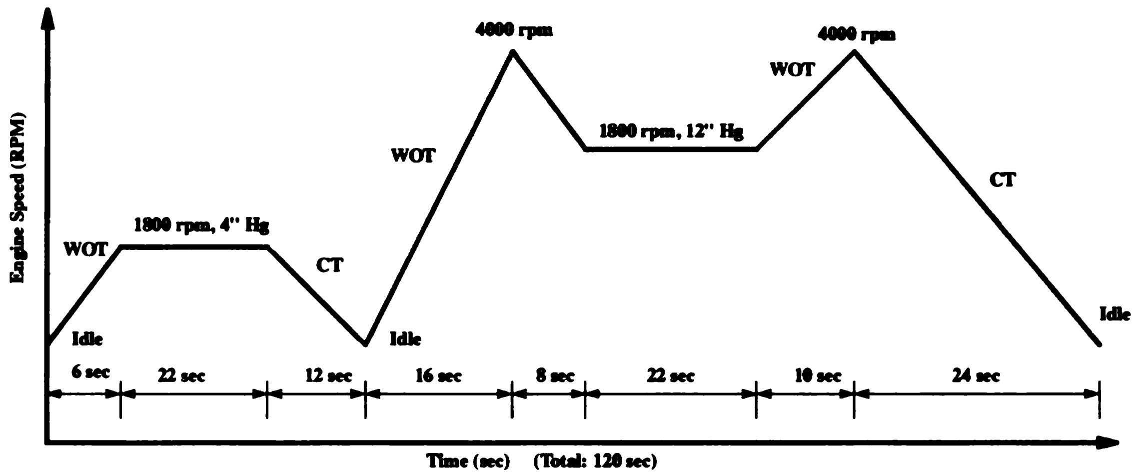

Figure 96 Ford transient engine test cycle

heights in order to ensure the ring fitting into the groove; and the maximum ring end gap clearances are limited to 2.0 mm.The summary of ring gap clearances, ring thicknesses, and upper and lower bounds on the design variables is shown in Table 6. The test runs 1 represent a more interesting case from the mathematical point of view when the lower bounds are close to zero. The test runs 2 are more interesting from the engineering point of view because of difficulties of manufacturing piston rings with dimension from the test run 1(ring thickness of 0.001 mm and ring end gap clearance of 0.001 mm). The ring thickness of 0.5 mm and end gap clearance of 0.05 mm are more practical and possible to manufacture.

Table 5 Operating condition duration and weights for the Ford Geotze cycle for test 2

Points	Speed (RPM)	Manifold Vacuum	Duration (sec)	Weight
1	1000	0"	1.83	0.0832
2	1500	0"	5.67	0.2577
3	2000	0"	5.42	0.2464
4	2500	0"	5.17	0.2350
5	3000	0"	5.17	0.2350
6	3500	0"	5.14	0.2350
7	4000	0"	2.58	0.1173
8	1000	22"	5.0	0.2273
9	1500	22"	10.0	0.4545
10	2000	22"	8.0	0.3636
11	2500	22"	12.0	0.5455
12	3000	22"	6.0	0.2727
13	3500	22"	6.0	0.2727
14	4000	22"	3.0	0.1364
15	2000	4"	22.0	1.0
16	2000	12"	22.0	1.0

Table 6 Initial values, upper bounds, and lower bounds of ring design parameters

Design Parameters	Initial Dimension	Lower Bound		Upper Bound	
		Test 1	Test 2	Test 1	Test 2
Ring Gap 1	0.200	0.001	0.05	2.0	
Ring Thickness 1	1.5	0.001	0.5	1.5147	
Ring Gap 2	0.205	0.001	0.05	2.0	
Ring Thickness 2	1.51	0.001	0.5	1.5246	

OPTIMIZATION RESULTS

Four optimization runs have been performed for each engine: the 4.6L V8 and the 5.4L V8. Each run started with the same initial design parameters. The summary of the optimization results for both engines are given in Table 7 and Table 8. In these tables *rcl1*, *rth1*, *cl2*, and *rth2* refer to the ring end gap clearance for the top ring, the ring thickness for

Table 7 Optimization results for the 4.6L V8 engine

	Single 1	**Single 2**	**Cycle 1**	**Cycle 2**
Ring Gap 1	0.00100	0.05000	0.00100	0.20758
Ring Thickness 1	1.51470	1.50600	1.50759	0.64014
Ring Gap 2	0.00100	0.05000	0.00112	0.05000
Ring Thickness 2	1.52460	1.52460	1.48117	1.50944
Iterations	34	86	91	101
Initial *G*	4.32663	4.32663	1.00772	1.00772
Final *G*	0.07847	0.919384	0.02157	0.12556

Table 8 Optimization results for the 5.4L V8 engine

	Single 1	**Single 2**	**Cycle 1**	**Cycle 2**
Ring Gap 1	0.06030	0.05000	0.00100	0.12080
Ring Thickness 1	0.00100	0.50080	1.51470	0.50000
Ring Gap 2	0.62740	0.05020	0.00100	0.05000
Ring Thickness 2	0.78060	0.95610	1.08228	1.48808
Iterations	200	77	60	62
Initial *G*	5.52156	5.52156	1.47093	1.47093
Final *G*	0.00000052	0.14726	0.02563	0.16523

the top ring, the ring end gap clearance for the second ring, and the second ring thickness respectively. The number of calls from the optimizer to the objective function evaluations (The RING program) is denoted by *iterations*. The initial and final values of the objective function for each run are given in *initial G* and *final G* respectively.

In order to compare the performance of the ring packs with the optimized parameters against the initial design over a wide range of operating conditions, the blow-by and back flow maps were generated for each set of optimized ring design parameters as well as for the initial design. The blow-by and back flow maps are shown in Figure 97 to Figure 116.

The blow-by and back flow maps with the initial ring pack design parameters for the 4.6 L V8 and 5.4L V8 engines are shown in Figure 97, Figure 98, Figure 99, and Figure 100. The blow-by maps as well as the back flow maps for both the engines show many similarities. The blow-by and back flow results form a plain surface with an inclination from high engine load (low manifold vacuum) to low engine load (high manifold vacuum), and from low engine speeds to high engine speed. The slope in the dimension of engine load is steeper than in the dimension of engine speed. At low engine load (high manifold vacuum) and high engine speed, the maps show spikes in blow-by and back flow. These spikes are due to top ring collapse. The mechanisms of ring collapse are described in Chapter 6 on page 132.

The blow-by and back flow maps for both engines with the ring pack parameters from the optimization runs of *single 1* are shown in Figure 101, Figure 102, Figure 103, and Figure 104. In this case, the ring pack design parameters were optimized based on a single operating condition with a minimum ring thickness and minimum ring end gap

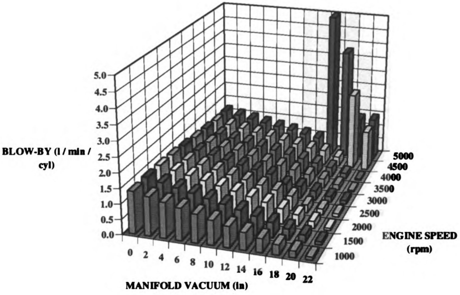

Figure 97 Predicted blow-by map from the cylinder for the 4.6L V8 engine with the initial ring pack parameters

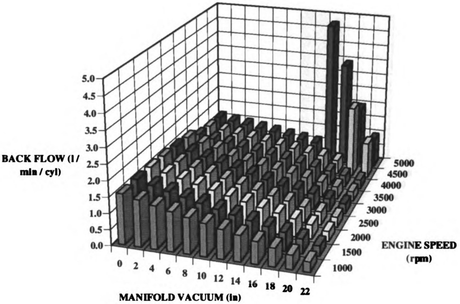

Figure 98 Predicted back flow map into the cylinder for the 4.6L V8 engine with the initial ring pack parameters

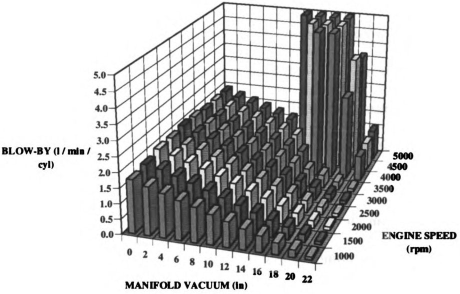

Figure 99 Predicted blow-by map from the cylinder for the 5.4L V8 engine with the initial ring pack parameters

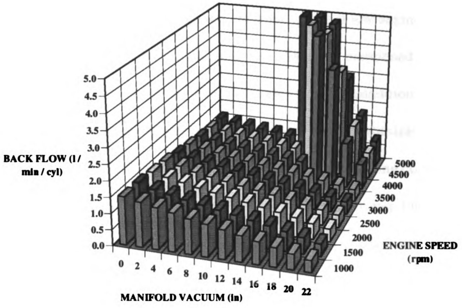

Figure 100 Predicted back flow map into the cylinder for the 5.4L V8 engine with the initial ring pack parameters

clearance of 0.001 mm. The blow-by and back flow maps show a significant improvement for both the engines. For the case of the 5.4L V8 engine, the blow-by map (Figure 103) show a step increase in blow-by at high engine load (low manifold vacuum) and all speed. The step increase of blow-by is due to second ring fluttering because of relatively small thickness of the second ring and ignoring these particular operating conditions during optimization.

Blow-by and back flow maps for both the engines with more realistic ring pack design parameters optimized for a single operating condition are shown in Figure 105, Figure 106, Figure 107, and Figure 108. In this case, designated as *single 2*, the minimum allowed ring end gap clearances and ring thickness are of 0.05 mm and 0.5 mm respectively. Overall, the blow-by and back flow maps show improvements over the initial maps. However, they are not as drastic as the previous case (case *single 1*). In addition, the blow-by and back flow maps for both the engines show the spikes at low engine load (high manifold vacuum). These spikes are due to top ring collapse as mentioned above. Since the design parameters are optimized based on the single operating condition at which the ring collapse does not occur, these spikes are not considered during optimization. It is interesting to note that for the 5.4L V8 engine, the blow-by spikes due to ring collapse are shifted toward lower engine speed in comparison to the original blow-by map for this engine. The shift is due to a different combination of the top and second ring thickness and, therefore, different ring masses for this set of the ring pack design parameters. The blow-by for the 5.4L V8 engine show a step increase in blow-by at high engine load (low manifold vacuum) similar to the previous case of *single 1*.

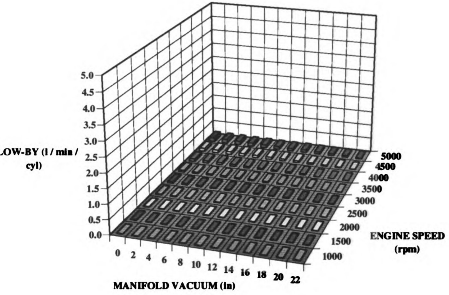

Figure 101 Predicted blow-by map from the cylinder for the 4.6L V8 engine with the ring pack parameters from *single 1*

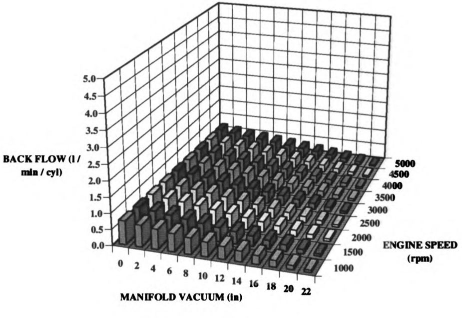

Figure 102 Predicted back flow map into the cylinder for the 4.6L V8 engine with the ring pack parameters from *single 1*

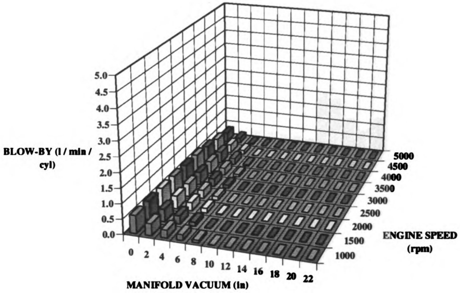

Figure 103 Predicted blow-by map from the cylinder for the 5.4L V8 engine with the ring pack parameters from *single 1*

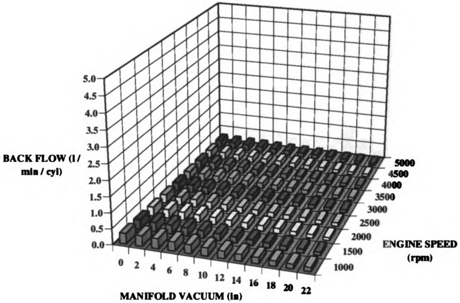

Figure 104 Predicted back flow map into the cylinder for the 5.4L V8 engine with the ring pack parameters from *single 1*

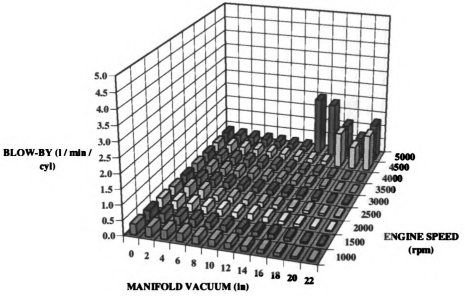

Figure 105 Predicted blow-by map from the cylinder for the 4.6L V8 engine with the ring pack parameters from *single 2*

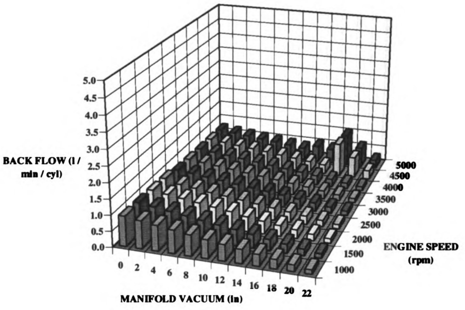

Figure 106 Predicted back flow map into the cylinder for the 4.6L V8 engine with the ring pack parameters from *single 2*

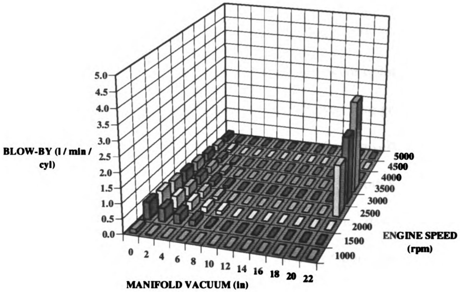

Figure 107 Predicted blow-by map from the cylinder for the 5.4L V8 engine with the ring pack parameters from *single 2*

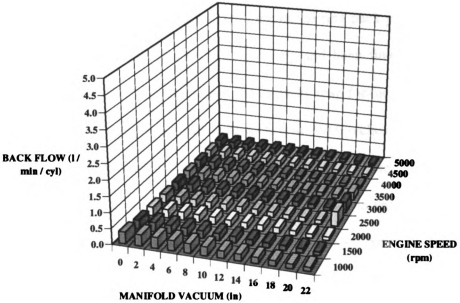

Figure 108 Predicted back flow map into the cylinder for the 5.4L V8 engine with the ring pack parameters from *single 2*

The blow-by and back flow maps for both engines with the ring pack parameters from the optimization runs of *cycle 1* are shown in Figure 109, Figure 110, Figure 111, and Figure 112. In this case, ring pack design parameters were optimized based on multiple operating conditions (Table 5) and the minimum allowed ring gap clearances and ring thickness of 0.001 mm each. The blow-by and back flow results show a significant improvement in comparison to the original maps and form smooth surfaces for the whole range of operating conditions. The only difficulties associated with these map are in extremely small ring end gap clearances for both the rings from a practical point of view.

Blow-by and back flow maps for both the engines with more realistic ring pack design parameters optimized for multiple operating conditions (Table 5) are shown in Figure 113, Figure 114, Figure 115, and Figure 116. This case is designated as *cycle 2*. Even though the blow-by and back flow are not as good as for the previous case, they show significant improvements over the results with the initial ring pack parameters (Figure 97, Figure 98, Figure 99, and Figure 100). The blow-by and back flow results for both the engines form smooth surfaces in the maps. The blow-by map for the 4.6L V8 engine show two spikes of a relatively small magnitude at 4000 rpm and 0 inches and 2 inches of manifold vacuum. These spikes are due to second ring fluttering at these operating conditions. The operating condition point of 4000 rpm 0 inches of manifold vacuum is used for optimization with a small weight. The operating condition of 4000 rpm 2 inches of manifold vacuum is not used at the engine test cycle and is not considered during optimization.

As seen in its results, the ring pack optimization routine can be a valuable tool for engine design and analysis. A special precaution should be taken to selecting the operating conditions on which the blow-by is optimized, the weights of optimization conditions, and

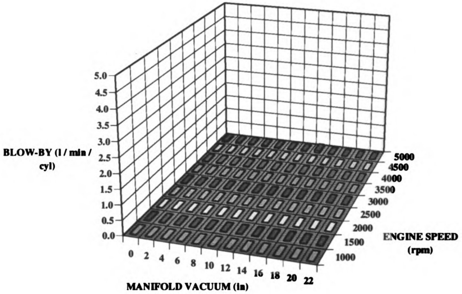

Figure 109 Predicted blow-by map from the cylinder for the 4.6L V8 engine with the ring pack parameters from *cycle 1*

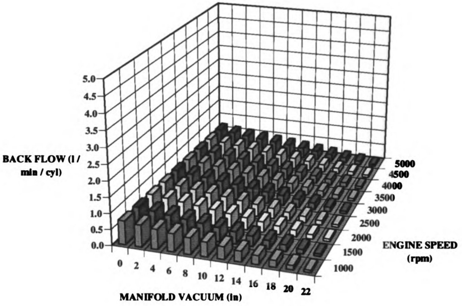

Figure 110 Predicted back flow map into the cylinder for the 4.6L V8 engine with the ring pack parameters from *cycle 1*

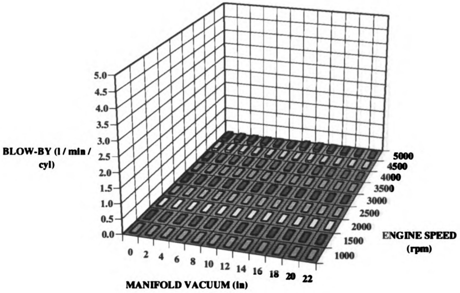

Figure 111 Predicted blow-by map from the cylinder for the 5.4L V8 engine with the ring pack parameters from *cycle 1*

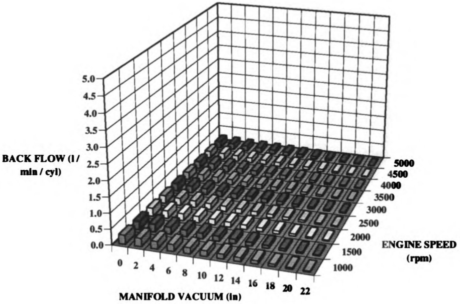

Figure 112 Predicted back flow map into the cylinder for the 5.4L V8 engine with the ring pack parameters from *cycle 1*

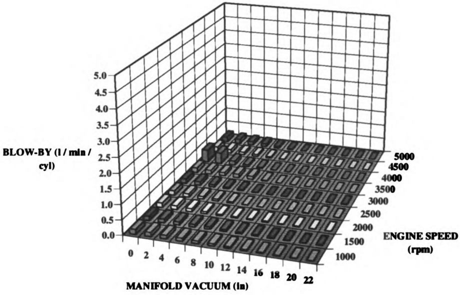

Figure 113 Predicted blow-by map from the cylinder for the 4.6L V8 engine with the ring pack parameters from *cycle 2*

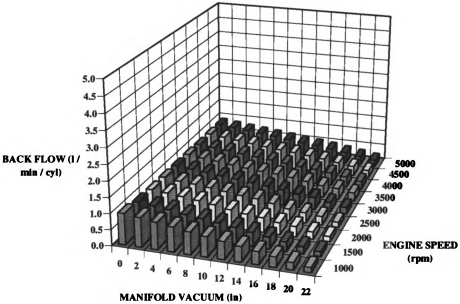

Figure 114 Predicted back flow map into the cylinder for the 4.6L V8 engine with the ring pack parameters from *cycle 2*

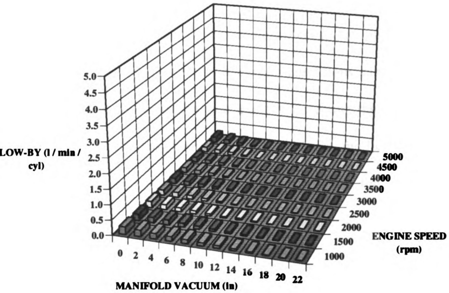

Figure 115 Predicted blow-by map from the cylinder for the 5.4L V8 engine with the ring pack parameters from *cycle 2*

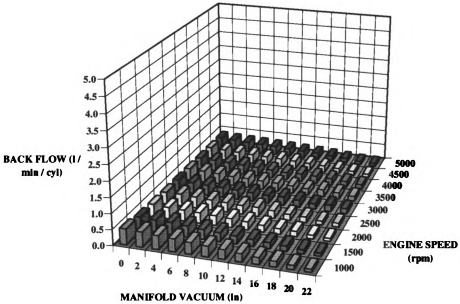

Figure 116 Predicted back flow map into the cylinder for the 5.4L V8 engine with the ring pack parameters from *cycle 2*

the limits of the allowed design parameters. The fewer operating conditions are used for optimization, the less expensive and time consuming computations of the optimization are. The different set of the weights of the operating conditions can significantly change the influence of one operating condition over another. Selecting the limits of the allowed design parameters may be challenging as well. On one hand, the limits should provide a wide range of possible design parameters. On the other hand, the limits should be feasible for manufacturing and reasonable in terms of computational cost.

Chapter 7 RECOMMENDATIONS AND CONCLUSION

In this dissertation, two major research areas have been considered: further development of the ring pack analysis model, the RING program, and application of the model to engine design and analysis in order to better understand physical processes in an internal combustion engine. The model development includes creating the three-dimension ring twist model, the TWIST program; establishing an interface between the in-cylinder combustion model, GESIM; and adding the ring pack optimization routine.

It was found that ring twist significantly influences ring pack performance. The nature of ring twist requires a three-dimensional analysis of the ring motion. The ring pack analysis program, the RING program, with three-dimensional ring twist analysis capabilities has been completed. Simulations were performed for an engine at the same operating conditions for several combinations of twist and no twist analysis. The twist analysis was shown to be very important for prediction of ring dynamics. The results show the influence of the ring twist on the ring position, inter-ring gas pressures and inter-ring pressure gradients. Special attention has to be paid to the motion of the twisted second ring at the middle of the intake and the end of the compression stroke and to the top ring at the beginning of the compression stroke and the end of the exhaust stroke.

Another part of the model development includes the ring pack optimization routine. In addition to engine modeling and design analysis, the ring pack optimization routine allows performance of design syntheses in a systematic manner. The ring pack optimization routine has been applied to two production engines. Four optimization runs with different limits on engine design parameters and different operating condition have been performed for each engine. The results have been confirmed for a wide range of operating conditions and compared with the initial ring pack design. It was shown that the ring pack optimization routine is a valuable tool for engine design and analysis.

In order to analyze engine performance at different operation condition and accommodate special features of a particular engine design, an interface between the ring pack model and the in-cylinder combustion model has been established. This interface allowed application of the ring pack model to the design and analysis including modeling of the Variable Displacement Engine (VDE) and analyzing the blow-by and back flow for three Ford production engines for a wide range of operating conditions.

The accommodation of the special features of the VDE engine required modification of the ring pack model. In the VDE engine analysis it was determined that the transient processes after the valves are shut off can be divided into two parts: a fast transient due to heat transfer and temperature drop and a slow transient due to ring pack breathing. The duration of the fast transient was determined to be seven cycles and the duration of the slow transient can be several thousand cycles depending on the amount of air mass trapped inside the cylinder.

Based on the analysis of net flow, back flow, and oil film thickness, the cycle based oil consumption can be estimated to be higher at 1500 rpm while the oil consumption on a time basis is higher at 3500 rpm. In addition, it was found that in order to reduce blow-by, back flow, and engine oil consumption, it is preferable to keep moderate pressure inside the combustion chamber. This pressure corresponds to the reference angle interval between 60 and 100 degrees.

For the blow-by analysis, the procedure to generate global blow-by and back flow maps for a wide range of operating conditions was established using the engine combustion model, GESIM, and the ring pack model, RING. The blow-by and back flow can be used as scalar parameters to characterize piston ring behavior for a given set of operating conditions. The blow-by and back flow maps for a wide range of operating conditions were generated for three production engines. The simulation results were correlated with experimental measurements and showed good agreement. In addition, it was found that the flow into the cylinder during the cycle, back flow, is interrelated with the net flow from the cylinder, blow-by. In this study, it was found that blow-by and back flow over a large range of operating condition are primarily influenced by the top ring design and top ring motion. In this region, the second ring has a secondary affect.

The ring pack performance is influenced by the ring pack parameters as well as the engine configuration. The influence of ring design parameters, such as ring mass and ring tension, on top ring behavior and the balance between pressure and inertia forces was analyzed. An increase of ring mass changes the balance between pressure and inertia forces and increase the occurrences of ring collapse and ensuing blow-by spikes. Increased ring tension can prevent ring collapse and reduces blow-by spikes. The side effects of increased ring tension are increased ring friction and ring wear.

It was found that the engine bore / stroke ratio affects ring pack performance. The cylinder bore diameter and the length of the crank affect pressure and inertia forces. Special attention has to be paid to the bore / stroke ratio in the early stages of engine design in order to optimize ring pack performance.

In future development, new features can be added to the ring pack analysis program. It would be interesting to consider the influence of three-dimensional ring motion including ring twist on oil film thickness developed between the ring face and the cylinder liner. Another interesting phenomenon may include modeling of oil flow in the ring groove behind the ring. These possible developments are related to formulation of oil consumption mechanisms such as oil evaporation from the cylinder liner, oil particle throw-off from the top of the piston, and influence of blow-by on oil consumption and engine emissions. A new development may also include formulating a more descriptive model of the oil control ring, especially the three-piece oil control ring common in automotive applications.

As recommendations, special attention needs to be paid to three major issues. First, engine designers need to consider at an early stage in engine development the influence of the engine bore / stroke ratio not only on the overall engine performance but also on the ring pack behavior. Second, the sensitivities of the ring pack parameters need to be taken into account for a wide range of operating conditions. Performing ring pack simulations for a wide range of operating conditions can be introduced as a standard practice. For this purpose, it may be necessary to introduce some other scalar parameters characterizing ring pack behavior for the whole engine cycle similar to blow-by and back flow. Third, for the purpose of determining the ring pack design parameters, it would be helpful to use the ring pack optimization based on the multiple operating conditions.

BIBLIOGRAPHY

BIBLIOGRAPHY

1. Abbot, M. B. and Basco, D. R., "*Computational Fluid Dynamics*," Longman Scientific & Technical, John Wiley & Sons, Inc., New York, 1990.

2. Anderson, J. D., "*Modern Compressible Flow*," McGraw-Hill, Inc., 1990.

3. Andronov, A. A., Vitt, A. A., and Khaikin, S. E., "*Theory of Oscillators*," Pergamon Press Ltd., 1966.

4. 1. Allen, D. G., Dudley, B. R., Middleton, V. and Parker, D. A., "Prediction of Piston Ring-Cylinder Bore Oil Film Thickness in Two Particular Engines and Correlation with Experimental Evidence," Proc. IMechE Conferece on Piston Ring Scuffing, paper No. C73/75, 1975.

5. Aue, G.K., "On the Mechanism of a Piston Ring Seal," Sulzer Technical Review, No. 1, 1974.

6. Baker, A. J. S., Dowson, D. and Strchan, P., "Dynamic Operating Factors in Piston Rings," International Symposium of Marine Engineers, paper 256, Tokyo, 1973.

7. Baladad, B. J., Sheare, P., and Leong, R., "Ultra Violet Sulfur Trace Oil Consumption Testing of Two 5.4L 2V Modular Truck Engines," Technical Report, Engene Performance Development, Ford Motor Company, October 96.

8. Borgnakke, Davis, G. C., and Tabaczynski, R. J., "Predictions of In-Cylinder Velocity and Turbulent Intensity for an Open Chamber Cup-in-Piston Engine," SAE Paper 810224 also *SAE Transactions* 90, 1981, pp. 964-978.

9. Brombolich, L. J., "Structural Mechanics of Piston Rings," Compu-Tec Eng. Internal Report, St. Louis, MO, 1993.

10. Brombolich L. J. "Effect of Cylinder Distortion and Piston Ring Design on Oil Consumption and Friction Losses in Automotive Engines," DE-AC02-86CE-90236, Report to US Department of Energy, 1988.

11. Brown, J. F. and Hamilton, G. M., "The Partially Lubricated Piston Ring," Journal Mech. Eng. Sci., Vol. 19, No 2, 1977, pp. 81-89.

12. Bryson, A. E., and Ho, Y. C., "*Applied Optimal Control*," Hemisphere Publishing Corporation, 1975.

13. Butler, J. F. and Heshall, S. H., "Piston Ring Performance in a Heavy Rated Two-Cycle Engine," Proc. IMechE Piston Ring Scuffing Conference, paper No. C75/75, 1975.

14. Cameron, A., "*Basic Lubrication Theory*," Ellis Horwood Ltd., Publishers, 1981.

15. Carmichael, D. G., "*Structural Modelling and Optimization: A General Methodology for Engineering and Control*," Ellis Horwood, Ltd., 1981.

16. CASE Analysis System. Theoretical Manual. Compu-Tec Engineering, Inc., Chesterfield, Missouri, 1995.

17. CASE Analysis System. User's Manual. Compu-Tec Engineering, Inc., Chesterfield, Missouri, 1995.

18. Castleman, R. A., "A Hydrodynamical Theory of Piston Ring Lubrication," Physics, Vol. 7, Sept. 1936, pp. 364-367.

19. Chow, P. L. and Saibel, E. A., "On the Roughness Effect in Hydrodynamic Lubrication," Trans. of the ASME, Vol. 100, 1978, pp. 176-180.

20. Christensen, H., "A Theory of Mixed Lubrication," Proc. IMechE. Vol. 186, 1972, pp. 421-430.

21. Corbat, J. P., "Mechanik der Kolbenringe mit Unsymmetrischem Querschnitt," Ph.D. Thesis, Eidgenossischen Technischen Hochschule Lausanne, 1974.

22. Das, P. K., "Analysis of Piston Ring Lubrication," SAE Paper 760008, 1976.

23. Davis, G. C., Mikulec, A., Kent, J. C., and Tabaczynski, R. J., "Modeling the Effect of Swirl on Turbulence Intensity and Burn Rate in SI Engines and Comparison with Experiments," SAE Paper 860325, 1986.

24. Dowson, D., Economu, P. N., Ruddy, B. L., Strachen, P. J. and Baker, A. J. S., "Piston Ring Lubrication—PartII: Theoretical Analysis of a Single Ring and a Complete Ring Pack," from 'Energy Conservation through Fluid Film Lubrication Technology: Frontiers in Research and Design,' Winter Annual Meeting of ASME, Dec. 1979, pp. 23-52.

25. Ejakov, M. A., Schock, H. J., Brombolich, L. J., Carlstrom, C. M., Williams, R. L. "Simulation Analysis of Inter-Ring Gas Pressure and Ring Dynamics and Their Affect on Blow-by," ICE-Vol. 29-2, 1997 Fall Technical Conference, Volume 2, ASME 1997.

26. Ejakov, M. A., Schock, H. J., Brombolich, L. J., Williams, R. L. "Comparison Between Predicted and Measured Inter-Ring Gas Pressures and Analysis of Factors Affecting Them," DAR 96-00858, Ford Design Analysis Report, November, 1996.

27. Ejakov, M. A., Hascher, H. G., Schock, H. J., Brombolich, L. J., Trinker, F. H., LoRusso, J. A. "Simulation Analysis of Ring Pack Bahavior in a Deactivated Cylinder," ICE-Vol. 27-2, 1996 Fall Technical Conference, Volume 2, ASME 1996.

28. Eilon, S. and Saunders, O. A., "A Study of Piston-Ring Lubrication," Proc. IMechE., Vol. 171, 1957, pp. 427-443.

29. Englisch, C., "Piston Rings for Heavy Duty I.C. Engines," C.I.M.A.C., paper B4, 1965, pp. 701-736.

30. ENGSIM User's Manual. Ford Research Laboratories, Ford Motor Company, Dearborn, Michigan, 1994.

31. FRAME 3D. User's Manual. Compu-Tec Engineering, Inc. Chesterfield, Missouri, 1986.

32. Furuhama, S., "A Dynamic Theory of Piston Ring Lubrication," Bull JSME, Vol. 2, No 7, 1952.

33. Furuhama, S. and Hiruma, M., "The Relationship Between Piston Ring Scuffing and the Formation of Surface Profile," Proc. IMechE Conference on Piston Ring Scuffing, paper No. C67/75, 1975.

34. Furihama, S. and Tada, T., "On The Flow of Gas Through the Piston Rings," Bulletin of the JSME, First Report—The Discharge Coefficient and Temperature of Leakage Gas, Vol. 4, No. 16, 1961, pp. 684-690.

35. Furihama, S. and Tada, T., "On The Flow of Gas Through the Piston Rings," Bulletin of the JSME, Second Report—The Character of Gas Leakage, Vol. 4, No. 16, 1961, pp. 691-698.

36. Gebhart, B., "*Heat Conduction and Mass Diffusion*," McGraw-Hill, Inc., 1993.

37. Graham, N. A. and Munro, R. "Investigation of Analysis of Oil Consumption and Blowby in Relation to Piston and Ring Features," AE Symposium, Paper No 28, 1981.

38. Greenwood, D. T., "*Principles of Dynamics*," Prentice-Hall, Inc., 1988.

39. Gulwadi, S. D., "A Mixed Lubrication and Oil Transport Model fro Piston Rings Using a Mass Conserving Algorithm," ASME ICE Vol.25-2, 1995, pp. 129-139.

40. Haftka, R. T. and Gurdal, Z., "*Elements of Structural Optimization*," Kluwer Academic Publishers, 1992.

41. Hamilton, G. M. and Moore, S. L., "Comparison Between Measured and Calculated Thicknesses of the Oil-Film Lubricating Piston Rings," Proc. IMechE., Vol. 188, 1974, pp. 262-268.

42. Haug, E. J., Choi, K. K., Komkov, V., "*Design Sensitivity Analysis of Structural Systems*," Academic Press, Inc., 1986.

43. Haug, E. J., and Arora, J. S., "*Applied Optimal Design*," Jonh Wiley & Sons, Inc., 1979.

44. Hersey, M., "*Theory and Research in Lubrication*," John Wiley & Sons, Publishers, 1966.

45. Heywood, J. B., "*Internal Combustion Engine Fundamentals*," McGraw-Hill, Inc., 1988.

46. Keribar, R., Dursunkaya, Z., and Flemming, M. F., "An Integrated Model of Ring Pack Performance," ASME *Journal of engineering for Gas Turbines and Power*, Vol 113, 1991, pp. 382-389.

47. Knowland, C. G., Russell, C. J., "Predictive Optimization of Piston and Ring Stability," SAE Paper 960873.

48. Kuo, K. K., "*Principles of Combustion*," John Wiley & Sons, Inc., 1986.

49. Lanczos, C., "*The Variational Principles of Mechanics*," Dover Publications, Inc., 1986.

50. Lilly, L. C. R., "*Diesel Engine Reference Book*," Butterworth and Co., Ltd., Publishers, 1984.

51. Lloyd, T., "The Hydrodynamic Lubrication of Piston Rings," Proc. IMechE, Vol. 183, Part 3P, 1968-1969, pp. 28-34.

52. MATLAB, Using MATLAB, Version 5, The MathWorks, Inc., 1996.

53. MATLAB, Optimization Toolbox, User's Guide, Version 5, The MathWorks, Inc., 1996.

54. Namazian, M. and Heywood, J. B., "Flow in the Piston-Cylinder-Ring Crevicesof a Spark-Ignition Engine: Effect on Hydrocarbon Emissions, Efficiency and Power," Feb. 1982, SAE paper 820088.

55. Newman, C. E., Stein, R. A., Warren, C. C., and Davis, G. C., "The Effect of Load Control with Port Throttling at Idle—Measurements and Analysis", SAE Paper 890679, 1989.

56. Oh, K. P., Li, C. H. and Goenka, P. K., "Elastohydrodynamic Lubrication of Piston Skirts," Transaction of the ASME, Vol. 109, April 1987.

57. Patir, N. and Cheng, H. S., "An Average Flow Model for Determining Effects of Three Dimensional Roughness on Partial Hydrodynamic Lubrication," Transactions of the ASME, Vol. 100, January 1978.

58. Patir, N. and Cheng, H. S., "Application of Average Flow Model to Lubrication Between Rough Sliding Surfaces," Transactions of the ASME, Vol. 101, April 1979.

59. Pierre, D. A., "*Optimization Theory with Applications*," Jonh Wiley & Sons, Inc., 1969.

60. Press, W. H., Flannery, B. P., Teukolsky, S. A., and Vetterling, W. T., "Numerical Recipies, The Art of Scientific Computing," Cambridge University Press, Cambridge, 1986.

61. Rhodes, M. L. P., "Piston Research and Development Techniques," The Associated Engineering Group, Technical Symposium, UK, June 1970.

62. Rohde, S. M., "A Mixed Friction Model for Dynamically Loaded Contacts with Application to Piston Ring Lubrication," from "Surface Roughness Effects in Hydrodynamic and Mixed Lubrication," Winter Annual Meeting of ASME, Nov. 1980.

63. Rohde, S. M., Whitaker, K. W. and McAllister, G. T., "A Study of the Effects of Piston Ring and Engine Design Variables on Piston Ring Friction," Winter Annual Meeting of ASME, Dec. 1979, pp. 117-134.

64. Ruddy, B. L., Dowson, D., and Economou, P. N., "A Theoretical Analysis of the Twin-Land Type of Oil-Control Piston Ring," *J. Mech. Eng. Sci.*, Vol. 23, pp 51-62., 1981.

65. Ruddy, B. L., Parsons, B., Dowson, D. and Economu, P. N., "The Influence of Thermal Distortion and Wear of Piston Ring Grooves upon Lubrication of Piston Rings in Diesel Engines," from 'Thermal Effects in Tribology,' Proc. IMechE, 1980, pp. 84-94.

66. Ruddy, B. L., "Lubrication and Dynamics of Piston Rings and the Theoretical Prediction of Ring Pack Gas Flow," Ph.D. Thesis, University of Leeds, 1979.

67. Ruddy, B. L., Dowson, D., Economu, P. N. and Baker, A. J. S., "Piston Ring Lubrication-Part III: The Influence of Ring Dynamics and Ring Twist," from 'Energy Conservation Through Fluid Film Lubrication Technology: Frontiers in Research and Design,' Winter Annual Meeting of ASME, Dec. 1979, pp. 191-215.

68. Shaw, S. W., "A Periodic Forced Piecewise Linear Oscillator," Ph.D. Thesis, Cornell University, 1983.

69. Sorab, J., Holdenman, H. A., and Chui, G. K., "Viscosity Prediction for Multigrade Oils: Temperature and Shear Rate Effects," Ford Research Technical Report No. SR-93-05.

70. Strogatz, S. H., "*Nonlinear Dynamics and Chaos*," Addison-Wesley Publishing Company, 1994.

71. Swift, H. W., "Elastic Deformation of Piston Rings", Engineering, 1947, pp. 161-165.

72. Tabaczynski, R. J., Trinker, F. H., and Shanon, B. A. S., "Further Refinement and Validation of a Turbulent Flame Propagation Model for Spark-Ignition Engines", *Combustion and Flame* **39**, 1980, pp. 111-121.

73. Taylor, R. I., Brown, M. A., Thompson, D. M., and Bell, J. C., "The Influence of Lubricant Rheology on Friction in the Piston Ring-Pack," SAE paper 941981.

74. Tian, T., Rabute, R., Wong, V. W., Heywood, J. B., "Effect of Piston-Ring Dynamics on Ring / Groove Wear and Oil Consumption in a Diesel Engine," SAE Paper 970835, 1997.

75. Tian T., Noorzij, L. B., Wong, V. W., Heywood, J. B., "Modeling Piston-Ring Dynamics, Blow-by, and Ring-Twist Effects," ICE-Vol. 27-2, 1996 Fall Technical Conference, Volume 2, ASME 1996.

76. Tian T., Wong, V. W., Heywood, J. B., "A Piston Ring-Pack Film Thickness and Friction Model for Multigrade Oils and Rough Surfaces ," Oct. 1996, SAE paper 962032.

77. Ting, L. L., "Lubricated Piston Rings and Cylinder Bore Wear", Wear Control Handbook, ASME, 1980.

78. Ting, L. L. and Mayer, J. E., "Piston Ring Lubrication and Cylinder Bore Analysis, Part I—Theory," ASME Journal of Lubrication Technology, Vol. 96, pp. 305-314; Paper No. 73-Lub-25., 1974.

79. Ting, L. L. and Mayer, J. E., "Piston Ring Lubrication and Cylinder Bore Wear Analysis, Part II—Theory Verification," Transactions of the ASME, Journal of Lubrication Thechnology, Paper No. 73-Lub-27, 1974.

80. Vanderplaats, G. N., "*Numerical Optimization Techniques for Engineering Design: With Applications*," McGraw-Hill, New york, 1984.

81. Wark, K., "*Advances Thermodynamics for Engineers*," McGraw-Hill, Inc., 1995.

82. White, F. M., "*Viscous Fluid Flow*," McGraw-Hill, Inc., 1991.

83. Wiggins, S., "*Introduction to Applied Nonlinear Dynamical Systems and Chaos*," Springer-Verlag New York, Inc., 1990.

84. Young, W.C.,"*Roark's Formulas for Stress and Strain*", Sixth Edition, Mcguire Hill, Inc., 1989.

85. Yun, J. E., Chung, Y. C., Chun, S. M. and Lee, K. Y., " An Application of Simplified Average Reynolds Equation for Mixed Lubrication Analysis of Piston Ring Assembly in an Internal Combustion Engine," May 1996, SAE paper 952562.